



ALGORITHMS FOR SMALL
SATELLITE FORMATION FLYING

THESIS

Robert B. LaRue, 2nd Lieutenant, USAF

AFIT-ENY-MS-18-M-273

DEPARTMENT OF THE AIR FORCE
AIR UNIVERSITY

AIR FORCE INSTITUTE OF TECHNOLOGY

Wright-Patterson Air Force Base, Ohio

The views expressed in this thesis are those of the author and do not reflect the official policy or position of the United States Air Force, Department of Defense, or the United States Government.

AFIT-ENY-MS-18-M-273

ALGORITHMS FOR SMALL
SATELLITE FORMATION FLYING

THESIS

Presented to the Faculty
Department of Aeronautics and Astronautics
Graduate School of Engineering and Management
Air Force Institute of Technology
Air University
Air Education and Training Command
In Partial Fulfillment of the Requirements for the
Degree of Master of Science in Astronautical Engineering

Robert B. LaRue, B.S.
2nd Lieutenant, USAF

March 2018

AFIT-ENY-MS-18-M-273

ALGORITHMS FOR SMALL
SATELLITE FORMATION FLYING

Robert B. LaRue, B.S.
2nd Lieutenant, USAF

Committee Membership:

Lt Col Kirk W. Johnson, PhD
Chair

William E. Wiesel, PhD
Member

Capt Joshua A. Hess, PhD
Member

Abstract

This thesis presents algorithms for spacecraft formation flying using impulsive-thrust and low-thrust methods. The general circular orbit formation initial conditions are derived in terms of equinoctial elements. Physical significance of the bounded relative motion parameters is presented for the case of general circular orbits. The developed algorithms are posed in terms of equinoctial elements for a singularity-free approach. The algorithms are assessed by numerical propagation of the inertial equations of motion with J_2 and drag perturbations. Methods are presented for minimizing the ΔV required for formation initialization. An examination of the performance of open-loop and closed-loop control is provided for formation initialization and reconfiguration. The effects of differential drag on small satellite formations is analyzed. The developed algorithms are used to examine the trade space and quantify how spacecraft design parameters affect formation flying scenarios.

Acknowledgements

I would like to thank my advisor, Lieutenant Colonel Kirk Johnson, for his mentorship and guidance throughout my time here at AFIT. Completing my research was made possible by drawing on his expertise and knowledge. Additional thanks go to the student and faculty members of the RPO working group, whose weekly feedback greatly improved the quality and clarity of my work.

I would also like to thank Dr. William Wiesel and Captain Joshua Hess for serving on my thesis committee. I'm also very grateful to the Air Force Research Laboratory for supporting my research here at AFIT. Finally, I would like to thank the U.S. Air Force for allowing me to spend my first assignment as a full-time graduate student. It has been an amazing opportunity and something for which I will be eternally grateful.

Robert B. LaRue

Table of Contents

	Page
Abstract	iv
Acknowledgements	v
List of Figures	viii
List of Tables	xi
I. Introduction	1
II. Background	4
2.1 Relative Motion and Formation Flying	4
2.2 Satellite Formations	6
2.2.1 PCO and GCO Formations	6
2.2.2 Along-Track Orbits	9
2.3 Orbit Element Sets	10
2.4 Orbit Element Differences	13
2.5 Orbital Perturbations	14
2.5.1 Perturbations due to an Aspherical Gravity Field	15
2.5.2 Perturbations due to Atmospheric Drag	16
2.6 Mean Orbit Elements	18
2.7 Small Satellites	21
2.8 State Transition Matrix	22
2.9 Maneuvering Techniques	23
2.9.1 Impulsive Maneuvering	24
2.9.2 Continuous-Thrust Maneuvering	25
2.10 Propulsion Technologies	26
2.10.1 Chemical Propulsion	27
2.10.2 Electrical Propulsion	27
III. Methodology	29
3.1 Formation Design	29
3.2 Impulsive Formation Control	34
3.2.1 Impulsive Maneuvering Algorithm	35
3.2.2 Impulsive Formation Maintenance Algorithm	37
3.3 Continuous-Thrust Formation Control	39
3.4 Coordinate Transformations	41
3.4.1 ECI to Hill Frame Transformation	41

	Page
3.4.2 Hill Frame to ECI Transformation	42
3.4.3 Determining ECI Position and Velocity from Equino- cial Elements	45
3.5 Initial Conditions for Formation Initialization	47
3.6 Numerical Propagation of Solution	57
3.7 Algorithm Overview	59
IV. Results	61
4.1 Formation Initialization	61
4.1.1 Impulsive-Thrust Initialization	61
4.1.2 Low-Thrust Initialization	63
4.2 Formation Reconfiguration	68
4.2.1 Impulsive-Thrust Reconfiguration	68
4.2.2 Low-Thrust Reconfiguration	75
4.3 Drag Considerations	79
V. Conclusion	84
5.1 Contributions and Key Findings	84
5.2 Limitations of the Algorithms	85
5.3 Recommendations for Future Work	86
Appendix A. State Transition Matrix	88
Appendix B. Additional Results	90
Bibliography	96

List of Figures

Figure		Page
1.	Hill Frame	5
2.	PCO Relative Orbit Geometry at $t = 0$	8
3.	GCO Relative Orbit Geometry at $t = 0$	9
4.	Orbit Orientation	11
5.	Categories of Small Satellites	21
6.	Impulsive Maneuver	25
7.	Spacecraft Velocity Relative to ECI Frame	43
8.	CSD Ejection Velocity	47
9.	PCO Initialization Maneuver With $N = 2$, $\Delta t_{max} = 3$ Orbits	62
10.	PCO Initialization Maneuver With $N = 2$, $\Delta t_{max} = 1$ Orbit	63
11.	PCO Initialization Maneuver With $N = 3$, $\Delta t_{max} = 3$ Orbits	64
12.	PCO Initialization Maneuver With $N = 5$, $\Delta t_{max} = 5$ Orbits	64
13.	PCO Initialization Maneuver With $N = 5$, $\Delta t_{max} = 8$ Orbits	65
14.	PCO Initialization Maneuver With $N = 5$, $\Delta t_{max} = 8$ Orbits, Closed-Loop Feedback	65
15.	Low-Thrust PCO Initialization Maneuver, $\Delta t = 4.5$ Orbits	66
16.	Low-Thrust PCO Initialization Maneuver, $\Delta t = 8$ Orbits	67
17.	Low-Thrust PCO Initialization Maneuver, $\Delta t = 20$ Orbits	67
18.	1 km \rightarrow 2 km GCO Reconfiguration with $\Delta t_{max} = 3$ orbits, $N = 2$	69
19.	1 km \rightarrow 2 km GCO Reconfiguration with $\Delta t_{max} = 3$ orbits, $N = 3$	69
20.	1 km \rightarrow 2 km GCO Reconfiguration with $\Delta t_{max} = 3$ orbits, $N = 4$	70
21.	1 km \rightarrow 2 km GCO Reconfiguration with $\Delta t_{max} = 3$ orbits, $N = 5$	70
22.	1 km \rightarrow 2 km GCO Reconfiguration with $\Delta t_{max} = 5$ orbits, $N = 5$	70
23.	2 km \rightarrow 1 km GCO Reconfiguration with $\Delta t_{max} = 3$ orbits, $N = 2$	71
24.	1 km \rightarrow 3 km GCO Reconfiguration with $\Delta t_{max} = 3$ orbits, $N = 2$	72

Figure		Page
25.	GCO Formation Reconfiguration Results Using Impulsive-Thrust	72
26.	Approximate Linear Relationship For Impulsive GCO Reconfiguration	73
27.	1 km \rightarrow 2 km ATO Reconfiguration with $\Delta t_{max} = 3$ orbits, $N = 2$	74
28.	1 km \rightarrow 2 km ATO Reconfiguration with $\Delta t_{max} = 3$ orbits, $N = 3$	74
29.	1 km \rightarrow 2 km ATO Reconfiguration r with $\Delta t_{max} = 3$ orbits, $N = 4$	75
30.	1 km \rightarrow 2 km ATO Reconfiguration with $\Delta t_{max} = 3$ orbits, $N = 5$	75
31.	1 km \rightarrow 2 km ATO Reconfiguration with $\Delta t_{max} = 5$ orbits, $N = 5$	76
32.	1 km \rightarrow 2 km Low-thrust GCO Reconfiguration Maneuver . . .	76
33.	1 km \rightarrow 3 km Low-Thrust GCO Reconfiguration Maneuver . .	77
34.	1 km \rightarrow 2 km Low-Thrust GCO Reconfiguration Maneuver with 500 kg, 23 mN Thrust Satellite	77
35.	1 km \rightarrow 2 km Low-Thrust GCO Reconfiguration Maneuver with 10 kg, 4 mN Thrust Satellite	78
36.	1 km \rightarrow 3 km Low-Thrust GCO Reconfiguration Maneuver with 10 kg, 4 mN Thrust Satellite	79
37.	0.5 km \rightarrow 1 km Low-Thrust GCO Reconfiguration Maneuver .	79
38.	1 km PCO Initialization Maneuver with Worst-Case Differential Drag	81
39.	1 km PCO Initialization Maneuver with Worst-Case Differential Drag, 6 Impulses	81
40.	1 km PCO Initialization Maneuver with Worst-Case Differential Drag using Low-Thrust, $\Delta t = 4.5$ orbits	82
41.	1 km PCO Initialization Maneuver with Worst-Case Differential Drag using Low-Thrust, $\Delta t = 8$ orbits	82
42.	1 km PCO Initialization Maneuver with Worst-Case Differential Drag using Low-Thrust, $\Delta t = 20$ orbits	83
43.	1 km \rightarrow 2 km PCO Reconfiguration with $\Delta t_{max} = 3$ orbits, $N = 2$	90
44.	1 km \rightarrow 2 km PCO Reconfiguration with $\Delta t_{max} = 3$ orbits, $N = 3$	90

Figure		Page
45.	1 km \rightarrow 2 km PCO Reconfiguration with $\Delta t_{max} = 3$ orbits, $N = 4$	91
46.	1 km \rightarrow 2 km PCO Reconfiguration with $\Delta t_{max} = 3$ orbits, $N = 5$	91
47.	1 km \rightarrow 2 km PCO Reconfiguration with $\Delta t_{max} = 5$ orbits, $N = 5$	92
48.	1 km \rightarrow 2 km Low-Thrust PCO Reconfiguration Maneuver . .	92
49.	1 km \rightarrow 3 km Low-Thrust PCO Reconfiguration Maneuver . .	93
50.	1 km \rightarrow 2 km Low-Thrust PCO Reconfiguration Maneuver with 500 kg, 23 mN Thrust Satellite	93
51.	1 km \rightarrow 2 km Low-Thrust PCO Reconfiguration Maneuver with 10 kg, 4 mN Thrust Satellite	94
52.	1 km \rightarrow 3 km Low-Thrust PCO Reconfiguration Maneuver with 10 kg, 4 mN Thrust Satellite	94
53.	0.5 km \rightarrow 1 km Low-Thrust PCO Reconfiguration Maneuver .	95

List of Tables

Table		Page
1.	Exponential Density Model	17
2.	Summary of PCO and GCO Initial Conditions	34
3.	Spacecraft Parameters	66
4.	1 km \rightarrow 2 km PCO Reconfiguration Maneuver Results	69
5.	PCO Reconfiguration Using Low Thrust	79

ALGORITHMS FOR SMALL SATELLITE FORMATION FLYING

I. Introduction

With the miniaturization of computers and satellite components, the achievable performance of small satellites (SmallSats) is rapidly increasing. Such technological developments make it possible for SmallSats to perform missions that previously required larger and more expensive satellites. Greater access to space at lower cost will make it possible for universities and small companies to launch satellite networks and space exploration missions. Cube satellites (CubeSats) in particular can be developed rapidly for low cost, and have seen ever-increasing use since their introduction by Stanford and Cal-Poly in 1999 [1] [2]. Originally proposed as a low-cost method to get students involved in space, CubeSats have evolved into a flourishing area of research that has potential for a variety of missions. The low-cost access to space that CubeSats provide has intrigued major space companies and government administrations as a way to demonstrate new technologies or perform missions that are not feasible with larger satellites [3].

A satellite formation is defined by NASA's Goddard Space Flight Center (GSFC) as "The tracking or maintenance of a desired relative separation, orientation or position between or among spacecraft" [4]. Formation flying has many potential applications in which a formation of spacecraft work together to accomplish a task that would otherwise require a significantly larger or more complex spacecraft. One such application is distributed sensing, where a satellite formation could achieve performance that would conventionally require a massive radar or telescope. Satellite formations also allow for greater reliability and resiliency, as it would be much easier to replace a malfunctioning satellite than it would be to repair a component on a larger satellite.

A number of formation flying missions have been conducted to date, such as the Magnetospheric Multiscale (MMS) mission [5] [6], and the Prototype Research Experiments and Space Mission Technology Advancement (PRISMA) [7], among others. There have also been CubeSat formation flying missions, such as AeroCube-4 [8], which demonstrated formation flying by changing the satellites' drag coefficient to reconfigure the formation over a period of weeks. CubeSat Proximity Operations Demonstration (CPOD) [9] aims to demonstrate proximity operations and docking using two 3U CubeSats. The CanX-4 and CanX-5 spacecraft demonstrated precision formation flying using picosatellites, including projected circular orbit (PCO) formations [10]. An overview of many current and future CubeSat formation flying missions can be found in [8].

While there are benefits to using a formation of satellites as opposed to a single spacecraft, there are several technical difficulties that arise. Accurate control of the formation geometry is a necessity for mission success in many cases. For applications such as distributed sensing, where the spacecraft in the formation work together to perform the function of a radar or telescope, it may be desirable to resize the formation periodically to change the resolution of the distributed system. This is an example of a formation reconfiguration problem.

There have been numerous studies on the reconfiguration of satellite relative orbits. Vaddi et al. developed an analytical two-impulse control scheme to transfer a deputy between given initial and final configurations [11], including unperturbed PCO and GCO (General Circular Orbit) formations. Palmer investigated relative low-thrust transfers for Keplerian orbits [12]. Vignal and Pernicka examined the performance of linear vs. nonlinear controllers for low-thrust formation keeping [13]. Yan and Alfriend used the Gim-Alfriend state transition matrix [14] to analytically derive low-thrust control laws for perturbed relative motion [15]. Cho and Park developed a computationally efficient solution to the reconfiguration problem that does not require inverting the fundamental dynamics matrix [16]. Lee and Park provided an analytical solution to the low-thrust formation reconfiguration problem including dif-

ferential gravity, J_2 , and chief eccentricity [17]. Massari and Bernelli-Zazzera derived optimal low-thrust control laws subject to multiple constraints using the interior-point method [18]. Cho, Park, Yoo, and Choi derived an analytical solution for formation reconfigurations on elliptical reference orbits using the Tschauner-Hempel equations [19] [20]. These and other studies have provided crucial insight into the dynamics and control of the formation reconfiguration problem.

The work presented in this thesis will leverage the literature to build algorithms for formation initialization, reconfiguration, and maintenance. These algorithms will be used to analyze a variety of scenarios involving small satellite formation flying. The goal is to examine the tradespace and determine how spacecraft characteristics such as thrust, mass, and specific impulse affect formation flying maneuvers. Initial conditions will be chosen to simulate realistic scenarios [21] [22]. The effectiveness of the guidance and control algorithms will be assessed by a numerical propagation using absolute equations of motion with J_2 and drag effects included, to capture the full nonlinear equations of motion and major perturbations.

To summarize, the goals of the research presented are as follows:

1. Develop an algorithm for formation flying that accounts for situations unique to SmallSats
2. Compare and evaluate a variety of formation types
3. Examine design tradespace to see how spacecraft parameters affect formation flying scenarios

This Introduction chapter will be followed by a Background chapter, which summarizes the concepts that form the foundation for the work presented in this thesis. Next is the Methodology chapter, which will outline the developed algorithms and present the overall process for obtaining solutions. The Results chapter shows simulation outcomes to quantify the performance of the algorithms. Finally, the Conclusion will summarize the Results and state the significant outcomes of the research.

II. Background

This chapter will review the basic principles that form the foundation for the research presented in this thesis.

2.1 *Relative Motion and Formation Flying*

One of original models for satellite relative motion is the Hill/Clohessy-Wiltshire (HCW) equations [23] [24]. These equations were originally derived for rendezvous and docking in the early space program. The homogenous form of the HCW equations is provided below:

$$\ddot{x} - 2n\dot{y} - 3n^2x = 0 \quad (1)$$

$$\ddot{y} + 2n\dot{x} = 0 \quad (2)$$

$$\ddot{z} + n^2z = 0 \quad (3)$$

where n is the chief satellite mean motion and x , y , and z are the Hill frame components (Fig. 1). These are linearized equations of motion that make several assumptions, such as zero chief eccentricity, no perturbation forces, and that the deputy satellite is close to the chief ($d \ll r$, where d is the distance from the chief to the deputy, and r is the orbit radius of the chief). Despite the assumptions, the HCW equations are an attractive option because they are a set of autonomous equations of motion (they do not explicitly depend on time) with a simple closed form solution [4] [25]:

$$x(t) = 4x_0 + \frac{2\dot{y}_0}{n} + \frac{\dot{x}_0}{n} \sin(nt) - \left(3x_0 + \frac{2\dot{y}_0}{n}\right) \cos(nt) \quad (4)$$

$$y(t) = -(6nx_0 + 3\dot{y}_0)t + \frac{2\dot{x}_0}{n} \cos(nt) + \left(6x_0 + \frac{4\dot{y}_0}{n}\right) \sin(nt) - \frac{2\dot{x}_0}{n} + y_0 \quad (5)$$

$$z(t) = z_0 \cos(nt) + \frac{\dot{z}_0}{n} \sin(nt) \quad (6)$$

where the subscript 0 refers to the initial conditions.

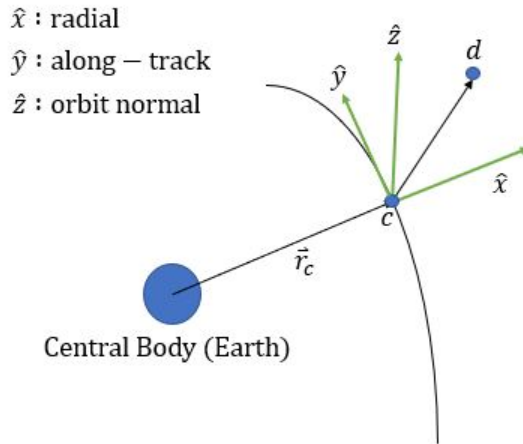


Figure 1: Hill Frame

The HCW equations are typically an acceptable model for modeling relative motion in cases where the chief orbit is very close to circular, the deputy is within a few kilometers of the chief, and forces other than gravity remain small. The inaccuracy of the HCW model will rapidly increase with the degree to which these assumptions are violated. Even in cases where these assumptions hold, predicting motion over long periods of time using the HCW model will be inaccurate due to neglecting perturbation forces, particularly J_2 . There have been numerous efforts in the literature to develop higher fidelity relative motion models that relax the simplifying assumptions used in deriving the HCW equations. For example, the Schweighart-Sedwick model is a linearized relative motion model similar to HCW, but includes J_2 perturbations [26]. Gim and Alfriend developed a state transition matrix (STM) that accommodates an elliptical chief orbit and J_2 perturbations using the geometric method, and provides transformations between Hill components and orbit element differences [14]. There are also models such as the Tschauner-Hempel equations [20] that accommodate chief eccentricity by using true anomaly rather than time as the independent variable. For a thorough overview and comparison of many of the available relative motion models, the reader is referred to [27].

Even though the HCW equations leverage a variety of assumptions, they can still be used to reveal fundamental characteristics about satellite relative motion. Equation (6) demonstrates that the cross-track motion is a simple harmonic. This cross-track oscillation can be negated by choosing $z_0 = \dot{z}_0 = 0$. The first term in Eq. (5) is often referred to as the secular term, as it is the only term in the HCW solution that grows with time (all other t terms are periodic). The secular term results in general instability for in-plane (x - y plane) motion. However, a stable subspace exists under certain conditions where the secular term is eliminated. The initial conditions that eliminate the secular drift are:

$$\dot{y}_0 = -2nx_0 \tag{7}$$

Many formation flying strategies include choosing initial conditions such that Eq. (7) is satisfied, therefore eliminating drift and bounding the motion of the deputy to the chief. It is important to note that initial conditions that satisfy Eq. (7) bound motion only for the HCW model (general bounded motion occurs when the spacecraft in a formation have equal energies). If a higher fidelity model is being used, there are additional constraints that must be used to fully eliminate drift [4]. Stability in the context of the HCW model is local – there are initial conditions that violate Eq. (7) but satisfy global boundedness. In spite of these caveats, there are interesting geometric properties that emerge from the HCW solution. These geometric properties form the basis for PCO and GCO orbits.

2.2 *Satellite Formations*

2.2.1 PCO and GCO Formations. This section will describe the basic characteristics of two particular types of satellite formation - projected circular orbits (PCOs) and general circular orbits (GCOs). A PCO is a trajectory that forms a circular projection onto the y - z (horizontal) plane of the Hill frame. These orbits have a variety of applications for Earth-observing missions, as this formation leads to

equal spacing of the deputy spacecraft in the horizontal plane. A GCO is a trajectory that forms a three-dimensional circle in the Hill frame. This formation type may be suitable for applications where constant spacing between the chief and deputy satellites is desired. Both formations are defined in terms of the phase-magnitude form of the stable subspace HCW solution [4]:

$$x(t) = \rho_x \sin(nt + \alpha_x) \quad (8)$$

$$y(t) = \rho_y + 2\rho_x \cos(nt + \alpha_x) \quad (9)$$

$$z(t) = \rho_z \sin(nt + \alpha_z) \quad (10)$$

These equations are a form of the HCW solution with the initial conditions chosen such that Eq. (7) is satisfied. The variables ρ_x , ρ_y , and ρ_z are magnitude (distance) parameters, and the variables α_x and α_z are phase (angle) parameters. Equations (8) and (9) show a fundamental property of bounded relative motion – the 2:1 in-plane ellipse. The expressions for the bounded relative motion parameters in terms of Hill frame components are presented below:

$$\rho_x = \frac{\sqrt{\dot{x}_0^2 + x_0^2 n^2}}{n} \quad (11)$$

$$\rho_y = y_0 - 2\frac{\dot{x}_0}{n} \quad (12)$$

$$\rho_z = \frac{\sqrt{\dot{z}_0^2 + z_0^2 n^2}}{n} \quad (13)$$

$$\alpha_x = \text{atan2}(nx_0, \dot{x}_0) \quad (14)$$

$$\alpha_z = \text{atan2}(nz_0, \dot{z}_0) \quad (15)$$

where atan2 is the quadrant-specific inverse tangent function. In the special case where $\alpha_x = \alpha_z$ and $\rho_z = \sqrt{3}\rho_x$, the relative orbit is a three-dimensional circle with radius $2\rho_x$ (a GCO) centered at $(0, \rho_y, 0)$. In the case where $\alpha_x = \alpha_z$ and $\rho_z = 2\rho_x$, the relative orbit is a PCO centered at $(0, \rho_y, 0)$. The PCO and GCO constraints

are typically defined with $\rho_y = 0$, to center the formation on the chief. The angle parameters generally do not have any immediate physical significance. However, in the special case of a PCO, α_z is the phase of the deputy satellite in the projected circle (measured from the $+y$ axis) at the time of the chief satellite's equator crossing. Physical significance of the bounded relative motion parameters for a PCO are shown in Fig. 2 [28]. Physical significance of the bounded relative motion parameters for a GCO are shown in Fig. 3.

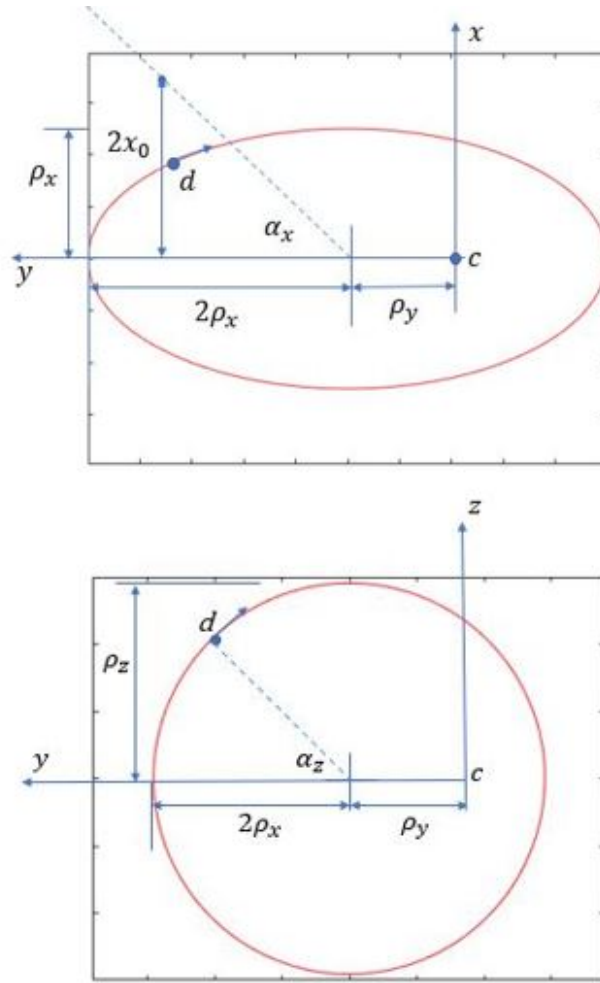


Figure 2: PCO Relative Orbit Geometry at $t = 0$

There are other special cases of bounded relative motion in the literature, but PCOs and GCOs have been the subject of much of the current work. PCOs have been

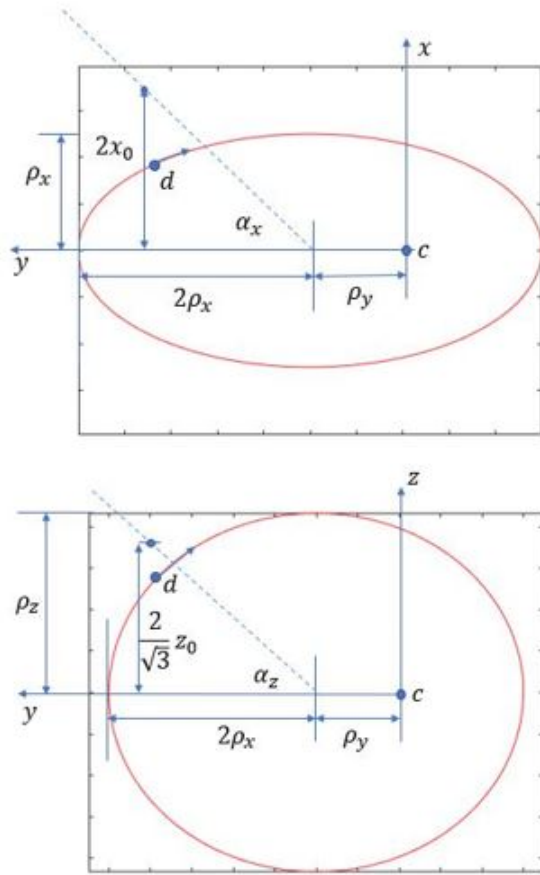


Figure 3: GCO Relative Orbit Geometry at $t = 0$

a particular area of interest, due to their attractive properties and J_2 -invariant nature. Natural perturbations cause a phase rotation $\dot{\alpha}$ in the PCO formation that allow it to be controlled for long periods of time with little fuel cost, as well as balancing fuel consumption of the various satellites in the formation [29] [30]. Much of the analysis presented in the results section will be focused on PCO and GCO formations due to their unique properties and variety of applications.

2.2.2 Along-Track Orbits. Along-track orbits (ATOs) are a type of spacecraft formation where the deputy satellite has an offset in the y -direction of the Hill frame. ATOs are sometimes referred to as “leader-follower” formations. The initial

conditions for an along-track orbit can be characterized as:

$$\bar{X}_0 = \begin{bmatrix} x_0 \\ y_0 \\ z_0 \\ \dot{x}_0 \\ \dot{y}_0 \\ \dot{z}_0 \end{bmatrix} = \begin{bmatrix} 0 \\ y_d \\ 0 \\ 0 \\ 0 \\ 0 \end{bmatrix} \quad (16)$$

where y_d is the desired offset in the y -direction. In the HCW model, an ATO will result in a relative trajectory with $y(t) = y_0$, and $x(t) = z(t) = 0$ (observe Eqs. (4 - 6)). As a result, the relative trajectory will appear to be stationary in the Hill frame. In reality, orbital perturbations and nonlinearities will cause the trajectory to deviate somewhat from the $(0, y_0, 0)$ point.

There are other variants of the ATO where one or more of the deputy satellites are given an offset in the z -direction. In this case, the satellite will have oscillatory cross-track motion, but will still maintain a constant offset in the y -direction (since cross-track motion is decoupled from in-plane motion for the HCW model). This type of modified ATO may be desirable in cases when cross-track separation between satellites is needed. It is worth noting that since the z -motion is oscillatory, the desired cross-track separation would only occur at one point in the orbit.

2.3 *Orbit Element Sets*

There are a variety of available orbit element sets that may be used to characterize a satellite orbit. The classical orbit elements are defined as:

$$\bar{c}l = (a, e, i, h, g, l) \quad (17)$$

where a is the semimajor axis, e is the eccentricity, i is the inclination, h is the right ascension of the ascending node, g is the argument of perigee, and l is the mean

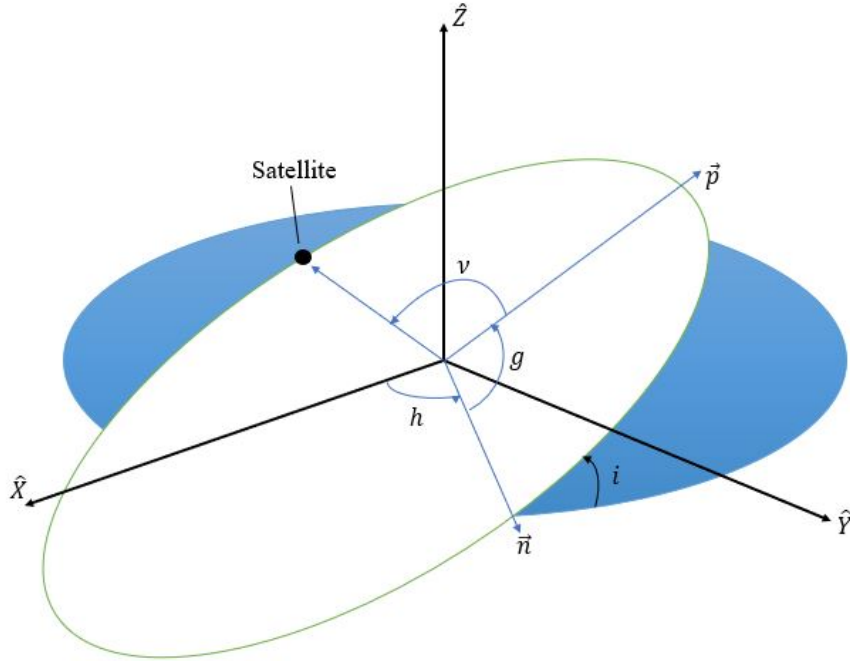


Figure 4: Orbit Orientation

anomaly. The orbit elements a and e define the size and shape of the orbit, while the elements i , h , and g define the orientation of the orbit in space. The mean anomaly l defines the position of the satellite in the orbit. Together, these six elements fully define the trajectory of a satellite. Figure 4 shows the orientation of an orbit in space. \hat{X} , \hat{Y} , and \hat{Z} are respectively the 1-, 2-, and 3-direction of the Earth-centered inertial (ECI) frame. \hat{X} is known as the vernal equinox, or the first point of Aries. \hat{Z} points through the north pole, and $\hat{Y} = \hat{Z} \times \hat{X}$.

The right ascension of the ascending node (h), sometimes simply referred to as the right ascension or the node, is the angle between \hat{X} and the nodal vector \vec{n} . The nodal vector locates the point where the satellite orbit crosses the \hat{X} - \hat{Y} plane from the $-\hat{Z}$ to $+\hat{Z}$ direction. g measures the angle from \vec{n} to the orbit periapsis. i measures the tilt of the orbit plane, and is measured between \hat{K} and the orbit angular momentum vector. The inclination can lie between 0° and 180° . Orbits with inclinations between 0° and 90° are referred to as prograde orbits, as the satellite moves through its orbit in the same direction as the Earth's rotation. Alternatively,

orbits with inclinations between 90° and 180° are retrograde orbits, as the satellite moves through its orbit in the opposite direction of the Earth's rotation. Orbits with inclinations of 0° or 180° are equatorial orbits, the former being prograde and the latter retrograde. An inclination of 90° corresponds to a polar orbit.

The true anomaly ν measures the angle between the satellite and the orbit periapsis. The mean anomaly l is a fictitious angle that measures the angle to the satellite if it moved in a circular orbit with an equal period to the real orbit, and is related to the true anomaly by Kepler's equation. While l may be less intuitive than ν , it has the advantage of a constant rate (the mean motion) in the two-body problem for any elliptical orbit. Either l or ν may be used to define the location of a satellite in its orbit. For the special case of a circular orbit, l and ν are equivalent. For the interested reader who wishes to learn more about the classical orbit elements and Kepler's equation, there are thorough discussions of these topics in refs. [25] and [31].

The classical orbit elements have the advantage of using parameters that all have intuitive significance. However, they are singular for orbits that are circular ($e = 0$) or equatorial ($i = 0$), as g is undefined for the case of circular orbits and h is undefined for equatorial orbits. These singularities make using classical orbit elements impractical, as satellites frequently are placed in orbits where they arise. Geostationary spacecraft are a common example of satellites with orbits that are both circular and equatorial.

The nonsingular elements are an alternative orbit element set that can accommodate circular orbits. These elements are defined as:

$$\bar{n}s = (a, \lambda, i, q_1, q_2, h) \tag{18}$$

where $\lambda = l + g$, $q_1 = e \cos g$, and $q_2 = e \sin g$. It is important to note that the nonsingular elements are still singular for equatorial orbits, as h is undefined in this case. In order to accommodate orbits that are both circular and equatorial, the

equinoctial elements may be used. The equinoctial elements are defined as:

$$\bar{e}q = (a, \Lambda, \tilde{q}_1, \tilde{q}_2, p_1, p_2) \quad (19)$$

where $\Lambda = l + g + h$, $\tilde{q}_1 = e \cos(g + h)$, $\tilde{q}_2 = e \sin(g + h)$, $p_1 = \tan(i/2) \cos h$, and $p_2 = \tan(i/2) \sin h$. The equinoctial elements have a singularity for retrograde equatorial orbits ($i = 180$ deg), but there are alternative formulations that account for this case [32]. However, an Earth satellite has not yet been launched into this orbit [33], so the equinoctial elements are typically considered a singularity-free element set. The notation for the equinoctial elements is not universally standardized, so it is important to understand which definition is being used for each case. Equinoctial elements have the advantage of the least amount of singularities of the presented element sets, but the disadvantage of orbit elements whose physical significance is not intuitive. In general, the equinoctial elements are more difficult to work with than classical or nonsingular elements, as they tend to lead to complicated algebraic expressions. It is for this reason that nonsingular elements are generally preferable to equinoctial elements for the case of inclined circular orbits.

Three sets of orbit elements have been presented here, but there are a multitude of orbit element sets available in the literature, each with their own unique set of advantages and disadvantages. For a review of the available orbit element sets, the reader is referred to refs. [34] and [28].

2.4 Orbit Element Differences

The relative orbit of a satellite can be characterized using orbit element differences:

$$\delta \bar{o}e = \bar{o}e_d - \bar{o}e_c \quad (20)$$

where $\bar{o}e_d$ are the orbit elements of the deputy and $\bar{o}e_c$ are the orbit elements of the chief. Note that $\bar{o}e$ can be any of the presented orbit element sets ($\bar{c}l$, $\bar{n}s$, or $\bar{e}q$). Given the chief orbit elements $\bar{o}e_c$ and the element differences, the position of

the deputy at any time can be solved for using Kepler’s equation (or an appropriate modified version). Equation (20) makes no assumptions about the chief satellite orbit, nor does it require that the deputy be in close proximity to the chief. The Hill frame state vector has six fast variables (variables that change with time), while the orbit element sets only have one (l , λ , or Λ) in the two-body problem, thus simplifying the the satellite position computation.

There are inferences that can be made about a relative trajectory described using orbit element differences that require no computation. The δi and δh of a deputy satellite determine the magnitude of its cross-track motion. Differences in semimajor axis (δa) result in the chief and deputy satellite having a different period, causing them to drift apart [35]. For the case of the two-body problem, a δa of zero will result in no relative drift. It is for this reason that the equation of constraint $\delta a = 0$ is equivalent to Eq. (7). However, a modified version of this constraint must be chosen in the presence of perturbations.

2.5 *Orbital Perturbations*

The motion of a spacecraft is primarily governed by the gravity of the primary body which it orbits. This motion can be described using the two-body equation:

$$\ddot{\vec{r}} = -\frac{\mu}{r^3}\vec{r} \tag{21}$$

where μ is the gravity parameter of the primary body, and \vec{r} is the vector from the center of the primary body to the spacecraft ($r = \|\vec{r}\|$). Equation (21) relies on several assumptions, namely that the mass of the spacecraft is negligible compared to the central body, the chosen coordinate system is inertial, the primary body is spherically symmetric with uniform density, and no forces act on the system other than gravity between the spacecraft and the primary body. For the case of Earth-orbiting spacecraft, the first two of these assumptions can generally be assumed to be true. However, the latter two are not – the Earth is not a perfect sphere, and there

are a variety of forces that act on the system other than the force of gravity between the two bodies. As long as these forces are small compared to the two-body gravity, they can be modeled as perturbations (small deviations) from two-body gravity. In this case, equation 21 can be modified:

$$\ddot{\vec{r}} = -\frac{\mu}{r^3}\vec{r} + \vec{a}_d \quad (22)$$

where \vec{a}_d are the disturbances (perturbations) from the two-body trajectory. Examples of typical perturbations are an aspherical gravity field (J_2), atmospheric drag, third-body gravity (sometimes called lunisolar perturbations in Earth orbit), and solar radiation pressure. These perturbations are present for all Earth-orbiting spacecraft, but the importance of each is varied depending the spacecraft's orbit regime. In low-Earth orbit (LEO), the largest perturbations are due to aspherical gravity and atmospheric drag. At higher altitudes such as geosynchronous orbits (GEO), atmospheric drag is not a major concern, but solar radiation pressure and third-body gravity from the Sun and Moon have a significant effect.

2.5.1 Perturbations due to an Aspherical Gravity Field. The analysis presented in this thesis is focused on SmallSats in low-Earth orbit (LEO). In LEO, J_2 is typically the largest perturbation, followed by atmospheric drag. In many cases, modeling only J_2 perturbations is a reasonable approximation of reality for spacecraft in LEO. J_2 is a zonal harmonic term due to the Earth's equatorial bulge, and is the largest aspherical gravity perturbation term (by several orders of magnitude). The acceleration component due to J_2 can be modeled as [36]:

$$\vec{a}_{J_2} = -\frac{3}{2}J_2\frac{\mu}{r^2}\left(\frac{R_e}{r}\right)^2 \begin{bmatrix} \left(1 - 5\left(\frac{Z}{r}\right)^2\right)\frac{X}{r} \\ \left(1 - 5\left(\frac{Z}{r}\right)^2\right)\frac{Y}{r} \\ \left(3 - 5\left(\frac{Z}{r}\right)^2\right)\frac{Z}{r} \end{bmatrix} \quad (23)$$

where R_e is the radius of the Earth and X , Y , and Z are the position components in the Earth-centered inertial (ECI) reference frame (Fig. 4). Equation (23) can be

inserted as part of the \vec{a}_d term in Eq. (22) to account for J_2 perturbations. In certain cases where a high degree of accuracy is desired, it may be necessary to augment Eq. (23) to account for additional spherical harmonics.

2.5.2 Perturbations due to Atmospheric Drag. The perturbation due to drag can be modeled as:

$$\vec{a}_{aero} = -\frac{1}{2}\zeta\frac{C_D S}{m}\|\vec{v}_{rel}\|\vec{v}_{rel} \quad (24)$$

where ζ is the density of the atmosphere, C_D is the spacecraft drag coefficient, S is the projected area (surface area of spacecraft exposed to drag), m is the spacecraft mass, and \vec{v}_{rel} is the velocity relative to the atmosphere. C_D is determined by the spacecraft design, but can typically be approximated as $C_D = 2.2$ [25]. S is a function of both the spacecraft design and its attitude (how it is oriented in space). \vec{v}_{rel} can be found in terms of ECI components using the following equation:

$$\vec{v}_{rel} = \vec{v} - (\vec{\omega}_E \times \vec{r}) \quad (25)$$

where \vec{r} and \vec{v} are respectively the ECI position and velocity, and $\vec{\omega}_E$ is the rotation rate of the Earth. Assuming an atmosphere that rotates with the Earth, $\vec{\omega}_E$ can be expressed in terms of ECI components as:

$$\vec{\omega}_E = \begin{bmatrix} 0 \\ 0 \\ \omega_E \end{bmatrix} \quad (26)$$

where $\omega_E = 7.2921158553 \times 10^{-5}$ rad/s [36].

Equation (24) can be inserted as part of the \vec{a}_d term in Eq. (22) to capture the effect of aerodynamic (drag) perturbations. While Eq. (24) is a simple expression, accurately modeling drag effects on satellites is a challenging prospect and an area of ongoing research. The challenge in accurately modeling drag is largely due to the difficulty in estimating the density (ζ). Atmospheric density has seasonal variations,

and is highly dependent on the current solar flux and Earth geomagnetic activity, both of which are difficult to predict accurately. A discussion of many of the factors at play when determining density can be found in ref. [25].

For the research presented in this thesis, the density is estimated using an exponential model. This model only considers altitude variations, and assumes a static (time-independent), axially symmetric atmosphere. In this case the density can be estimated as:

$$\zeta = \zeta_{ref} \exp\left(-\frac{\gamma - \gamma_{ref}}{\Gamma}\right) \quad (27)$$

where γ is the current altitude, γ_{ref} is the reference altitude, ζ_{ref} is the reference density, and Γ the scale height. These parameters can be found in Table 1 [36]. Using Eq. (27) and Table 1, the density can be estimated as a function of γ , which

Table 1: Exponential Density Model

γ (km)	γ_{ref} (km)	ζ_{ref} (kg/m ³)	Γ (km)
200-250	200	2.789×10^{-10}	38.5
250-300	250	7.248×10^{-11}	46.9
300-350	300	2.418×10^{-11}	52.5
350-400	350	9.158×10^{-12}	56.4
400-450	400	3.725×10^{-12}	59.4
450-500	450	1.585×10^{-12}	62.2
500-600	500	6.967×10^{-13}	65.8
600-700	600	1.454×10^{-13}	79.0
700-800	700	3.614×10^{-14}	109.0
800-900	800	1.170×10^{-14}	164.0
900 - 1,000	900	5.245×10^{-15}	225.0
> 1,000	1000	3.019×10^{-15}	268.0

can be approximated as $\gamma = r - R_E$. Then, Eq. (24) can be used to estimate the drag perturbation. The non-standard notation for density (ζ) and height (γ) in this thesis is used to prevent any potential ambiguity with the bounded relative motion parameter ρ or the orbit element h .

For satellite formations of identical spacecraft with the same attitude, the differential drag (difference of drag force on the satellites) is essentially zero. In this case, the spacecraft will have the same C_D , S , and m , and the differences in ζ and

\vec{v}_{rel} for the various satellites in the formation will be minuscule. This means that for formations with identical design and attitude, the only effect drag will have on the formation is the degradation of the reference (chief satellite) orbit.

However, there may be cases where there are formations with spacecraft whose design is not identical, or which are unable to have the same attitude. In this case, it is desirable to model the net effect of drag on the formation. The method implemented in this thesis is not high-fidelity, but it does provide a reasoned estimate of differential drag effects.

2.6 Mean Orbit Elements

In the two-body problem, the only classical orbit element that varies with time is the anomaly (l or ν). The other five elements (a , e , i , h , and g) are constant. However, in reality orbital perturbations cause these elements to vary with time. These time-varying elements are referred to as the osculating elements.

Alternatively, mean orbit elements are orbit elements with the short period (on the order of one orbit period) and long period (approximately one order higher than one orbit period) effects averaged out. This property will be briefly demonstrated in the following development [4]. The Delaunay variables are defined as:

$$\bar{D} = (l, g, h, L, GH) \quad (28)$$

where $L = \sqrt{\mu a}$, $G = \sqrt{\mu a(1 - e^2)}$, and $H = G \cos i$. The variables l , g , and h in this case become generalized coordinates, and L , G , and H are their conjugate momenta. The Delaunay elements are a set of canonical variables, meaning that they satisfy Hamilton's equations:

$$\dot{g} = \frac{\partial \mathcal{H}}{\partial G}, \quad \dot{i} = \frac{\partial \mathcal{H}}{\partial L}, \quad \dot{h} = \frac{\partial \mathcal{H}}{\partial H} \quad (29)$$

$$\dot{G} = -\frac{\partial \mathcal{H}}{\partial g}, \quad \dot{L} = -\frac{\partial \mathcal{H}}{\partial l}, \quad \dot{H} = -\frac{\partial \mathcal{H}}{\partial h} \quad (30)$$

The two-body Hamiltonian in terms of Delaunay variables is [4] [33]:

$$\mathcal{H}_0 = -\frac{\mu^2}{2L^2} \quad (31)$$

This further demonstrates the fact that the mean anomaly l is the only non-constant orbit element for the two-body problem, as all of the coordinates and the conjugate momenta G and H do not appear in the two-body Hamiltonian. However, these results are no longer valid in the presence of perturbations, as the Hamiltonian becomes:

$$\mathcal{H} = \mathcal{H}_0 + \epsilon\mathcal{H}_1 \quad (32)$$

where \mathcal{H}_1 is the perturbing Hamiltonian and ϵ is the perturbation. In this case, $\epsilon = -J_2$, and the perturbed Hamiltonian is [4]:

$$\mathcal{H}_1 = \frac{\mu^4 R_e^2}{4L^6} \left(\frac{a}{r}\right)^3 \left[\left(3\frac{H^2}{G^2} - 1\right) + 3\left(1 - \frac{H^2}{G^2}\right) \cos\theta \right] \quad (33)$$

where θ is the argument of latitude ($\theta = \nu + g$). Note that \mathcal{H} is now a function of all of the coordinates and momenta except for h . Therefore, none of the coordinates or momenta except for H will be constant.

Dirk Brouwer used the von Zeipel method in 1959 to average the Hamiltonian in order to remove the periodic terms [37]. A simplified result of his original work is presented here (Brouwer's work included higher-order terms in the geopotential). First the Hamiltonian is averaged with respect to l to remove the short-period terms, then with respect to g to remove the long-period terms. If the distances are normalized by the Earth radius, and time normalized by the mean motion of a satellite at one Earth radius, the averaged Hamiltonians in terms of normalized units become [4]:

$$\bar{\mathcal{H}}_0 = -\frac{1}{2\bar{L}^2} \quad (34)$$

$$\bar{\mathcal{H}}_1 = -\frac{1}{4\bar{L}^6} \left(\frac{\bar{L}}{\bar{G}}\right) \left(1 - 3\frac{\bar{H}^2}{\bar{G}^2}\right) \quad (35)$$

where the overhead bar on the Delaunay variables indicates that they are mean elements. The Hamiltonians are now a function of the momenta only (the coordinates are ignorable). This means that the mean coordinate rates and the mean momenta are constant, because the time derivatives of the momenta are zero (in accordance with Hamilton's equations), and the coordinate rates are a function of the momenta only. This demonstrates the benefit to designing satellite formations in the mean element space. In the osculating space, the coordinate rates and momenta are not constant (observe Eq. 33), making it difficult to choose the correct initial values for a formation. The caveat is that the use of mean elements requires a mean-to-osculating transformation in order to get the instantaneous orbit elements. The actual transformation from mean to osculating elements is obtained via a canonical coordinate transformation using generating functions, a concept that will not be discussed in detail here. The interested reader may find discussions of this topic in refs. [38] [39] [33].

Note that the development presented here is only to first-order, meaning that Eq. (32) was truncated after the first expansion term. The perturbed Hamiltonian could be expanded to any number of terms:

$$\mathcal{H} = \mathcal{H}_0 + \epsilon \mathcal{H}_1 + \frac{1}{2} \epsilon^2 \mathcal{H}_2 \dots \quad (36)$$

However, the amount of algebra involving in expanding to higher terms quickly becomes nontrivial. In many cases a first-order expansion in J_2 is adequate, as a second-order J_2 expansion is not necessary unless first-order expansions for higher-order spherical harmonics are also needed [33]. The work done by Brouwer has been extended by Gim and Alfriend, who derived the first-order mean-to-osculating transformation for nonsingular elements [14] and equinoctial elements [40] (the D and D^* matrices in the articles).

2.7 Small Satellites

Small Satellites are traditionally defined as the class of satellites with masses below 500 kg. The SmallSat category can be broken in to four main sub-categories – minisatellites, microsatellites, nanosatellites, and picosatellites [41]. These categories are shown in Fig. 5. CubeSats are a specific type of SmallSat that are built using standardized 10 cm \times 10 cm \times 10 cm cubes (1U). For example, a 6U CubeSat is a satellite where the base structure is six 10-cm cubes. This standardization allows for CubeSats to be developed and launched on a much faster timescale than traditional satellites. CubeSats are typically nanosatellites, but can be in the microsatellite range. For the purposes of this thesis, the term SmallSat can apply to any of the categories of satellite in Fig. 5. The presented analysis will be focused mostly on satellites in the microsatellite and nanosatellite range, with an emphasis on CubeSats.

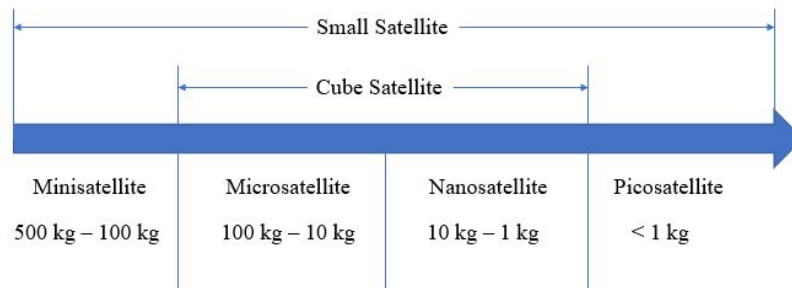


Figure 5: Categories of Small Satellites

Satellites of the sizes illustrated in Fig. 5 tend to lend themselves towards secondary payload launch options, as SmallSats are typically developed on a low-cost budget. Additionally, there are now attractive options such as the Sherpa [21] for SmallSats that provide additional ΔV capability after separation from the primary launch vehicle, giving mission designers more control over the satellite’s final orbit. In the realm of CubeSats, there are standardized options such as the canisterized satellite dispenser (CSD) [22] that allow for relatively simple integration with launch vehicles. These options available to SmallSats allow for quick development times and less testing in comparison to larger satellites.

One drawback is that SmallSats typically have less control over their final orbit than a primary payload. This creates unique problems for the case of SmallSat formation flying, since the spacecraft in the formation often have unfavorable initial conditions, such as a large drift rate, that must be compensated for early in the mission. This is the primary motivation for the formation initialization algorithms that will be developed in the Methodology chapter. Additional challenges for SmallSat missions are low budgets and SWaP (size, weight, and power), which generally translate to less capable subsystems. In effect, the same level of performance cannot be expected of a SmallSat and a large satellite from a high-budget program. This leads to challenges in the context of formation flying, as SmallSats will generally have lower performance in terms of their navigation and propulsion subsystems as compared to larger satellites.

2.8 State Transition Matrix

The state transition matrix (STM) is a matrix that maps the initial state \bar{X}_0 to the final state \bar{X}_f . Another way of describing it is the sensitivity matrix of the current state to the initial conditions. The state transition matrix is defined as [33]:

$$\Phi(t, t_0) = \frac{\partial \bar{X}(t)}{\partial \bar{X}(t_0)} \quad (37)$$

So if the solution is known, the state transition matrix may be written in closed form. The notation $\Phi(t, t_0)$ defines the map from the initial state to the final state. For the rest of this thesis, the initial time t_0 is defined as zero, and the notation Φ_t is used.

For the Hill/Clohessy-Wiltshire model, the state transition matrix is [4]:

$$\Phi_t = \begin{bmatrix} 4 - 3 \cos(nt) & 0 & 0 & \frac{\sin(nt)}{n} & \frac{2}{n} - \frac{2 \cos(nt)}{n} & 0 \\ -6nt + 6 \sin(nt) & 1 & 0 & -\frac{2}{n} + \frac{2 \cos(nt)}{n} & \frac{4 \sin(nt)}{n} - 3t & 0 \\ 0 & 0 & \cos(nt) & 0 & 0 & \frac{\sin(nt)}{n} \\ 3n \sin(nt) & 0 & 0 & \cos(nt) & 2 \sin(nt) & 0 \\ -6n + 6n \cos(nt) & 0 & 0 & -2 \sin(nt) & -3 + 4 \cos(nt) & 0 \\ 0 & 0 & -n \sin(nt) & 0 & 0 & \cos(nt) \end{bmatrix} \quad (38)$$

Notice how the state transition matrix reduces to the identity matrix when $t = 0$. State transition matrices only truly map the initial state to the final state for linear systems. For nonlinear systems, it maps the initial *differential* state to the final differential state. This has applications in perturbation theory, as it can show how initial trajectory errors will evolve over time [35] (departure from a reference trajectory).

Many of the available relative motion models are linear systems. In this case, the state transition matrix can be used to determine the spacecraft state at some future time based on the initial conditions:

$$\bar{X}_t = \Phi_t \bar{X}_0 \quad (39)$$

This makes the state transition matrix a powerful tool for trajectory propagation and maneuver planning, as it is an analytical method that requires no numerical integration. However, it must be noted that any linear relative motion model will be an approximation of the true nonlinear dynamics. Therefore, it is important to be sure that state transition matrices are only used where appropriate.

2.9 Maneuvering Techniques

There are a variety of propulsion methods available for spacecraft mission planners. Broadly, these can be separated into two categories – impulsive maneuvering and continuous-thrust maneuvering. The spacecraft thrust can be modeled as impul-

sive if the thrust is high enough to impart the required velocity change in a nearly instantaneous manner. In reality, all propulsion burns occur over some finite time period. However, it is desirable if possible to model the burns as impulsive, as this greatly reduces the complexity of the analysis.

In cases where the impulsive assumption is not valid, the spacecraft thrust may be modeled as continuous. In this case, the thrust is modeled as an element of the spacecraft dynamics, rather than a discontinuity in the spacecraft velocity [42] [43]. This point will be further emphasized in the following subsections.

2.9.1 Impulsive Maneuvering. In the impulsive maneuvering case, the velocity change of the spacecraft (ΔV) is modeled as a discontinuity in the spacecraft state. This is possible due to the assumption that the velocity change occurs instantaneously (i.e. no time passes during the burn). Consider the state vector of a spacecraft an instant before a maneuver:

$$\bar{X}_0 = \begin{bmatrix} \vec{r}_0 \\ \vec{v}_0 \end{bmatrix} \quad (40)$$

where \vec{r}_0 and \vec{v}_0 are respectively the initial position and velocity vectors of the spacecraft. The spacecraft state an instant after the maneuver can simply be modeled as:

$$\bar{X}_f = \begin{bmatrix} \vec{r}_0 \\ \vec{v}_0 + \Delta\vec{v} \end{bmatrix} \quad (41)$$

where $\Delta\vec{v}$ is the vector form of the velocity change ($\Delta V = ||\Delta\vec{v}||$). The instantaneous nature of the maneuver means that the initial (just before) and final (just after) positions are the same, with jump discontinuities in the velocity.

Consider a general 2-impulse PCO reconfiguration maneuver. The horizontal (y - z plane) component of this maneuver is shown in Fig. (6), with the first maneuver at location “a” and the second maneuver at location “b”. Given the state transition

matrix Φ and the maneuver time t_m , the required ΔV can be solved for as follows:

$$\bar{X}_f = \begin{bmatrix} \vec{r}_f \\ \vec{v}_f \end{bmatrix} = \begin{bmatrix} \vec{0} \\ \Delta\vec{v}_b \end{bmatrix} + \Phi_{t_m} \begin{bmatrix} \vec{r}_0 \\ \vec{v}_0 + \Delta\vec{v}_a \end{bmatrix} \quad (42)$$

In this case, \vec{r} and \vec{v} are respectively the position and velocity of the spacecraft in the Hill frame. The initial and final spacecraft states are known, and the ΔV s are unknown. Therefore, Eq. (42) is a system of six equations with six unknowns that can be solved for to find the required $\Delta\vec{v}$ components. For the impulsive maneuvers in this thesis, the approach of Eq. (42) was modified by setting t_m as a free variable and optimizing for ΔV . This will be elaborated further in the Methodology chapter.

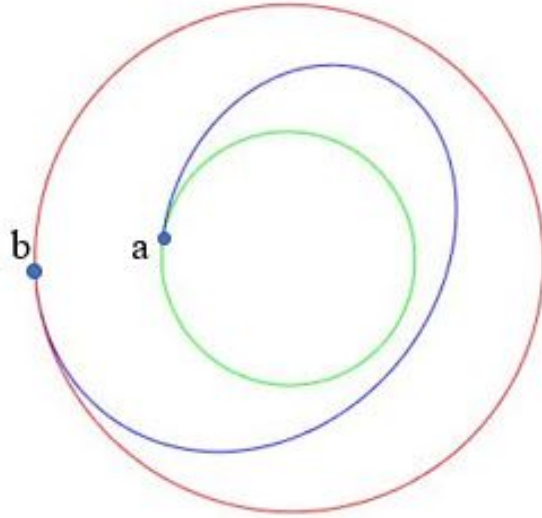


Figure 6: Impulsive Maneuver

2.9.2 Continuous-Thrust Maneuvering. In the case of continuous-thrust maneuvering, the spacecraft thrust is not high enough to impart the required velocity change in an instantaneous manner. Examples of this are low-thrust propulsion technologies such as ion drives or Hall thrusters that often require long burn times to achieve the desired velocity change. Low-thrust technologies of this nature are often

desirable because their high specific impulse (I_{sp}) translates to low fuel consumption as compared to chemical propulsion technologies.

In the continuous-thrust case, an analysis akin to Eq. (42) is no longer valid, as the maneuver can no longer be treated as separate coasting phases with jump discontinuities in the velocity between them. Instead, the thrust is added as a term to the dynamics model:

$$\dot{\bar{X}} = A\bar{X} + B\bar{u} \quad (43)$$

In Eq. (43), A is the state-space matrix, B is the control matrix, and \bar{u} is the control acceleration. The matrix B is simply used to map the components of \bar{u} onto the correct equations of the state-space model.

As can be seen from Eq. (43), determining the required \bar{u} throughout the maneuver is not as straightforward as determining the required $\Delta\vec{v}$ in Eq. (42). There are a variety of techniques that may be implemented to solve the continuous-thrust maneuver problem. In low-thrust cases where the maneuver occurs over a period of multiple orbits, the solution can be obtained by treating the control as a perturbation [44].

Many of the references cited in the Introduction apply a variety of methods to determine continuous-thrust solutions in the context of relative motion. The method that was implemented for the research in this thesis is an LQR (Linear Quadratic Regulation) technique derived by Cho and Park [16], and will be detailed further in the Methodology chapter.

2.10 Propulsion Technologies

There are a variety of propulsion technologies that are available for spacecraft missions. This section will overview two types of propulsion technologies – chemical propulsion and electrical propulsion. Methods such as solar sails and nuclear propulsion will not be discussed. The comparison will be largely focused on performance and design implications. The mechanics of how the different propulsion technologies

operate will not be discussed in detail. For a more complete discussion of electric propulsion types, the reader is referred to [45]. Ref. [41] discusses many of the available propulsion technologies for small satellites. A large amount of the information presented in this section was gleaned from these sources.

2.10.1 Chemical Propulsion. Chemical propulsion is the most commonly implemented method of rocket propulsion, and the only method that is currently feasible for launch vehicles, as alternative methods either do not generate enough thrust or are not safe to operate in the atmosphere. Chemical propulsion methods are also used on probe missions to the outer solar system, as they typically do not require large amounts of power to operate.

Chemical propulsion methods have the advantage of high thrust as compared to other propulsion technologies. It is for this reason that chemical propulsion methods are often favored for large maneuvers, as the amount of time it would take for a low-thrust method to impart the required velocity change is often prohibitive. The disadvantage is that chemical propulsion methods have low specific impulse ratings as compared to electrical propulsion systems. Specific impulses for SmallSat chemical propulsion technologies range from 65 s to 250 s [41].

2.10.2 Electrical Propulsion. Electrical propulsion technologies have the advantage of higher specific impulses than chemical propulsion methods. Typical I_s values for SmallSat technologies range from 700 s to 3000 s [41]. However, electric propulsion methods have much lower thrust ratings than chemical propulsion methods, meaning that maneuver times are long. It is for this reason that electric propulsion devices have typically been used for attitude control or orbit maintenance on large satellites, rather than for performing large maneuvers.

For many small spacecraft, a high specific impulse is necessary to meet ΔV requirements, as space for fuel storage is often limited. This may necessitate the use of electric propulsion as the primary propulsion system. There are a variety of

electric propulsion technologies available, but this section will highlight three types – ion propulsion, Hall thrusters, and electrospray thrusters.

2.10.2.1 Ion Propulsion. Ion propulsion uses plasma generation techniques to ionize large fractions of the propellant, which is typically xenon gas. Ion propulsion devices have the highest efficiency and specific impulse ratings of the presented electric propulsion technologies. Ion propulsion methods also require less power as compared to Hall thrusters.

2.10.2.2 Hall Thrusters. Hall thrusters exploit a phenomenon known as the Hall effect to generate plasma. Like ion propulsion devices, xenon gas is typically used as the propellant. Hall thrusters are less efficient and have lower specific impulse ratings than ion propulsion devices. However, Hall thrusters have the highest thrust of the presented electric propulsion methods, and are mechanically much simpler than ion propulsion devices. The drawback for Hall thrusters is that they require comparatively large amounts of power to operate. Hall thrusters for SmallSats have power requirements ranging from 175-200 W, while power requirements for SmallSat ion propulsion devices do not exceed 60 W [41].

2.10.2.3 Electrospray Thrusters. Electrospray propulsion devices electrostatically extract and accelerate ions from a conductive salt with a negligible vapor pressure. These devices have somewhat lower thrust ratings than ion propulsion methods, and comparable specific impulse ratings to Hall thrusters. While this may make them seem unappealing from a performance standpoint, electrospray devices have many advantages as compared to the other electric propulsion technologies. One of the biggest advantages for electrospray devices is that the propellant does not need to be pressurized for storage. Additionally, power requirements to operate electrospray devices are comparatively low (< 15 W) [41]. These design advantages make electrospray devices an attractive option for SmallSat applications, where storage space and power are often limited.

III. Methodology

This chapter will outline the methods used to generate the results presented in this thesis. The GCO initial conditions are derived in terms of equinoctial elements, followed by a description of the methods for computing fuel-optimal trajectories. Transformations between ECI and Hill frame components are detailed. Methods are developed for negating relative drift in the context of formation initialization. The full nonlinear equations of motion with perturbations are provided. Finally, a top-level overview of the algorithms is presented to show how the various pieces are connected.

3.1 Formation Design

In order to establish or reconfigure a spacecraft formation, it is necessary to first determine the initial conditions that will result in the desired formation geometry. It is advantageous to express these initial conditions in terms of orbit element differences, as the Hill frame components are all fast variables, making it difficult to determine the correct value at a given point in time. It is worth reiterating that the initial conditions should be used as the mean element differences when designing formations in the presence of perturbations. The PCO and GCO initial conditions in terms of nonsingular elements were derived by Vaddi, Alfriend, Vadali, and Sengupta [11]. Their work was extended by Johnson to derive the PCO initial conditions in terms of equinoctial element differences [28].

The following development will build on the previous work by deriving the GCO initial conditions in terms of equinoctial elements so that GCOs may be used in equatorial orbits. The parameters for bounded relative motion in terms of nonsingular orbit element differences are provided in Eqs. (44-48) [28].

$$\rho_x = a_c \delta e \tag{44}$$

$$\rho_y = a_c (\delta \lambda_0 + \delta h \cos(i_c)) \tag{45}$$

$$\rho_z = a_c \sqrt{\delta i^2 + \delta h^2 \sin^2 i_c} \tag{46}$$

$$\alpha_x = \lambda_{c0} - \text{atan2}(\delta q_2, \delta q_1) - \frac{\pi}{2} \quad (47)$$

$$\alpha_z = \lambda_{c0} + \text{atan2}(-\delta h \sin i_c, \delta i) \quad (48)$$

where the subscript c refers to the chief satellite and the subscript 0 means the value at the initial time. The parameters defined in Eqs. (44 - 48) are the same parameters that were previously given in terms of Hill frame components (11 - 15). The GCO constraints are defined as [11] [4]:

$$\delta a = 0 \quad (49)$$

$$\rho_y = 0 \quad (50)$$

$$\rho_x = \frac{\rho_z}{\sqrt{3}} \quad (51)$$

$$\alpha_x = \alpha + \lambda_{c0} \quad (52)$$

$$\alpha_z = \alpha + \lambda_{c0} \quad (53)$$

where α is the deputy phase angle at the time of the chief satellite's equator crossing. These constraints may then be written in terms of the nonsingular element differences:

$$\delta a = 0 \quad (54)$$

$$-\text{atan2}(\delta q_2, \delta q_1) - \frac{\pi}{2} = \alpha \quad (55)$$

$$\text{atan2}(-\delta h \sin i_c, \delta i) = \alpha \quad (56)$$

$$\delta \lambda_0 + \delta h \cos i_c = 0 \quad (57)$$

$$\delta e = \frac{\rho_z}{a_c \sqrt{3}} \quad (58)$$

$$\sqrt{\delta i^2 + \delta h^2 \sin^2 i_c} = \frac{\rho_z}{a_c} \quad (59)$$

Assuming a circular chief satellite orbit, the eccentricity of the deputy is equal to the eccentricity difference:

$$e_d = \delta e \quad (60)$$

Therefore:

$$\delta e = \sqrt{\delta q_1^2 + \delta q_2^2} \quad (61)$$

The assumption of a circular chief orbit is valid, because GCO (and PCO) formations are defined in terms of the HCW solution. Therefore, they only truly exist for circular chief orbits. However, the GCO (and PCO) initial conditions will result in stable motion for elliptical chief orbits (but the resulting formation will not have the unique properties of a PCO or GCO). Using Eq. (61), and the identity $-\text{atan2}(\delta q_2, \delta q_1) - \frac{\pi}{2} = \text{atan2}(-\delta q_1, -\delta q_2)$, Eq. (55) and Eq. (58) may be re-written:

$$\text{atan2}(-\delta q_1, -\delta q_2) = \alpha \quad (62)$$

$$\sqrt{\delta q_1^2 + \delta q_2^2} = \frac{\rho_z}{a_c \sqrt{3}} \quad (63)$$

Equations (62) and (63), along with Eqs. (56), (57), and (59), are the equations of constraint for a GCO in terms of nonsingular element differences. Equation (54) is the previously discussed no-drift condition, and should be replaced by an appropriate expression in the presence of perturbations [46] [4] [47].

In order to avoid the equatorial orbit singularity associated with nonsingular elements, the equations of constraint may be written in terms of differences in the equinoctial elements. The transformations from nonsingular elements to equinoctial elements are:

$$\lambda = \Lambda - h \quad (64)$$

$$\delta \lambda = \delta \Lambda - \delta h \quad (65)$$

$$i = 2 \text{atan}(\sqrt{p_1^2 + p_2^2}) \quad (66)$$

$$\delta i = \frac{2(p_1 \delta p_1 + p_2 \delta p_2)}{\sqrt{p_1^2 + p_2^2}(1 + p_1^2 + p_2^2)} \quad (67)$$

$$h = \text{atan2}(p_2, p_1) \quad (68)$$

$$\delta h = \frac{p_1 \delta p_2 - p_2 \delta p_1}{p_1^2 + p_2^2} \quad (69)$$

$$\delta q_1 = \frac{1}{\sqrt{p_1^2 + p_2^2}} (\delta h(\tilde{q}_2 p_1 - \tilde{q}_1 p_2) + \delta \tilde{q}_1 p_1 + \delta \tilde{q}_2 p_2) \quad (70)$$

$$\delta q_2 = \frac{-1}{\sqrt{p_1^2 + p_2^2}} (\delta h(\tilde{q}_1 p_1 + \tilde{q}_2 p_2) + \delta \tilde{q}_1 p_2 - \delta \tilde{q}_2 p_1) \quad (71)$$

Assuming zero chief eccentricity:

$$\delta q_1 = \frac{1}{\sqrt{p_1^2 + p_2^2}} (\delta \tilde{q}_1 p_1 + \delta \tilde{q}_2 p_2) \quad (72)$$

$$\delta q_2 = \frac{-1}{\sqrt{p_1^2 + p_2^2}} (\delta \tilde{q}_1 p_2 - \delta \tilde{q}_2 p_1) \quad (73)$$

Using these transformations on Eqs. (56-57, 59, 62-63), and introducing a new phase angle $\alpha_I = \alpha - h_c$, yields the equations of constraint in terms of equinoctial elements and equinoctial element differences. α_I is the deputy phase angle when the chief satellite crosses the 1-direction of the ECI (Earth-Centered Inertial) frame, known as the first point of Aries.

$$\delta \Lambda_0 = \frac{p_{1c} \delta p_2 - p_{2c} \delta p_1}{p_{1c}^2 + p_{2c}^2} [1 - \cos(2 \operatorname{atan}(\sqrt{p_{1c}^2 + p_{2c}^2}))] \quad (74)$$

$$\operatorname{atan2}(-(p_{1c} \delta p_2 - p_{2c} \delta p_1), p_{1c} \delta p_1 + p_{2c} \delta p_2) = \alpha_I + \operatorname{atan2}(p_{2c}, p_{1c}) \quad (75)$$

$$\frac{1}{\sqrt{p_{1c}^2 + p_{2c}^2}} \sqrt{\frac{4(p_{1c} \delta p_1 + p_{2c} \delta p_2)^2}{(1 + p_{1c}^2 + p_{2c}^2)^2} + \frac{(p_{1c} \delta p_2 - p_{2c} \delta p_1)^2}{p_{1c}^2 + p_{2c}^2} \sin^2(2 \operatorname{atan}(\sqrt{p_{1c}^2 + p_{2c}^2}))} = \frac{\rho_z}{a_c} \quad (76)$$

$$\operatorname{atan2}(-(\delta \tilde{q}_1 p_{1c} + \delta \tilde{q}_2 p_{2c}), -(-\delta \tilde{q}_1 p_{2c} + \delta \tilde{q}_2 p_{1c})) = \alpha_I + \operatorname{atan2}(p_{2c}, p_{1c}) \quad (77)$$

Since the chief satellite's orbit is assumed to be circular, $\delta e = e_d$, so the final equation of constraint is:

$$\sqrt{\delta \tilde{q}_1^2 + \delta \tilde{q}_2^2} = \frac{\rho_z}{a_c \sqrt{3}} \quad (78)$$

After some algebra, these equations can be solved to yield the GCO initial conditions in equinoctial element differences:

$$\delta a = 0 \quad (79)$$

$$\delta\tilde{q}_1 = -\frac{\rho_z}{a_c\sqrt{3}} \sin \alpha_I \quad (80)$$

$$\delta\tilde{q}_2 = -\frac{\rho_z}{a_c\sqrt{3}} \cos \alpha_I \quad (81)$$

$$\delta p_1 = \frac{\rho_z}{2a_c} (1 + p_{1c}^2 + p_{2c}^2) \cos \alpha_I \quad (82)$$

$$\delta p_2 = -\frac{\rho_z}{2a_c} (1 + p_{1c}^2 + p_{2c}^2) \sin \alpha_I \quad (83)$$

$$\delta\Lambda_0 = \frac{2(p_{1c}\delta p_2 - p_{2c}\delta p_1)}{1 + p_{1c}^2 + p_{2c}^2} \quad (84)$$

However, it is desirable to express these equations in terms of a more intuitive physical property. Using the knowledge that the radius of a GCO is equal to $2\rho_x$, a variable $\rho = 2\rho_x = \frac{2}{\sqrt{3}}\rho_z$ may be defined. Then, the GCO initial conditions terms of ρ are:

$$\delta\tilde{q}_1 = -\frac{\rho}{2a_c} \sin \alpha_I \quad (85)$$

$$\delta\tilde{q}_2 = -\frac{\rho}{2a_c} \cos \alpha_I \quad (86)$$

$$\delta p_1 = \frac{\sqrt{3}}{4} \frac{\rho}{a_c} (1 + p_{1c}^2 + p_{2c}^2) \cos \alpha_I \quad (87)$$

$$\delta p_2 = -\frac{\sqrt{3}}{4} \frac{\rho}{a_c} (1 + p_{1c}^2 + p_{2c}^2) \sin \alpha_I \quad (88)$$

Equations (85-88), along with Eqs. (79) and (84), will yield the necessary initial conditions in equinoctial element differences to yield a GCO of desired radius ρ and angle α_I . As mentioned previously, Eq. (79) should be replaced by an appropriate term in the presence of perturbations. The δa to negate drift in presence of J_2 perturbations given by Eq. (89) [4]. This constraint is also valid in the two-body problem, as it reduces to $\delta a = 0$ when J_2 vanishes.

$$\delta a = 0.5J_2a_c\left(\frac{R_e}{a_c}\right)^2\left(\frac{3\eta_c + 4}{\eta_c^5}\right)[(1 - 3\cos^2 i_c)\delta\eta - (\eta_c \sin 2i_c)\delta i] \quad (89)$$

where

$$\eta_c = \sqrt{1 - e_c^2} \quad (90)$$

$$\delta\eta = -\frac{e_c \delta e}{\eta_c} \quad (91)$$

The equations for the GCO initial conditions in terms of equinoctial element differences are summarized in Table 2, along with the initial conditions for a GCO in terms of nonsingular elements [11], and the PCO initial conditions in nonsingular and equinoctial elements [11] [28]. For all of the cases in Table 2, an additional equation of

Table 2: Summary of PCO and GCO Initial Conditions

	PCO	GCO
$\bar{n}s$	$\delta\lambda = \frac{\rho \sin \alpha}{a_c \tan i}$ $\delta i = \frac{\rho}{a_c} \cos \alpha$ $\delta q_1 = -\frac{\rho}{2a_c} \sin \alpha$ $\delta q_2 = -\frac{\rho}{2a_c} \cos \alpha$ $\delta h = -\frac{\rho \sin \alpha}{a_c \sin i}$	$\delta\lambda = \frac{\sqrt{3}}{2} \frac{\rho \sin \alpha}{a_c \tan i}$ $\delta i = \frac{\sqrt{3}}{2} \frac{\rho}{a_c} \cos \alpha$ $\delta q_1 = -\frac{\rho}{2a_c} \sin \alpha$ $\delta q_2 = -\frac{\rho}{2a_c} \cos \alpha$ $\delta h = -\frac{\sqrt{3}}{2} \frac{\rho \sin \alpha}{a_c \sin i}$
$\bar{e}q$	$\delta\tilde{q}_1 = -\frac{\rho}{2a_c} \sin \alpha_I$ $\delta\tilde{q}_2 = -\frac{\rho}{2a_c} \cos \alpha_I$ $\delta p_1 = \frac{\rho}{2a_c} (1 + p_{1c}^2 + p_{2c}^2) \cos \alpha_I$ $\delta p_1 = \frac{\rho}{2a_c} (1 + p_{1c}^2 + p_{2c}^2) \sin \alpha_I$ $\delta\Lambda_0 = \frac{2(p_{1c}\delta p_2 - p_{2c}\delta p_1)}{1 + p_{1c}^2 + p_{2c}^2}$	$\delta\tilde{q}_1 = -\frac{\rho}{2a_c} \sin \alpha_I$ $\delta\tilde{q}_2 = -\frac{\rho}{2a_c} \cos \alpha_I$ $\delta p_1 = \frac{\sqrt{3}}{4} \frac{\rho}{a_c} (1 + p_{1c}^2 + p_{2c}^2) \cos \alpha_I$ $\delta p_2 = -\frac{\sqrt{3}}{4} \frac{\rho}{a_c} (1 + p_{1c}^2 + p_{2c}^2) \sin \alpha_I$ $\delta\Lambda_0 = \frac{2(p_{1c}\delta p_2 - p_{2c}\delta p_1)}{1 + p_{1c}^2 + p_{2c}^2}$

constraint (Eq. (89)) is needed to negate relative drift. As was discussed previously, the design parameter ρ defines the radius of a GCO. For PCOs, the parameter ρ defines the radius of the projected circle in the horizontal plane. The parameters α and α_I have the same meaning as discussed previously.

3.2 Impulsive Formation Control

This section will discuss the methods used for the impulsive thrust algorithm. First, the method for formation initialization and reconfiguration will be discussed, followed by a discussion of the formation maintenance algorithm.

3.2.1 *Impulsive Maneuvering Algorithm.* The method used to solve for impulsive thrust maneuvers is a modification of Eq. (42). Rather than specifying the transfer time and solving for the ΔV s, the transfer time was set as a free optimization variable, subject to the inequality constraint:

$$\Delta t_m < \Delta t_{max} \quad (92)$$

where Δt_{max} is the maximum allowable time for the maneuver. A direct optimization routine using MATLAB's *fmincon* function was used to search transfer time values to find the fuel-optimal (ΔV -optimal) maneuver. It is desirable to analyze cases involving more than two burns, so Eq. (42) was programmed recursively for N maneuvers with $N - 1$ coasting arcs:

$$\bar{X}_f = \begin{bmatrix} \vec{r}_f \\ \vec{v}_f \end{bmatrix} = \begin{bmatrix} \vec{0} \\ \Delta \vec{v}_c \end{bmatrix} + \Phi_{\Delta t_{m_2}} \left(\begin{bmatrix} \vec{0} \\ \Delta \vec{v}_b \end{bmatrix} + \Phi_{\Delta t_{m_1}} \left(\begin{bmatrix} \vec{0} \\ \Delta \vec{v}_a \end{bmatrix} + \Phi_{\Delta t_w} \begin{bmatrix} \vec{r}_0 \\ \vec{v}_0 \end{bmatrix} \right) \right) \dots \quad (93)$$

where $\Phi_{\Delta t_{m_i}}$ is the STM for the i th coasting arc, and $\Delta \vec{v}_a, \Delta \vec{v}_b, \Delta \vec{v}_c$ and so on are the N burns. $\Phi_{\Delta t_w}$ is the STM for an initial “wait” coast, since it may not be optimal to begin maneuvering immediately. The equations of constraint are:

$$\bar{X}_f = \bar{X}_{f_d} \quad (94)$$

$$\Delta t_m = \Delta t_w + \sum_{i=1}^{(N-1)} \Delta t_{m_i} < \Delta t_{max} \quad (95)$$

where \bar{X}_{fd} is the desired final state. Δt_w is the time duration of the wait period, and Δt_{m_i} is the duration of the i th coast arc. The optimization state vector is:

$$\bar{x}_{opt} = \begin{bmatrix} \Delta \vec{v}_1 \\ \vdots \\ \Delta \vec{v}_N \\ \Delta t_{m1} \\ \vdots \\ \Delta t_{m_{N-1}} \\ \Delta t_w \end{bmatrix} \quad (96)$$

with the cost function defined as:

$$J = \bar{x}_{opt}^T M \bar{x}_{opt} \quad (97)$$

$$M = \begin{bmatrix} I_{3N} & \vdots \\ \dots & 0_N \end{bmatrix} \quad (98)$$

where I_{3N} is a $3N \times 3N$ identity matrix. Since there are 3 components for each $\Delta \vec{v}$, M is a matrix that maps only the $\Delta \vec{v}$ components to the quadratic cost function. The cost function is minimized, subject to Eqs. (94) and (95), resulting in a minimum-fuel impulsive maneuver.

This algorithm has the advantage of being general. Any number of N impulses could be defined, allowing a wide variety of formation reconfiguration and initialization maneuvers to be analyzed. Additionally, any state transition matrix can be used with this method (as long as the state vector is defined with respect to the model). The disadvantage is that it is not as computationally efficient as an analytic method. The optimization state vector has $4N$ components, so increasing the number of maneuvers rapidly increases the number of optimization variables. This means that simulating cases with large N values is computationally prohibitive. The state transition matrix used for the research in this thesis is the STM for the Schweighart-Sedwick model [26],

in order to capture the effects of J_2 in the targeting dynamics. It is provided in Appendix A.

3.2.2 Impulsive Formation Maintenance Algorithm. The method used for impulsive formation initialization and reconfiguration maneuvers has the advantage of allowing a wide variety of scenarios to be analyzed. While the method could conceivably be used for formation maintenance, it was decided to implement a more computationally efficient approach, since formation maintenance analyses usually require long run times.

The approach used for formation maintenance in the impulsive-thrust case is a discrete-time linear quadratic regulator (DLQR). The method implemented for this thesis is a modified version of the DLQR approach outlined in ref. [4]. A DLQR is a discretized version of the continuous-time linear quadratic regulator (LQR). DLQRs (and LQRs) are an analytic control approach that uses linearized dynamics (such as the HCW or Schweighart-Sedwick equations) and a quadratic cost function. The cost function for the DLQR is given by Eq. (99).

$$J = \sum_{i=0}^n \bar{X}(i)^T Q \bar{X}(i) + \bar{u}(i)^T R \bar{u}(i) \quad (99)$$

where n is the number of time steps, and $\bar{X}(i)$ and $\bar{u}(i)$ are the state and control vectors at the i th time instant. Q and R are respectively the state and control weight matrices. The state and control vectors are subject to the discrete-time state equation:

$$\bar{X}(i+1) = A_d \bar{X}(i) + B_d \bar{u}(i) \quad (100)$$

Note that even though Eq. (100) takes a similar form to Eq. (43), the quantities are fundamentally different. The left side of Eq. (100) is the state at a future time instant, not the state derivative. This means that A_d is not the state-space matrix,

but rather the state transition matrix (assuming impulsive control):

$$A_d = \Phi_{\Delta t} \quad (101)$$

where Δt is the time between instants (the step size). B_d then takes the form:

$$B_d = A_d B = \Phi_{\Delta t} B \quad (102)$$

where B is the same control matrix that was discussed previously. The approximate control law is given by ref. [4]:

$$\vec{u}(i) = -K (\bar{X}(i) - \bar{X}_r(i)) \quad (103)$$

where $K = (B_d S B_d + R)^{-1} B_d^T S A_d$ is the steady-state Kalman gain matrix, and \bar{X}_r is the reference (desired) trajectory. The control \vec{u} when using a DLQR is actually the $\Delta \vec{v}$, rather than a control acceleration vector as in the continuous-time case. S is the solution to the discrete-time algebraic Riccati equation:

$$A_d^T S A_d - S - A_d^T S B_d (B_d^T S B_d + R)^{-1} B_d^T S A_d + Q = 0 \quad (104)$$

Numerical solvers of the discrete-time algebraic Riccati equation (Eq. (104)) are standard in many software packages, such as MATLAB's ¹ *dare* function. The Schweighart-Sedwick STM was used as the A_d matrix, and \bar{X}_r was determined by sampling the reference trajectory of the desired formation at the instant of the impulse application.

The DLQR is an optimal control technique that has the advantage of being a computationally efficient analytic method for formation maintenance. Equation (104) must be solved numerically, but the resulting gain matrix is then constant as

¹MATLAB® is a registered trademark of MathWorks, Inc.

long as the time intervals between impulses remains the same. This means that the discrete-time algebraic Riccati equation only needs to be solved once.

3.3 Continuous-Thrust Formation Control

This section discusses the methodology that was implemented for computing low-thrust solutions in relative motion. The method was taken from Cho and Park [16], with some modifications that were made to constrain the solutions. The reader is encouraged to read ref. [16] for a more comprehensive discussion of the method.

The continuous-thrust control is an LQR (linear-quadratic regulator) approach, assuming three-axis control and a specified transfer time. The method can be implemented for a variety of dynamic models, as long as the model uses linearized dynamics such that the elements of the state-space matrix are related by $A_1 - A_1^T = \dot{A}_2$.

$$A = \begin{bmatrix} 0_3 & I_3 \\ A_1 & A_2 \end{bmatrix} \quad (105)$$

For the research presented in this thesis, the Schweighart-Sedwick model [26] was used to capture the effects of J_2 in the thrust profile calculation. Given the state-space matrix A and state transition matrix Φ for the desired dynamic model, the fuel-optimal control can be calculated using the following equations:

$$S(t) = \int_0^t \Phi_A^T \Phi_A d\tau \quad (106)$$

$$K = \Phi_f^{-1} \bar{X}_f - \Phi_0^{-1} \bar{X}_0 \quad (107)$$

$$C = \Phi_A^T \dot{\Phi}_A - (\Phi_A^T \dot{\Phi}_A)^T - \Phi_A^T A_2 \Phi_A \quad (108)$$

where

$$\bar{X}_t = \Phi_t \bar{X}_0 \quad (109)$$

$$\Phi = \begin{bmatrix} \Phi_A \\ \dot{\Phi}_A \end{bmatrix} \quad (110)$$

$$\bar{X} = \begin{bmatrix} x \\ y \\ z \\ \dot{x} \\ \dot{y} \\ \dot{z} \end{bmatrix} \quad (111)$$

$$\dot{\bar{X}} = A\bar{X} + B\bar{u} \quad (112)$$

$$B = \begin{bmatrix} 0_3 \\ I_3 \end{bmatrix} \quad (113)$$

the cost function is:

$$J = \frac{1}{2} \int_0^t u^T u \, d\tau \quad (114)$$

and the optimal control is:

$$\bar{u}(t) = \Phi_A S_f^{-1} C K \quad (115)$$

The matrices C and K are constant, and S_f is the S matrix evaluated at the final time. Therefore, the optimal control $\bar{u}(t)$ throughout the transfer is a function of $\Phi_A(t)$ only.

The method of Cho and Park was modified by placing constraints on the achievable trajectories. This can be done by bounding the control acceleration by the maximum thrust and initial mass of the spacecraft ($U = \|\bar{u}\|$).

$$U_{max} = \frac{F_{max}}{m_0} \quad (116)$$

The maximum thrust is a constant, and the mass of the spacecraft can only decrease throughout the maneuver. Therefore, the constraint in Eq. (116) is adequate for bounding the control throughout any maneuvers. For long maneuvers with significant changes in spacecraft mass, it may be desirable to update U_{max} throughout the maneuver.

3.4 Coordinate Transformations

In order to be able to effectively implement formation flying algorithms, it is necessary to be able to accurately transform state vectors between inertial and relative motion frames. This section will provide the coordinate transformations between ECI and Hill frame components, and the conversion of equinoctial elements to an ECI state vector.

3.4.1 ECI to Hill Frame Transformation. The relative motion between two satellites in general elliptic orbits can be expressed in the Hill frame as [48]:

$$x = \frac{\delta \vec{r}^T \vec{r}_c}{r_c} \quad (117)$$

$$y = \frac{\delta \vec{r}^T (\vec{H}_c \times \vec{r}_c)}{\|\vec{H}_c \times \vec{r}_c\|} \quad (118)$$

$$z = \frac{\delta \vec{r}^T \vec{H}_c}{H_c} \quad (119)$$

where \vec{H} is the angular momentum vector:

$$\vec{H} = \vec{r} \times \vec{v} \quad (120)$$

and $H = \|\vec{H}\|$. $\delta \vec{r}$ and $\delta \vec{v}$ are respectively the relative displacement and velocity:

$$\delta \vec{r} = \vec{r}_d - \vec{r}_c \quad (121)$$

$$\delta \vec{v} = \vec{v}_d - \vec{v}_c \quad (122)$$

Note that $\delta \vec{r}$ and $\delta \vec{v}$ are simply the difference in the ECI position and velocity between the deputy and chief, not Hill frame components. Equations (117-119) can be differentiated with respect to time to yield the Hill frame velocity components:

$$\dot{x} = \frac{\delta \vec{v}^T \vec{r}_c + \delta \vec{r}^T \vec{v}_c}{r_c} - \frac{(\delta \vec{r}^T \vec{r}_c)(\vec{r}_c^T \vec{v}_c)}{r_c^3} \quad (123)$$

$$\begin{aligned} \dot{y} = & \frac{\delta \vec{v}^T (\vec{H}_c \times \vec{r}_c) + \delta \vec{r}^T (\dot{\vec{H}}_c \times \vec{r}_c + \vec{H}_c \times \vec{v}_c)}{\|\vec{H}_c \times \vec{r}_c\|} \\ & - \frac{\delta \vec{r}^T (\vec{H}_c \times \vec{r}_c) (\vec{H}_c \times \vec{r}_c)^T (\dot{\vec{H}}_c \times \vec{r}_c + \vec{H}_c \times \vec{v}_c)}{\|\vec{H}_c \times \vec{r}_c\|^3} \end{aligned} \quad (124)$$

$$\dot{z} = \frac{\delta \vec{v}^T \vec{H}_c + \delta \vec{r}^T \dot{\vec{H}}_c}{H_c} - \frac{\delta \vec{r}^T \vec{H}_c (\vec{H}_c^T \dot{\vec{H}}_c)}{H_c^3} \quad (125)$$

where $\dot{\vec{H}}_c = \vec{r}_c \times \dot{\vec{v}}_c = \vec{r}_c \times \vec{a}_c$. This means that determining the Hill frame velocities requires knowledge of the chief satellite's acceleration vector, which can be obtained from Eq. (187). Equations (117-119) and (123-124) are the exact transformation from ECI to Hill frame components, and they are valid in the presence of perturbations.

3.4.2 Hill Frame to ECI Transformation. The rotation matrix from the Hill to ECI frame can be expressed as:

$$T = \begin{bmatrix} \hat{r}_c & (\hat{H}_c \times \hat{r}_c) & \hat{H}_c \end{bmatrix} \quad (126)$$

where \hat{r}_c and \hat{H}_c are respectively the unit vectors in the direction of the chief ECI position vector and angular momentum vector. This can be used to rotate the control vector from the Hill to ECI frame:

$$\vec{u}_{ECI} = T \vec{u} \quad (127)$$

Equation (127) can be inserted into Eq. (186) to find the total ECI acceleration of a deputy satellite during a low-thrust maneuver.

A similar process may be used to find the deputy ECI position and velocity from its Hill frame components. Figure 7 shows the orientation of the deputy ECI velocity vector in space.

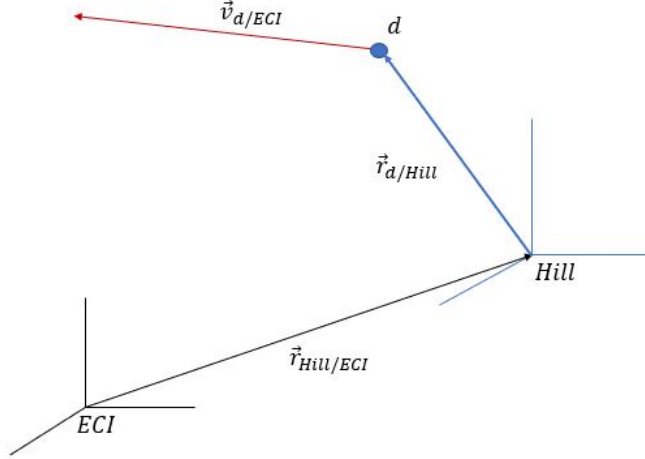


Figure 7: Spacecraft Velocity Relative to ECI Frame

From the transport theorem, the velocity of the deputy with respect to the ECI frame can be expressed as [49]:

$$\vec{v}_{d/ECI} = {}^{Hill}\dot{\vec{r}}_{d/Hill} + \vec{\omega}_{Hill/ECI} \times \vec{r}_{d/Hill} + {}^{ECI}\dot{\vec{r}}_{Hill/ECI} \quad (128)$$

where ${}^{Hill}\dot{\vec{r}}_{d/Hill}$ is the time derivative in the Hill frame of the position of the deputy with respect to the Hill frame, $\vec{\omega}_{Hill/ECI}$ is the angular velocity of the Hill frame with respect to the ECI frame, $\vec{r}_{d/Hill}$ is the position of the deputy with respect to the Hill frame, and ${}^{ECI}\dot{\vec{r}}_{Hill/ECI}$ is the time derivative in the ECI frame of the position of the Hill frame with respect to the ECI frame.

Equation (128) is a coordinate-free representation of the deputy velocity with respect to the ECI frame. If $\vec{v}_{d/ECI}$ and ${}^{ECI}\dot{\vec{r}}_{Hill/ECI}$ are expressed in terms of ECI components, then $\vec{v}_{d/ECI} = \vec{v}_d$ and ${}^{ECI}\dot{\vec{r}}_{Hill/ECI} = \vec{v}_c$, where \vec{v} is a vector of the velocity components of the ECI state. Additionally, if $\vec{r}_{d/Hill}$ and ${}^{Hill}\dot{\vec{r}}_{d/Hill}$ are expressed in terms of Hill frame components, then $\vec{r}_{d/Hill} = \vec{r}_{d_{Hill}}$ and ${}^{Hill}\dot{\vec{r}}_{d/Hill} = \vec{v}_{d_{Hill}}$ (where $\vec{r}_{d_{Hill}}$ and $\vec{v}_{d_{Hill}}$ are respectively the position and velocity components of the Hill-frame state). If $\vec{\omega}_{Hill/ECI}$ is also expressed in terms of Hill frame components, then Eq. (128) can be modified:

$$\vec{v}_d = T\vec{v}_{d_{Hill}} + T(\vec{\omega}_{Hill/ECI} \times \vec{r}_{d_{Hill}}) + \vec{v}_c \quad (129)$$

The deputy ECI position is simply:

$$\vec{r}_d = \vec{r}_c + T\vec{r}_{dHill} \quad (130)$$

Equations (129) and (130) can be used to find the deputy ECI position and velocity, based on the deputy Hill frame state and the chief ECI position and velocity. The only remaining step is to determine $\vec{\omega}_{Hill/ECI}$. In the Hill frame, it can be expressed as:

$$\vec{\omega}_{Hill/ECI} = \begin{bmatrix} \omega_r \\ 0 \\ \omega_n \end{bmatrix} \quad (131)$$

where ω_r and ω_n are respectively the radial and normal components of the angular velocity. In the two-body problem, ω_r is zero, and ω_n is the mean motion. However, J_2 perturbations cause a radial component to exist for the angular velocity, due to nodal regression. ω_r and ω_n can be expressed in terms of equinoctial elements as [40]:

$$\omega_r = -3J_2R_e^2 \frac{2\sqrt{\mu}\sigma_3\tau_2}{a_c^{7/2}\eta^7\sigma_2^2} (1 + \tilde{q}_{1c} \cos(\Psi_c) + \tilde{q}_{2c} \sin(\Psi_c))^3 \quad (132)$$

$$\omega_n = \sqrt{\frac{\mu}{p}} (1 + \tilde{q}_{1c} \cos(\Psi_c) + \tilde{q}_{2c} \sin(\Psi_c)) \quad (133)$$

$\Psi = \nu + g + h$ is the equinoctial element analogous to the true anomaly. Conversions between Λ and Ψ can be done with a modified version of Kepler's equation, which is discussed in the following section. The remainder of the parameters in Eqs. (132) and (133) are [40]:

$$\tau_2 = p_{1c} \sin(\Psi_c) - p_{2c} \cos(\Psi) \quad (134)$$

$$\eta = \sqrt{1 - \tilde{q}_{1c}^2 - \tilde{q}_{2c}^2} \quad (135)$$

$$\sigma_2 = 1 + p_{1c}^2 + p_{2c}^2 \quad (136)$$

$$\sigma_3 = 1 - p_{1c}^2 - p_{2c}^2 \quad (137)$$

$$p = a_c (1 - \tilde{q}_{1c}^2 - \tilde{q}_{2c}^2) \quad (138)$$

The osculating equinoctial elements should be used to calculate ω_r and ω_n , and the parameters τ_2 , η , σ_2 , σ_3 , and p . With ω_n and ω_r defined, Eq. (129) may be rewritten in matrix form:

$$\vec{v}_d = [v_d] = \begin{bmatrix} \dot{X}_d \\ \dot{Y}_d \\ \dot{Z}_d \end{bmatrix} = \begin{bmatrix} \dot{X}_c \\ \dot{Y}_c \\ \dot{Z}_c \end{bmatrix} + T \left(\begin{bmatrix} \dot{x} \\ \dot{y} \\ \dot{z} \end{bmatrix} + \begin{bmatrix} -\omega_n y \\ \omega_n x - \omega_r z \\ \omega_r y \end{bmatrix} \right) \quad (139)$$

The process in this section can also be used to rotate a $\Delta\vec{v}$ into the ECI frame to apply it to the deputy ECI state. This is done by simply updating the deputy Hill frame velocity to include the $\Delta\vec{v}$ before using Eq. (139).

3.4.3 Determining ECI Position and Velocity from Equinoctial Elements.

The ECI position and velocity of a satellite can be expressed in terms of its equinoctial elements as [31]:

$$\vec{r} = X_1 \vec{f} + Y_1 \vec{g} \quad (140)$$

$$\vec{v} = \dot{X}_1 \vec{f} + \dot{Y}_1 \vec{g} \quad (141)$$

where

$$\vec{f} = \frac{1}{1 + p_1^2 + p_2^2} \begin{bmatrix} 1 - p_2^2 + p_1^2 \\ 2p_1 p_2 \\ -2p_2 \end{bmatrix} \quad (142)$$

$$\vec{g} = \frac{1}{1 + p_1^2 + p_2^2} \begin{bmatrix} 2p_1 p_2 \\ 1 + p_2^2 - p_1^2 \\ 2p_1 \end{bmatrix} \quad (143)$$

and

$$X_1 = a \left((1 - \tilde{q}_2^2 \beta) \cos(F) + \tilde{q}_2 \tilde{q}_1 \beta \sin(F) - \tilde{q}_1 \right) \quad (144)$$

$$Y_1 = a \left((1 - \tilde{q}_1^2 \beta) \sin(F) + \tilde{q}_2 \tilde{q}_1 \beta \cos(F) - \tilde{q}_2 \right) \quad (145)$$

$$\dot{X}_1 = \frac{a^2 n}{r} (\tilde{q}_2 \tilde{q}_1 \beta \cos(F) - (1 - \tilde{q}_2^2 \beta) \sin(F)) \quad (146)$$

$$\dot{Y}_1 = \frac{a^2 n}{r} (-\tilde{q}_2 \tilde{q}_1 \beta \sin(F) + (1 - \tilde{q}_1^2 \beta) \cos(F)) \quad (147)$$

$$\beta = \frac{1}{1 + \sqrt{1 - \tilde{q}_1^2 - \tilde{q}_2^2}} \quad (148)$$

$$n = \sqrt{\frac{\mu}{a^3}} \quad (149)$$

where F is the eccentric longitude, and is found by solving the modified Kepler's equation:

$$F - \tilde{q}_1 \sin(F) + \tilde{q}_2 \cos(F) = \Lambda \quad (150)$$

The modified Kepler's equation can be solved with the following algorithm:

while $\Delta F > tol$

$$F_{new} = F - \frac{F - \tilde{q}_1 \sin(F) + \tilde{q}_2 \cos(F) - \Lambda}{1 - \tilde{q}_1 \cos(F) - \tilde{q}_2 \sin(F)}$$

$$\Delta F = F_{new} - F$$

$$F = F_{new}$$

where tol is a specified numerical tolerance. The numerical tolerance is necessary because Eq. (150) is a transcendental equation (as is the classical Kepler's equation), meaning that it cannot be solved explicitly. An initial guess of $F = \Lambda$ may be used. Once F has been found, it can also be used to find Ψ :

$$\Psi = \text{atan2}(\psi_1, \psi_2) \quad (151)$$

$$\psi_1 = ((1 + \eta)(\eta \sin(F) - \tilde{q}_2) + \tilde{q}_2(\tilde{q}_1 \cos(F) + \tilde{q}_2 \sin(F))) \quad (152)$$

$$\psi_2 = (1 + \eta)(\eta \cos(F) - \tilde{q}_1) + \tilde{q}_1(\tilde{q}_1 \cos(F) + \tilde{q}_2 \sin(F)) \quad (153)$$

3.5 Initial Conditions for Formation Initialization

In order to properly address the formation initialization problem for SmallSats, the initial state of the spacecraft should be chosen to simulate a realistic dispersal scenario. Figure 8, taken from the CSD data sheet [22], provides the ejection velocity as a function of spacecraft mass.

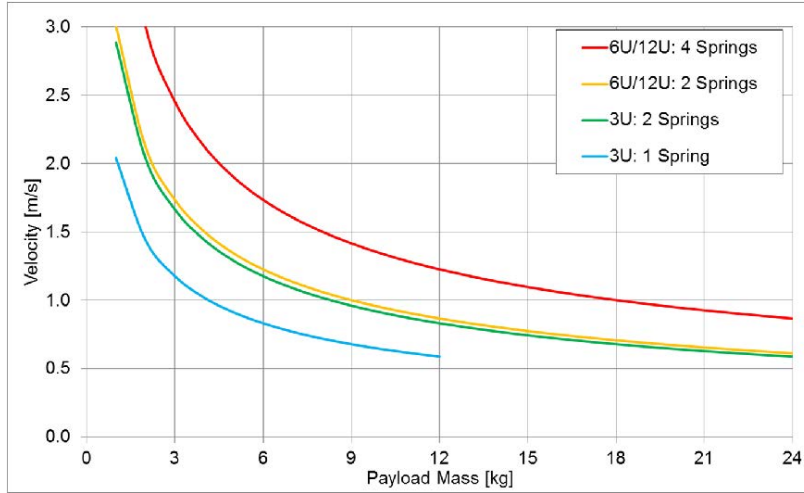


Figure 8: CSD Ejection Velocity

In order to be able to establish the desired formation, the deputy spacecraft must be able to cope with potentially unfavorable scenarios when it is deployed. A dispersal with velocity in the \hat{y} direction would result in a large drift rate due to the secular term (Eq. 5). Dispersals in the z -direction would result in cross-track oscillatory motion but no drift. Similarly, a dispersal in the x -direction would result in a 2:1 bounded relative motion ellipse going through the original dispersal point. Both of these latter cases have the advantage of keeping the deputy relatively close to the dispersal vehicle, but risk of collisions would be high if the formation was left uncontrolled. This seems to indicate that in cases where the dispersal vehicle and the chief satellite are the same, the ideal case would be aligning the dispersal mechanism (such as the CSD) mostly along the x - or z -direction, with a small component in the y -direction. This would have the advantage of keeping the drift rate small while ensuring that no collision would occur.

If the chief and the deputy are both being dispersed from a carrier vehicle (as opposed to a mothership chief satellite deploying its deputy satellites), the drift rate between the two can be mitigated by deploying the satellites at one orbit intervals. If both satellites are deployed along the y -axis at one-orbit intervals, the relative velocity between the satellites will be close to zero. This result is demonstrated in the following development. The HCW STM evaluated at $t = P$ (corresponding to one orbit period) is:

$$\Phi_{2\pi} = \begin{bmatrix} 1 & 0 & 0 & 0 & 0 & 0 \\ -6nP & 1 & 0 & 0 & -3P & 0 \\ 0 & 0 & 1 & 0 & 0 & 0 \\ 0 & 0 & 0 & 1 & 0 & 0 \\ 0 & 0 & 0 & 0 & 1 & 0 \\ 0 & 0 & 0 & 0 & 0 & 1 \end{bmatrix} \quad (154)$$

If this is used to propagate a dispersal along the y -axis, the result is:

$$\Phi_{2\pi} \bar{X}_0 = \begin{bmatrix} 1 & 0 & 0 & 0 & 0 & 0 \\ -6nP & 1 & 0 & 0 & -3P & 0 \\ 0 & 0 & 1 & 0 & 0 & 0 \\ 0 & 0 & 0 & 1 & 0 & 0 \\ 0 & 0 & 0 & 0 & 1 & 0 \\ 0 & 0 & 0 & 0 & 0 & 1 \end{bmatrix} \begin{bmatrix} 0 \\ 0 \\ 0 \\ 0 \\ v_{disp} \\ 0 \end{bmatrix} = \begin{bmatrix} 0 \\ -3Pv_{disp} \\ 0 \\ 0 \\ v_{disp} \\ 0 \end{bmatrix} \quad (155)$$

where v_{disp} is the dispersal velocity. If the satellites are of equal design they should have approximately the same dispersal velocity. If a second satellite, defined as the

chief, is deployed one orbit later, its initial Hill frame state is given by:

$$\bar{X}_{c0} = \begin{bmatrix} 0 \\ 0 \\ 0 \\ 0 \\ v_{disp} \\ 0 \end{bmatrix} \quad (156)$$

It is desirable to express the relative motion of the deputy with respect to the chief, rather than the dispersal vehicle. The Hill frame state of the deputy (in a new Hill frame centered on the chief) can be found by determining the ECI state vector of each spacecraft, and then using them to determine the state vector of the deputy in the new Hill frame. The ECI position and velocity of the chief and deputy spacecraft can be found using Eqs. (129) and (130).

$$\vec{r}_c = \vec{r}_v + T\vec{r}_{cHill} = \vec{r}_v \quad (157)$$

$$\vec{v}_c = T\vec{v}_{cHill} + T(\vec{\omega} \times \vec{r}_{cHill}) + \vec{v}_v = T\vec{v}_{cHill} + \vec{v}_v \quad (158)$$

$$\vec{r}_d = \vec{r}_v + T\vec{r}_{dHill} \quad (159)$$

$$\vec{v}_d = T\vec{v}_{dHill} + T(\vec{\omega} \times \vec{r}_{dHill}) + \vec{v}_v \quad (160)$$

where the subscript v refers to the dispersal vehicle. \vec{r} and \vec{v} vectors with a “Hill” subscript indicate the position and velocity components of the Hill frame state vector. The position and velocity differences can be found using Eqs. (121) and (122):

$$\delta\vec{r} = \vec{r}_d - \vec{r}_c = T\vec{r}_{dHill} \quad (161)$$

$$\delta\vec{v} = \vec{v}_{dECI} - \vec{v}_{cECI} = T(\vec{v}_{dHill} - \vec{v}_{cHill}) + T(\vec{\omega} \times \vec{r}_{dHill}) \quad (162)$$

However, $\vec{v}_{d_{Hill}} = \vec{v}_{c_{Hill}}$ in this case, therefore:

$$\delta\vec{v} = T (\vec{\omega} \times \vec{r}_{d_{Hill}}) \quad (163)$$

T is given by Eq. (126), and $\vec{r}_{d_{Hill}}$ is known from the deputy Hill frame state vector. If two-body motion is assumed, the angular velocity vector in the Hill frame is:

$$\vec{\omega} = \begin{bmatrix} 0 \\ 0 \\ n \end{bmatrix} \quad (164)$$

where n is the mean motion. Now, $\delta\vec{r}$ and $\delta\vec{v}$ can be expressed as:

$$\delta\vec{r} = \begin{bmatrix} \hat{r}_v & (\hat{H}_v \times \hat{r}_v) & \hat{H}_v \end{bmatrix} \begin{bmatrix} 0 \\ -3Pv_{disp} \\ 0 \end{bmatrix} = -3Pv_{disp} (\hat{H}_v \times \hat{r}_v) \quad (165)$$

$$\begin{aligned} \delta\vec{v} &= \begin{bmatrix} \hat{r}_v & (\hat{H}_v \times \hat{r}_v) & \hat{H}_v \end{bmatrix} \begin{bmatrix} 0 & -n & 0 \\ n & 0 & 0 \\ 0 & 0 & 0 \end{bmatrix} \begin{bmatrix} 0 \\ -3Pv_{disp} \\ 0 \end{bmatrix} \\ &= \begin{bmatrix} \hat{r}_v & (\hat{H}_v \times \hat{r}_v) & \hat{H}_v \end{bmatrix} \begin{bmatrix} 3Pnv_{disp} \\ 0 \\ 0 \end{bmatrix} = 3Pnv_{disp} \hat{r}_v \end{aligned} \quad (166)$$

Now that the position and velocity differences are known, Eqs. (117-119) and (123-125) can be used to find the Hill frame components. The transformation will give the state of the deputy in a Hill frame centered on the chief satellite (where previously it was centered on the dispersal vehicle). The development will start with

the x -component:

$$x = \frac{\delta \vec{r}^T \vec{r}_c}{r_c} = \frac{-3Pv_{disp} \left(\hat{H}_v \times \hat{r}_v \right)^T \vec{r}_c}{r_c} \quad (167)$$

However, $\vec{r}_c = \vec{r}_v$ because the transformation is made at the instant the chief is ejected from the dispersal vehicle. Eq. (167) can be rewritten as:

$$x = -3Pv_{disp} \left(\hat{H}_v \times \hat{r}_c \right)^T \hat{r}_c = 0 \quad (168)$$

Now, the y -component:

$$y = \frac{\delta \vec{r}^T \left(\vec{H}_c \times \vec{r}_c \right)}{\|\vec{H}_c \times \vec{r}_c\|} = \frac{-3Pv_{disp} \left(\hat{H}_v \times \hat{r}_c \right)^T \left(\vec{H}_c \times \vec{r}_c \right)}{\|\vec{H}_c \times \vec{r}_c\|} \quad (169)$$

The cross product magnitude of two arbitrary vectors is $\|\vec{a} \times \vec{b}\| = ab \sin \Theta$, where Θ is the angle between the two vectors. Since \vec{H}_c and \vec{r}_c are orthogonal, $\|\vec{H}_c \times \vec{r}_c\| = H_c r_c$. Therefore:

$$y = -3Pv_{disp} \left(\hat{H}_v \times \hat{r}_c \right)^T \left(\hat{H}_c \times \hat{r}_c \right) \quad (170)$$

The inner product of two vectors is $\vec{a}^T \vec{b} = ab \cos \Theta$. Assuming that the dispersal vehicle and the chief satellite lie in the same orbit plane (which should be the case for a y -axis dispersal), $\hat{H}_c = \hat{H}_v$. Therefore, $\left(\hat{H}_v \times \hat{r}_c \right)^T \left(\hat{H}_c \times \hat{r}_c \right) = 1$, because the angle between the unit vectors $\left(\hat{H}_v \times \hat{r}_c \right)$ and $\left(\hat{H}_c \times \hat{r}_c \right)$ is zero. This gives the expression for the y -component:

$$y = -3Pv_{disp} \quad (171)$$

The z component is:

$$z = \frac{\delta \vec{r}^T \vec{H}_c}{H_c} = -3Pv_{disp} \left(\hat{H}_v \times \hat{r}_c \right)^T \hat{H}_c = 0 \quad (172)$$

The \dot{x} component is given by:

$$\begin{aligned}
\dot{x} &= \frac{\delta \vec{v}^T \vec{r}_c + \delta \vec{r}^T \vec{v}_c}{r_c} - \frac{(\delta \vec{r}^T \vec{r}_c)(\vec{r}_c^T \vec{v}_c)}{r_c^3} \\
&= \frac{(3Pnv_{disp} \hat{r}_c)^T \vec{r}_c - 3Pv_{disp} (\hat{H}_v \times \hat{r}_c)^T \vec{v}_c}{r_c} - \frac{\left(-3Pv_{disp} (\hat{H}_v \times \hat{r}_c)^T \vec{r}_c\right) (\vec{r}_c^T \vec{v}_c)}{r_c^3} \\
&= \frac{(3Pnv_{disp} \hat{r}_c)^T \vec{r}_c - 3Pv_{disp} (\hat{H}_v \times \hat{r}_c)^T \vec{v}_c}{r_c} + \frac{\left(3Pv_{disp} (\hat{H}_v \times \hat{r}_c)^T \hat{r}_c\right) (\vec{r}_c^T \vec{v}_c)}{r_c^2}
\end{aligned} \tag{173}$$

The 2nd term goes to zero, because $(\hat{H}_v \times \hat{r}_c)^T \hat{r}_c = 0$.

$$\begin{aligned}
\dot{x} &= \frac{(3Pnv_{disp} \hat{r}_c)^T \vec{r}_c - 3Pv_{disp} (\hat{H}_v \times \hat{r}_c)^T \vec{v}_c}{r_c} \\
&= 3Pnv_{disp} \hat{r}_c^T \hat{r}_c - \frac{3Pv_{disp} (\hat{H}_v \times \hat{r}_c)^T \vec{v}_c}{r_c} \\
&= 3Pnv_{disp} - \frac{3Pv_{disp} (\vec{v}_c \times \hat{H}_v)^T \hat{r}_c}{r_c}
\end{aligned} \tag{174}$$

$\hat{H}_v = \hat{H}_c = \frac{\vec{r}_c \times \vec{v}_c}{\|\vec{r}_c \times \vec{v}_c\|}$, therefore:

$$\begin{aligned}
\dot{x} &= 3Pnv_{disp} - \frac{3Pv_{disp} \left(\vec{v}_c \times \frac{\vec{r}_c \times \vec{v}_c}{\|\vec{r}_c \times \vec{v}_c\|}\right)^T \hat{r}_c}{r_c} \\
&= 3Pnv_{disp} - \frac{3Pv_{disp} (\vec{v}_c \times \vec{r}_c \times \vec{v}_c)^T \hat{r}_c}{r_c \|\vec{r}_c \times \vec{v}_c\|} \\
&= 3Pnv_{disp} - \frac{3Pv_{disp} (\vec{r}_c (\vec{v}_c^T \vec{v}_c) - \vec{v}_c (\vec{v}_c^T \vec{r}_c))^T \hat{r}_c}{r_c \|\vec{r}_c \times \vec{v}_c\|}
\end{aligned} \tag{175}$$

If the chief orbit is circular, \vec{v}_c and \vec{r}_c are orthogonal, so $\vec{v}_c^T \vec{r}_c = 0$:

$$\begin{aligned}
\dot{x} &= 3Pnv_{disp} - \frac{3Pv_{disp} (\vec{r}_c (\vec{v}_c^T \vec{v}_c))^T \hat{r}_c}{r_c \|\vec{r}_c \times \vec{v}_c\|} \\
&= 3Pnv_{disp} - \frac{3Pv_{disp} v_c^2 \vec{r}_c^T \hat{r}_c}{r_c \|\vec{r}_c \times \vec{v}_c\|} \\
&= 3Pnv_{disp} - \frac{3Pv_{disp} v_c^2 \hat{r}_c^T \hat{r}_c}{\|\vec{r}_c \times \vec{v}_c\|} \\
&= 3Pnv_{disp} - \frac{3Pv_{disp} v_c^2}{\|\vec{r}_c \times \vec{v}_c\|} \tag{176}
\end{aligned}$$

Since \vec{r}_c and \vec{v}_c are orthogonal, $\|\vec{r}_c \times \vec{v}_c\| = r_c v_c$:

$$\begin{aligned}
\dot{x} &= 3Pnv_{disp} - \frac{3Pv_{disp} v_c}{r_c} \\
&= 3Pnv_{disp} - \frac{3Pv_{disp} \sqrt{\frac{\mu}{a}}}{a} \\
&= 3Pnv_{disp} - 3Pnv_{disp} = 0 \tag{177}
\end{aligned}$$

The \dot{y} component is given by:

$$\begin{aligned}
\dot{y} &= \frac{\delta \vec{v}^T (\vec{H}_c \times \vec{r}_c) + \delta \vec{r}^T (\dot{\vec{H}}_c \times \vec{r}_c + \vec{H}_c \times \vec{v}_c)}{\|\vec{H}_c \times \vec{r}_c\|} \\
&\quad - \frac{\delta \vec{r}^T (\vec{H}_c \times \vec{r}_c) (\vec{H}_c \times \vec{r}_c)^T (\dot{\vec{H}}_c \times \vec{r}_c + \vec{H}_c \times \vec{v}_c)}{\|\vec{H}_c \times \vec{r}_c\|^3} \\
&= 3Pnv_{disp} \hat{r}_c^T (\hat{H}_c \times \hat{r}_c) - \frac{3Pv_{disp} (\hat{H}_v \times \hat{r}_c)^T (\dot{\vec{H}}_c \times \vec{r}_c + \vec{H}_c \times \vec{v}_c)}{\|\vec{H}_c \times \vec{r}_c\|} \\
&\quad + \frac{3Pv_{disp} (\hat{H}_v \times \hat{r}_c)^T (\hat{H}_c \times \hat{r}_c) (\vec{H}_c \times \vec{r}_c)^T (\dot{\vec{H}}_c \times \vec{r}_c + \vec{H}_c \times \vec{v}_c)}{\|\vec{H}_c \times \vec{r}_c\|^2}
\end{aligned}$$

$$\begin{aligned}
&= -\frac{3Pv_{disp} \left(\hat{H}_v \times \hat{r}_c \right)^T \left(\dot{\vec{H}}_c \times \vec{r}_c + \vec{H}_c \times \vec{v}_c \right)}{\|\vec{H}_c \times \vec{r}_c\|} \\
&+ \frac{3Pv_{disp} (\vec{H}_c \times \vec{r}_c)^T \left(\dot{\vec{H}}_c \times \vec{r}_c + \vec{H}_c \times \vec{v}_c \right)}{\|\vec{H}_c \times \vec{r}_c\|^2} \\
&= -\frac{3Pv_{disp} \left(\hat{H}_c \times \hat{r}_c \right)^T \left(\dot{\vec{H}}_c \times \vec{r}_c + \vec{H}_c \times \vec{v}_c \right)}{\|\vec{H}_c \times \vec{r}_c\|} \\
&+ \frac{3Pv_{disp} (\hat{H}_c \times \hat{r}_c)^T \left(\dot{\vec{H}}_c \times \vec{r}_c + \vec{H}_c \times \vec{v}_c \right)}{\|\vec{H}_c \times \vec{r}_c\|} \\
&= 0
\end{aligned} \tag{178}$$

Finally, the \dot{z} component can be found by:

$$\begin{aligned}
\dot{z} &= \frac{\delta \vec{v}^T \vec{H}_c + \delta \vec{r}^T \dot{\vec{H}}_c}{H_c} - \frac{\delta \vec{r}^T \vec{H}_c (\vec{H}_c^T \dot{\vec{H}}_c)}{H_c^3} \\
&= \frac{3Pnv_{disp} \hat{r}_c^T \vec{H}_c - 3Pv_{disp} \left(\hat{H}_v \times \hat{r}_c \right)^T \dot{\vec{H}}_c}{H_c} + \frac{3Pv_{disp} \left(\hat{H}_v \times \hat{r}_c \right)^T \vec{H}_c (\vec{H}_c^T \dot{\vec{H}}_c)}{H_c^3} \\
&= 3Pnv_{disp} \hat{r}_c^T \hat{H}_c - \frac{3Pv_{disp} \left(\hat{H}_v \times \hat{r}_c \right)^T \dot{\vec{H}}_c}{H_c} + \frac{3Pv_{disp} \left(\hat{H}_v \times \hat{r}_c \right)^T \vec{H}_c (\vec{H}_c^T \dot{\vec{H}}_c)}{H_c^3}
\end{aligned} \tag{179}$$

\hat{r}_c and \hat{H}_c are orthogonal, so the first term goes to zero:

$$\begin{aligned}
\dot{z} &= -\frac{3Pv_{disp} \left(\hat{H}_v \times \hat{r}_c \right)^T \dot{\vec{H}}_c}{H_c} + \frac{3Pv_{disp} \left(\hat{H}_v \times \hat{r}_c \right)^T \vec{H}_c (\vec{H}_c^T \dot{\vec{H}}_c)}{H_c^3} \\
&= -\frac{3Pv_{disp} \left(\hat{H}_v \times \hat{r}_c \right)^T \dot{\vec{H}}_c}{H_c} + \frac{3Pv_{disp} \left(\hat{H}_c \times \hat{r}_c \right)^T \hat{H}_c (\vec{H}_c^T \dot{\vec{H}}_c)}{H_c^2}
\end{aligned} \tag{180}$$

$\left(\hat{H}_c \times \hat{r}_c \right)^T \hat{H}_c = 0$, so the 2nd term vanishes:

$$\dot{z} = -\frac{3Pv_{disp} \left(\hat{H}_v \times \hat{r}_c \right)^T \dot{\vec{H}}_c}{H_c}$$

$$\begin{aligned}
&= -\frac{3Pv_{disp} \left(\hat{H}_v \times \hat{r}_c \right)^T \left(\vec{r}_c \times \dot{\vec{v}}_c \right)}{H_c} \\
&= -\frac{3Pv_{disp} \left((\hat{H}_v^T \vec{r}_c)(\hat{r}_c^T \dot{\vec{v}}_c) - (\hat{H}_v^T \dot{\vec{v}}_c)(\hat{r}_c^T \vec{r}_c) \right)}{H_c}
\end{aligned} \tag{181}$$

$\hat{H}_v = \hat{H}_c$ and \vec{r}_c are orthogonal, therefore $\hat{H}_v^T \vec{r}_c = 0$:

$$\dot{z} = \frac{3Pv_{disp}(\hat{H}_v^T \dot{\vec{v}}_c)(\hat{r}_c^T \vec{r}_c)}{H_c} \tag{182}$$

$\dot{\vec{v}}_c = \ddot{\vec{r}}_c$, and it is known from the two-body problem that the acceleration is in the negative \vec{r}_c direction (Eq. (21)). In other words, \vec{H}_v and $\dot{\vec{v}}_c$ are orthogonal. Therefore:

$$\dot{z} = 0 \tag{183}$$

In summary, The Hill frame state of the deputy, with respect to a chief satellite deployed one orbit later, is:

$$\bar{X}_{d_{new}} = \begin{bmatrix} 0 \\ -3Pv_{disp} \\ 0 \\ 0 \\ 0 \\ 0 \end{bmatrix} \tag{184}$$

So, the state of the deputy will be a y -offset with zero relative velocity (the deputy will be in an ATO). There were a variety of assumptions that were employed in the preceding development. First, the initial state of the deputy was propagated forward one orbit using the HCW state transition matrix. This means that the result given in Eq. (184) may not hold true in situations that violate the HCW assumptions (described previously in the Background chapter). Two-body motion was assumed to determine the angular velocity, meaning that the effects of nodal regression were not

considered. It was also assumed that the dispersal vehicle and the chief satellite lie in the same orbit plane, but this assumption is reasonable as long as there is not a significant cross-track component in the dispersal velocity. Additionally, there will be small nonlinear effects that will cause the actual deputy state to deviate slightly from Eq. (184). Note that there is no particular reason why the first deployed satellite needs to be the deputy. If it was desirable for the second satellite to be the deputy, the sign of Eq. (184) could simply be reversed (since the decision of a chief satellite is arbitrary).

In order to quantify the effectiveness of the method, a simulation was run with a dispersal vehicle in a 500 km altitude circular, equatorial orbit. The dispersal velocity of the chief and deputy was assumed to be 1 m/s. The deputy initial state was transformed into the ECI frame and propagated forward in time by one orbit using the full nonlinear equations of motion (Eq. (186) without control). Then a coordinate transformation was performed to determine the deputy state in a new Hill frame centered on a chief satellite dispersed one orbit later. The result of the simulation for the deputy state vector in the new Hill frame was:

$$\bar{X}_{d_{new}} = \begin{bmatrix} -0.02 \text{ km} \\ -17.07 \text{ km} \\ 0 \text{ km} \\ -0.014 \text{ m/s} \\ -3.03 \times 10^{-4} \text{ m/s} \\ 0 \text{ m/s} \end{bmatrix} \quad (185)$$

The result predicted by Eq. (184) is $y = -17.03 \text{ km}$, with 0 for the other Hill frame components, so the differences between the predicted result and the simulation result are relatively small in this case.

The method developed in this section shows that in the case of a circular chief orbit and dispersals along the y -axis of the Hill frame, the relative velocity of the

satellites in a formation can be almost entirely eliminated by utilizing dispersals at one orbit intervals. This approach has the advantage of reducing the amount of ΔV required for initialization (since the satellites will not need to burn fuel to cancel relative drift), while ensuring that collisions between satellites in the formation will not occur.

3.6 Numerical Propagation of Solution

The trajectories are evaluated by propagating the orbits of the chief and deputy satellite using absolute equations of motion including J_2 perturbations and atmospheric drag:

$$\begin{aligned} \ddot{\vec{r}}_d = & -\frac{\mu}{r_d^3}\vec{r}_d - \frac{3}{2}J_2\frac{\mu}{r_d^2}\left(\frac{R_e}{r_d}\right)^2 \begin{bmatrix} (1 - 5(\frac{Z_d}{r_d})^2)\frac{X_d}{r_d} \\ (1 - 5(\frac{Z_d}{r_d})^2)\frac{Y_d}{r_d} \\ (3 - 5(\frac{Z_d}{r_d})^2)\frac{Z_d}{r_d} \end{bmatrix} \\ & - \frac{1}{2}\zeta_{\gamma_d}\frac{C_D S_d}{m_d}\sqrt{(\dot{X}_d - \omega_E Y_d)^2 + (\dot{Y}_d - \omega_E X_d)^2 + \dot{Z}_d^2} \begin{bmatrix} \dot{X}_d - \omega_E Y_d \\ \dot{Y}_d - \omega_E X_d \\ \dot{Z}_d \end{bmatrix} + \vec{u}_{ECI} \quad (186) \end{aligned}$$

$$\begin{aligned} \ddot{\vec{r}}_c = & -\frac{\mu}{r_c^3}\vec{r}_c - \frac{3}{2}J_2\frac{\mu}{r_c^2}\left(\frac{R_e}{r_c}\right)^2 \begin{bmatrix} (1 - 5(\frac{Z_c}{r_c})^2)\frac{X_c}{r_c} \\ (1 - 5(\frac{Z_c}{r_c})^2)\frac{Y_c}{r_c} \\ (3 - 5(\frac{Z_c}{r_c})^2)\frac{Z_c}{r_c} \end{bmatrix} \\ & - \frac{1}{2}\zeta_{\gamma_c}\frac{C_D S_c}{m_c}\sqrt{(\dot{X}_c - \omega_E Y_c)^2 + (\dot{Y}_c - \omega_E X_c)^2 + \dot{Z}_c^2} \begin{bmatrix} \dot{X}_c - \omega_E Y_c \\ \dot{Y}_c - \omega_E X_c \\ \dot{Z}_c \end{bmatrix} \quad (187) \end{aligned}$$

where \vec{u}_{ECI} is the control vector in the inertial frame. These equations of motion provide a computationally efficient and relatively accurate method for evaluating the effectiveness of the analytically determined thrust profiles. As can be seen from Eq.

(187), the chief satellite is uncontrolled. In the case of impulsive-thrust maneuvering, the \vec{u}_{ECI} term is dropped from Eq. (186), and copies of identical equations of motion are used for the chief and deputy. In this case, the deputy satellite state vector is updated after each coasting arc to include the ΔV (Eq. (41)).

In the continuous-thrust case, the control is not constrained to be constant. This means that the mass flow rate (\dot{m}) is also not constant. The equation for the specific impulse of a rocket engine with varying thrust is defined as [50]:

$$I_s = \frac{\int_0^t F(t)dt}{g_{ref} \int_0^t \dot{m}(t)dt} \quad (188)$$

where g_{ref} is the reference acceleration (9.8066 m/s²). This equation can be differentiated to yield:

$$\dot{m}(t) = \frac{F(t)}{I_s g_{ref}} \quad (189)$$

with thrust magnitude F defined as $F(t) = -m(t)U(t)$:

$$\dot{m}(t) = \frac{-m(t)U(t)}{I_s g_{ref}} \quad (190)$$

Equation (190) is a differential equation that can be numerically integrated to track the mass of the spacecraft throughout the maneuver.

In the case of impulsive thrust, the ΔV of a maneuver is solved for directly. However, the continuous-thrust case solves for the control acceleration. The continuous-thrust ΔV can be found by simply integrating the control acceleration magnitude $U(t)$ over the transfer time t_m . This integration can be performed analytically using the mathematical expression for $U(t)$ or numerically using the values of $\|\vec{u}(t)\|$ calculated throughout the maneuver.

$$\Delta V = \int_0^{t_m} U(t)dt \quad (191)$$

3.7 Algorithm Overview

The impulsive-thrust and continuous-thrust algorithms were both set up based on equinoctial elements. This was necessitated by a desire to build a general algorithm that can be used for formation flying in a variety of chief satellite orbits, including orbits that are circular and equatorial.

The first step is to define the orbit of the chief satellite. Once this is done, the initial state of the deputy can be defined. These initial states of the chief and deputy are then propagated for a specified initial coast period before any maneuvering begins. For the case of formation initialization, the deputy satellite is given an initial state in the Hill frame, simulating dispersal from a container such as the CSD (the state given by Eq. (184) was chosen for the formation initialization results shown in this thesis, but the algorithm does not require this choice). For formation reconfiguration, the initial conditions cannot be defined in such a straightforward manner, unless the desired orbit has simple initial conditions (such as an ATO). For the cases of PCO and GCO reconfiguration, the initial conditions are defined using a set of equations from Table 2 and Eq. (89). Once the initial conditions of the deputy satellite are obtained, the ECI state of the chief and deputy are propagated forward using identical copies of the equations of motion (Eqs. (186 - 187), with the \vec{u}_{ECI} term dropped).

Once the initial ECI states have been propagated for the specified coast period, the deputy spacecraft begins the maneuvering phase. For the impulsive-thrust case, the user defines a number of impulses (N) and a set of parameters to define the desired target orbit (such as ρ and α_I for a desired target PCO). The solver then iterates until it reaches a minimum-fuel solution that satisfies Eqs. (94) and (95). The solver then returns a length $N - 1$ vector of the coast durations, a $N \times 3$ matrix of $\Delta\vec{v}$ values (in the Hill frame), and a wait duration (Δt_w). The states of the chief and deputy are then propagated forward by Δt_w , and afterwards the first $\Delta\vec{v}$ is applied. The $\Delta\vec{v}$ is translated into the ECI frame and applied to the deputy ECI state vector. The ECI states of the chief and deputy are then propagated forward by the first coast duration,

and afterwards the second $\Delta\vec{v}$ is applied. This process is repeated until the end of the maneuver phase.

For the continuous-thrust case, the user must define a transfer time and a desired final state in the Hill frame. If the \vec{u} required to complete the maneuver in the specified time exceeds spacecraft performance parameters, the user is warned that the spacecraft cannot complete the maneuver in the specified time. The control vector \vec{u} is then rotated into the ECI frame and added to the equations of motion of the deputy (Eq. (186)), and the chief and deputy states are propagated forward by the transfer time.

Once the maneuvering phase is over, the states of the chief and deputy are propagated forward by a specified time. If there is no formation maintenance, the final ECI states of the chief and deputy are simply propagated using identical copies of equations of motion with no control. In the case of impulsive-thrust formation maintenance, the final states of the chief and deputy are propagated forward by the DLQR time step size. The reference trajectory is then sampled, and the feedback control law (Eq. (103)) is used to calculate the $\Delta\vec{v}$. This $\Delta\vec{v}$ is then rotated into the ECI frame and applied to the deputy state vector. The state of the chief and deputy are then propagated forward by the time step, and the process is repeated until the specified time for the final orbit propagation expires.

The continuous-thrust case for formation maintenance is virtually identical to the case of continuous-thrust maneuvering. A transfer time (t_{trans}) is specified, and the reference trajectory is sampled at $t = t_{current} + t_{trans}$. The states of the chief and deputy are then propagated forward by the transfer time using Eqs. (186-187). Following the maneuver, the actual state of the deputy is updated ($\bar{X}_{f_{actual}}$ and \bar{X}_f will not be identical, since linearized dynamics are used in the thrust profile calculation), and the process is repeated until the specified final orbit propagation time expires.

IV. Results

This chapter will present simulation results of the algorithms that have been outlined in the previous chapter.

4.1 *Formation Initialization*

This section will present results for cases involving formation initialization. The spacecraft coasts for a specified period simulating dispersal from a satellite dispenser such as the CSD. Then the spacecraft executes the formation initialization maneuver. The “+” marks the initial location of the deputy, and the “×” marks the location of the chief (defined as the origin). The chief satellite was placed in a 500 km altitude circular, equatorial orbit.

4.1.1 Impulsive-Thrust Initialization. For the impulsive-thrust formation initialization results, the initialization geometry is shown on the left, and the right hand side of the plots show the relative motion versus time. The circles mark the locations of the impulses. A dashed vertical line marks the end of the coast phase, and the dotted vertical lines mark the times of the impulses.

In Phase 1, the spacecraft executes an open-loop maneuver to the targeted final state. In Phase 2, the orbit of the spacecraft is propagated with the formation maintenance algorithm activated. This is to ensure that the spacecraft reaches the desired final orbit, since linearization errors in the targeting dynamics can cause the spacecraft to miss the desired final state at the end of the open-loop maneuver. The ΔV of Phase 1 and Phase 2 are summed to get the total initialization ΔV . This approach is then compared to an alternate method where feedback is introduced after each impulse.

Consider an impulsive-thrust formation initialization scenario involving a formation of two 6U CubeSats with a mass of 10 kg. Assuming a 2-springs configuration, the ejection velocity from the CSD is estimated to be 0.9 m/s (Fig. 8). The desired formation is a $\rho = 1$ km PCO. The initialization maneuver with a one-orbit dispersal

interval (the deputy is dispersed one orbit after the chief), $N = 2$ and $\Delta t_{max} = 3$ orbits is shown in Fig. 9. The ΔV for this maneuver was 1.94 m/s. It is clear from the figure that linearization errors play a significant role in formation initialization, as the > 14 km initial separation between chief and deputy is large enough to somewhat violate the $d \ll r$ assumption of linearized dynamics. However, the open-loop maneuver in Phase 1 gets the deputy sufficiently close for the closed-loop formation maintenance algorithm to achieve the desired relative trajectory.

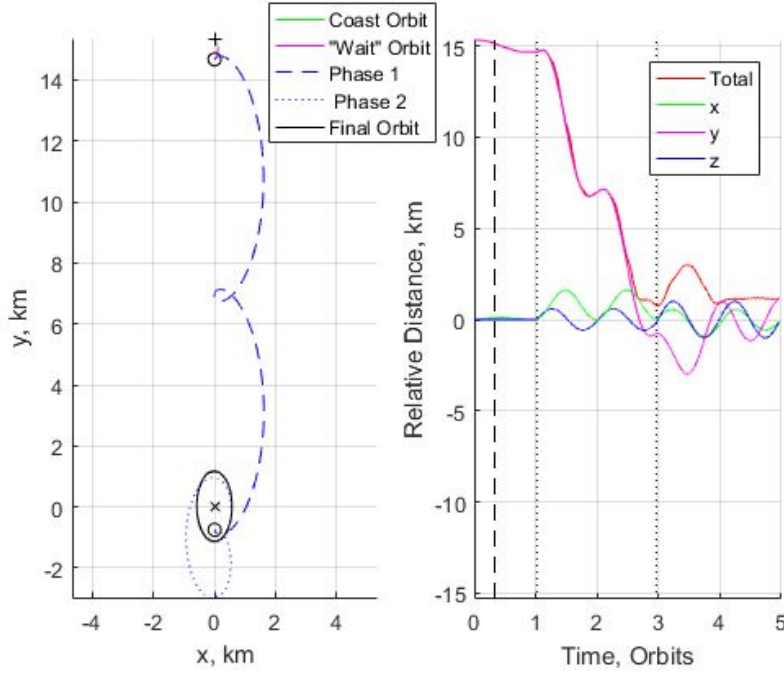


Figure 9: PCO Initialization Maneuver With $N = 2$, $\Delta t_{max} = 3$ Orbits

Now it is desirable to see how varying maneuver parameters such as N and Δt_{max} will affect the ΔV . Consider the same maneuver but with a more restrictive Δt_{max} , shown in Fig. 10. The ΔV for this case was 2.92 m/s. Clearly, the allowable transfer time has a significant effect on the ΔV for a formation initialization maneuver. For the case in Fig. 11, the Δt_{max} was restored to 3 orbits, and N was set to 3. In this case the ΔV was 1.79 m/s. This shows that a marginal improvement in ΔV can be made by increasing the number of burns. This is extrapolated even further in the 5-impulse, $\Delta t_{max} = 5$ orbits case shown in Fig 12, with a ΔV of 1.73 m/s. Even

though the extended time for the open-loop maneuver causes it to be less accurate than the previous cases, there is still an improvement in ΔV . This indicates that there is likely a breaking point where the open-loop dynamics is too inaccurate, and the total ΔV will increase due to the Phase 2 control having to correct the errors. This is demonstrated in Fig. 13, where the Δt_{max} was increased to 8 orbits, and the ΔV increased to 1.91 m/s. However, these errors can be corrected by introducing feedback control in the Phase 1 maneuver. This case is shown in Fig. 14, where the remaining impulses are re-computed after each burn. The ΔV was 1.31 m/s in this case. Clearly, feedback control is necessary for the fuel-optimal maneuver in most cases. Additionally, the Phase 2 curve in Fig 14 lies on top of the final orbit, indicating that corrections to the Phase 1 maneuver were not necessary. This result also indicates that higher- N maneuvers are likely to more accurately reach the desired final orbit the first time, as there is more opportunity for feedback control.

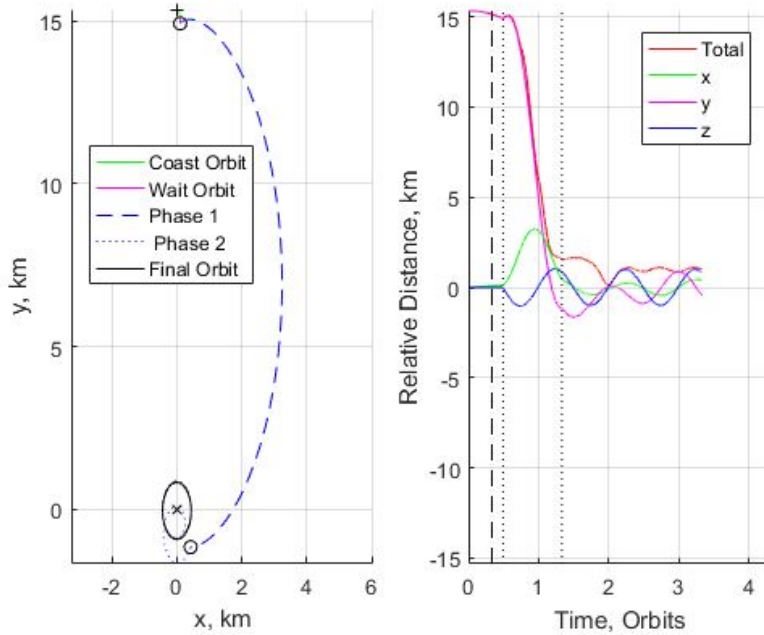


Figure 10: PCO Initialization Maneuver With $N = 2$, $\Delta t_{max} = 1$ Orbit

4.1.2 Low-Thrust Initialization. For the low-thrust initialization results, the left side of the figures show the initialization geometry, and the right side shows

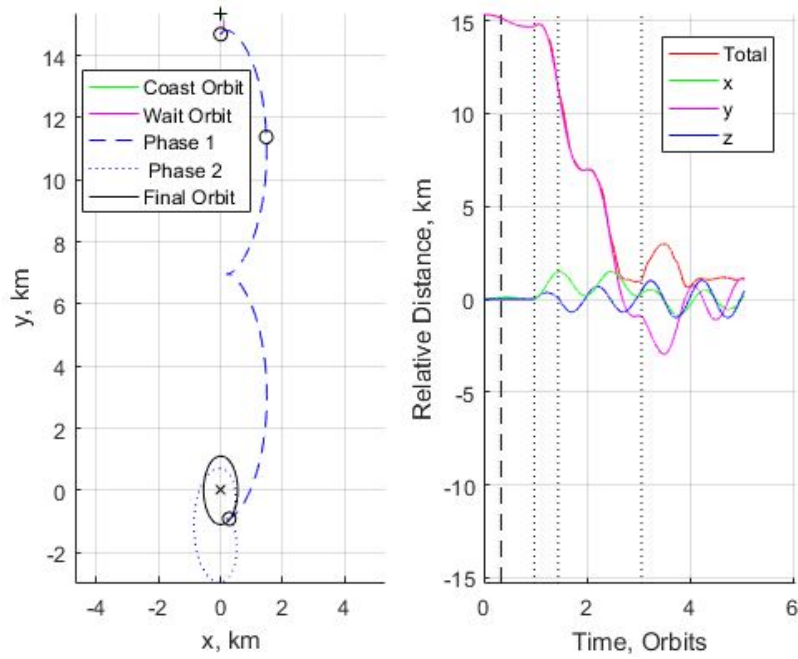


Figure 11: PCO Initialization Maneuver With $N = 3$, $\Delta t_{max} = 3$ Orbits

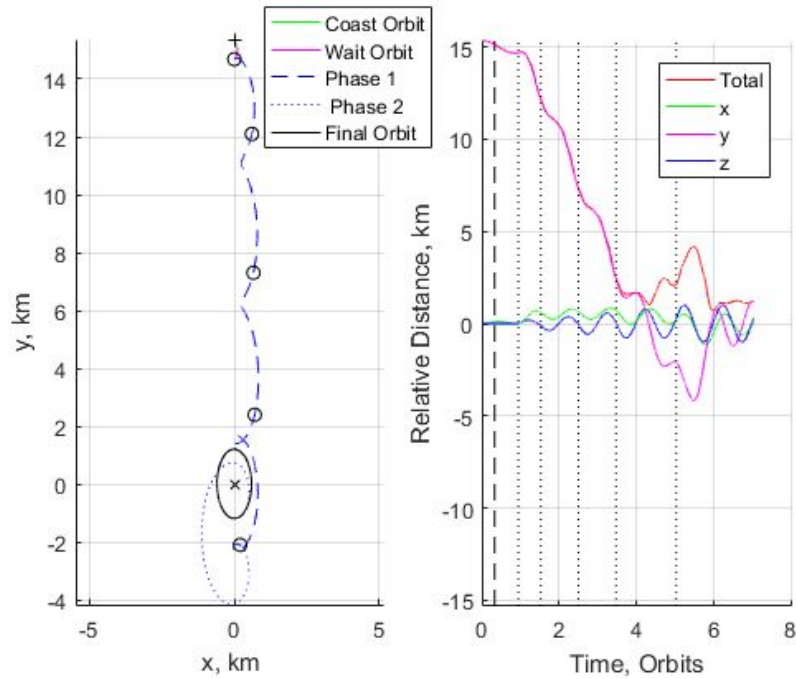


Figure 12: PCO Initialization Maneuver With $N = 5$, $\Delta t_{max} = 5$ Orbits

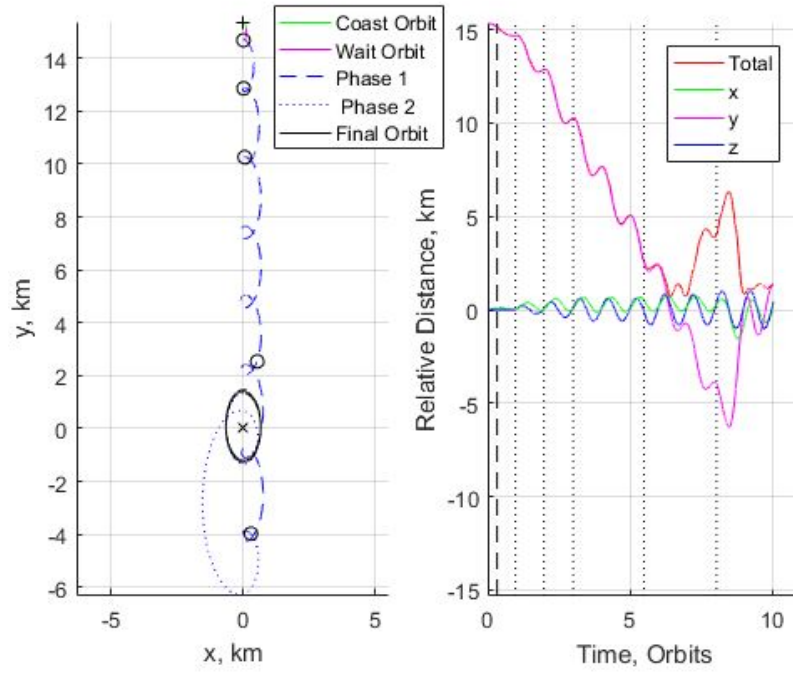


Figure 13: PCO Initialization Maneuver With $N = 5$, $\Delta t_{max} = 8$ Orbits

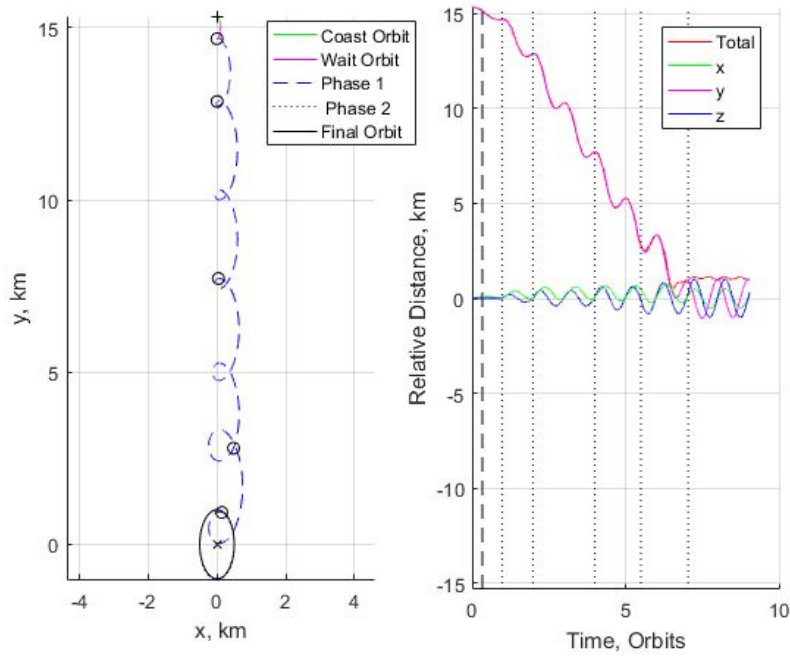


Figure 14: PCO Initialization Maneuver With $N = 5$, $\Delta t_{max} = 8$ Orbits, Closed-Loop Feedback

the control history for the maneuver. The horizontal bar indicates the control limit for the spacecraft. This line is typically located at the top of the graph.

The low-thrust initialization maneuvers were performed with the spacecraft parameters defined in Table 3. These parameters were chosen to be representative of a 6U CubeSat with an electrospray thruster. Like in the impulsive case, a one orbit dispersal interval was implemented. It was found that feedback control is necessary for most cases involving low-thrust formation initialization. For the results shown, the spacecraft was given a position update once every 1/2 orbit in order to re-evaluate the remainder of the trajectory. The spacecraft defined in Table 3 required 4.5 orbits to complete the 1 km PCO initialization maneuver (Fig. 15). The ΔV for this maneuver was 1.62 m/s, with a fuel cost of approximately 1.3×10^{-3} kg.

Table 3: Spacecraft Parameters

m	F	I_s
10 kg	1.0 mN	1300 s

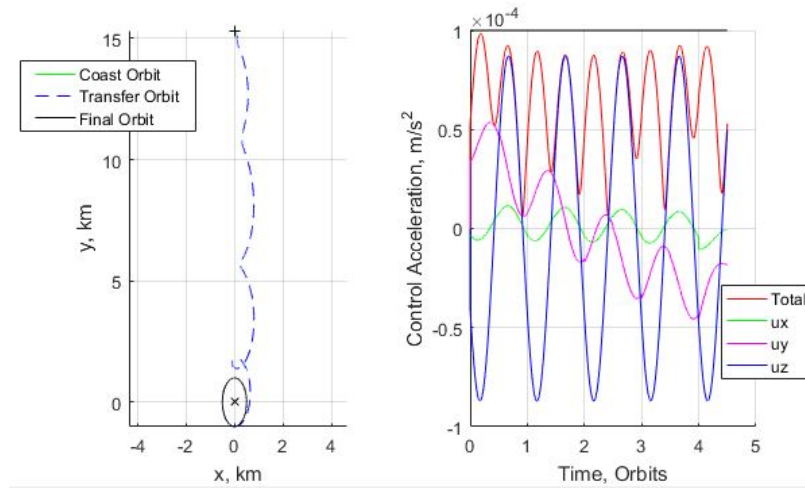


Figure 15: Low-Thrust PCO Initialization Maneuver, $\Delta t = 4.5$ Orbits

Like in the impulsive case, it is desirable to see what effect lengthening the transfer time has on the ΔV . The same PCO initialization maneuver with the transfer time extended to 8 orbits is shown in Fig. 16. The ΔV for this maneuver was

1.52 m/s with a fuel cost of approximately 1.2×10^{-3} kg. This result is a marginal improvement over the case shown in Fig. 15. The maneuver was executed once again with a transfer time of 20 orbits, resulting in a ΔV of 1.49 m/s. These results indicate that lengthening the transfer time does reduce the ΔV for low-thrust initialization, but only at an incremental rate.

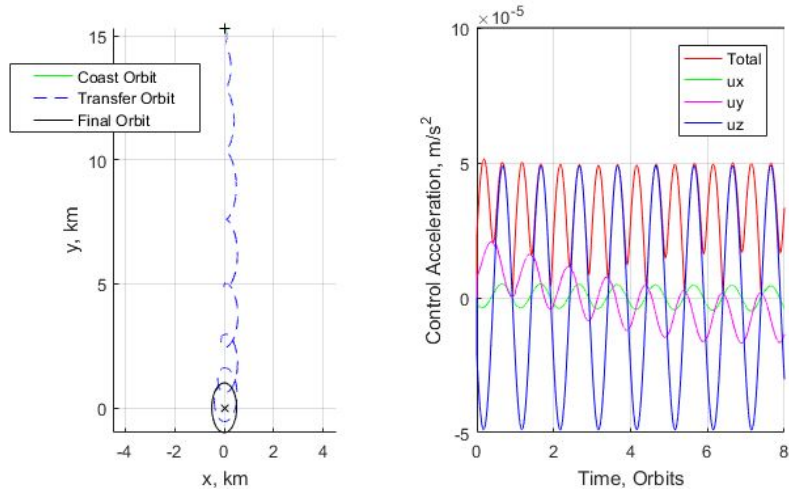


Figure 16: Low-Thrust PCO Initialization Maneuver, $\Delta t = 8$ Orbits

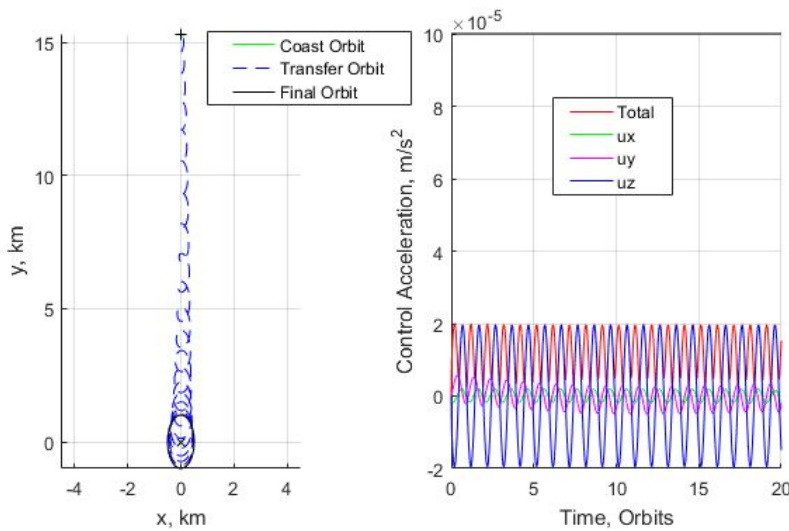


Figure 17: Low-Thrust PCO Initialization Maneuver, $\Delta t = 20$ Orbits

4.2 Formation Reconfiguration

This section will present results for cases involving formation reconfiguration. PCO, GCO, and ATO reconfiguration maneuvers are examined. The chief satellite was placed in a 500 km altitude circular, equatorial orbit.

4.2.1 Impulsive-Thrust Reconfiguration. The formation reconfiguration case for impulsive-thrust is broken into four phases. For the first phase, referred to as the “coast”, the initial conditions of the deputy satellite are propagated for one orbit to show the initial orbit geometry. Then, the maneuver phase begins. The maneuver phase is broken up into two parts – the “wait” period and the transfer. In the wait period, the spacecraft coasts for an additional period, determined by the optimizer (Eq. (93)). Then the spacecraft executes an open-loop N -impulse fuel-optimal maneuver. Following the maneuver, the final orbit is propagated for one orbit to show the final formation geometry.

Consider the case of a two-impulse GCO reconfiguration maneuver, shown in Fig. 18. The maximum allowable transfer time for this maneuver was set to 3 orbits, and the resulting ΔV was 1.11 m/s. Note that there is some fluctuation with the total relative distance at the end of the maneuver. Even though GCO orbits have constant chief-deputy spacing for all time in the HCW model, perturbations and nonlinearities cause the real trajectory to deviate somewhat from this property. The fluctuations also exist for the initial coast orbit, but they are harder to discern because they have a smaller magnitude. These fluctuations can be mitigated somewhat by a formation maintenance algorithm.

Even though the maximum transfer time for the result in Fig. 18 was set to 3 orbits, the fuel-optimal maneuver was completed in 1 orbit. This indicates that there may not be any benefit to long transfer times in the case of 2-impulse reconfiguration. Now, consider the same reconfiguration scenario, but with 3 impulses. This result is shown in Fig. 19. The transfer time is extended in this case, but the resulting ΔV is still 1.11 m/s. The same maneuver is again shown for 4 impulses and 5 impulses in

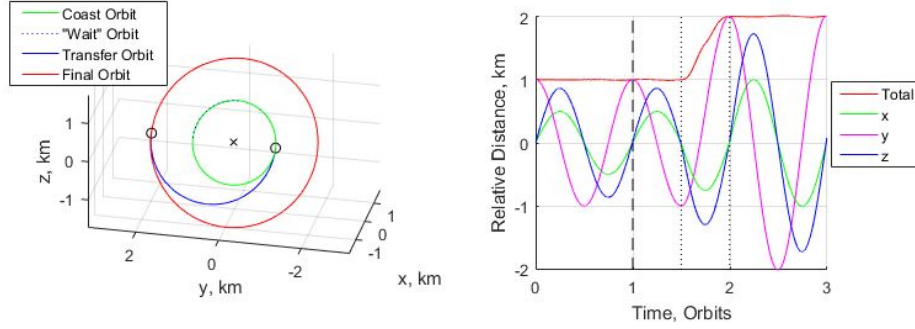


Figure 18: 1 km \rightarrow 2 km GCO Reconfiguration with $\Delta t_{max} = 3$ orbits, $N = 2$

Figs. 20 and 21, both with a ΔV of 1.11 m/s. The 5-impulse case was repeated, but with the maximum allowable transfer time increased to 5 orbits (Fig. 22). The ΔV for this maneuver was still 1.11 m/s. These results indicate that the GCO reconfiguration ΔV is approximately constant with the transfer time and number of impulses. A similar result was observed for PCOs, summarized in Table 4 (plots are shown in Figs. 43-47 in Appendix B).

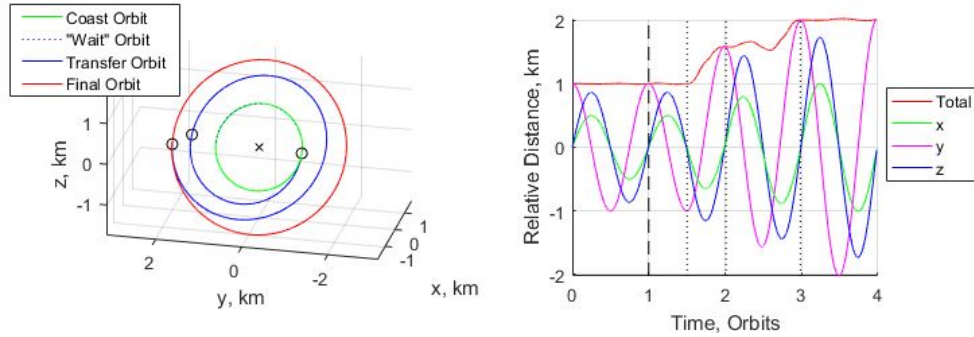


Figure 19: 1 km \rightarrow 2 km GCO Reconfiguration with $\Delta t_{max} = 3$ orbits, $N = 3$

Table 4: 1 km \rightarrow 2 km PCO Reconfiguration Maneuver Results

N	Δt_{max} (orbits)	ΔV m/s
2	3	1.24
3	3	1.24
4	3	1.24
5	3	1.25
5	5	1.24

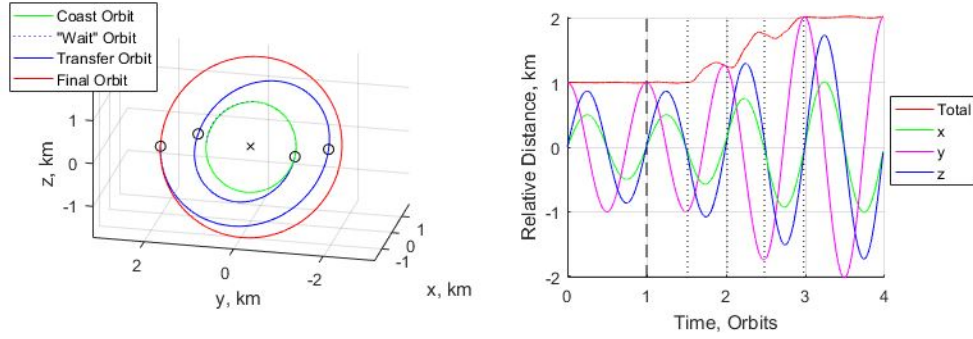


Figure 20: 1 km \rightarrow 2 km GCO Reconfiguration with $\Delta t_{max} = 3$ orbits, $N = 4$

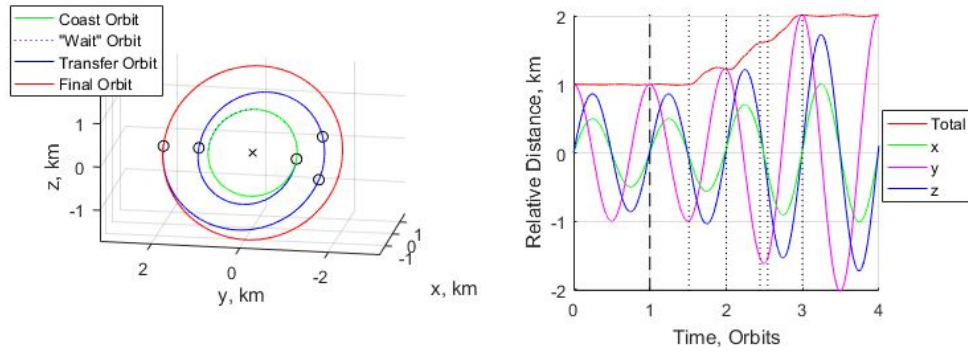


Figure 21: 1 km \rightarrow 2 km GCO Reconfiguration with $\Delta t_{max} = 3$ orbits, $N = 5$

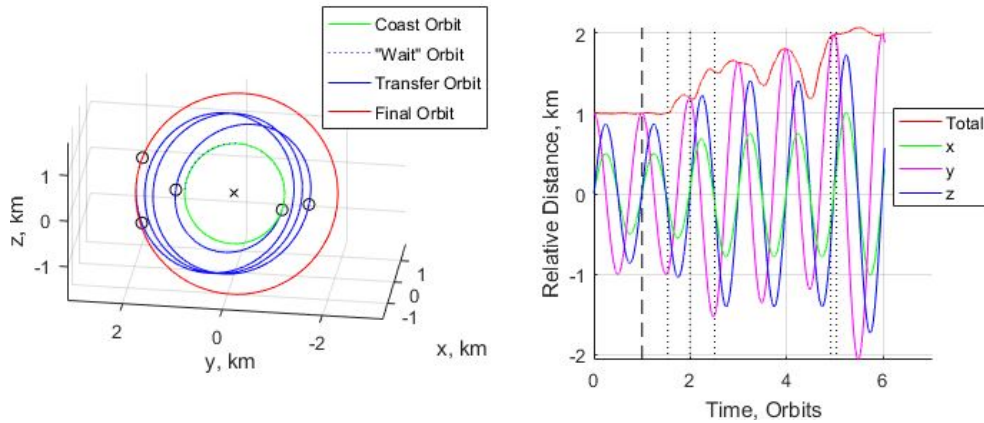


Figure 22: 1 km \rightarrow 2 km GCO Reconfiguration with $\Delta t_{max} = 5$ orbits, $N = 5$

Consider a $\rho = 2 \text{ km} \rightarrow 1 \text{ km}$ reconfiguration maneuver (Fig. 23), the reverse of the maneuver shown in Fig. 18. The ΔV for this maneuver was 1.11 m/s. Note that the ΔV for this case is equal to the 1.11 m/s ΔV for the 1 km \rightarrow 2 km case. The $\rho = 1 \text{ km} \rightarrow 3 \text{ km}$ case is shown in Fig. 24. The ΔV for this maneuver was

2.22 m/s. This is double the cost for the case shown in Fig. 18. These results indicated a potential approximate linear relationship between $|\Delta\rho|$ and ΔV for GCO reconfiguration maneuvers for a given semimajor axis (where $|\Delta\rho| = |\rho_f - \rho_0|$). This prompted an investigation to see if general trends could be drawn between $\Delta\rho$ and ΔV . Simulations were run for a variety of orbit regimes and inclinations to see if trends changed based on the reference orbit. The result is shown in Fig. 25. It was found that the fuel-optimal ΔV , normalized by the chief orbit circular velocity V_{circ} , is an approximate linear function of $\frac{\Delta\rho}{a_c}$ for all orbit regimes that were analyzed.

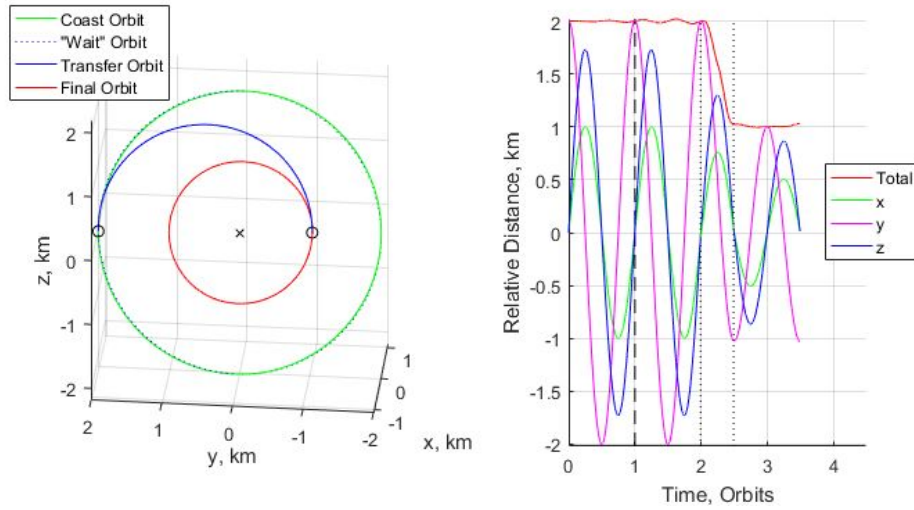


Figure 23: 2 km \rightarrow 1 km GCO Reconfiguration with $\Delta t_{max} = 3$ orbits, $N = 2$

The approximate linear trend is shown more explicitly in Fig. 26, where all of the simulation results are plotted as one data set. As can be seen from the figure, all of the simulation results lie on the linear curve. The slope of the linear curve implies a 1:1 relation between $\frac{\Delta V}{V_{circ}}$ and $\frac{\Delta\rho}{a_c}$. This suggests the approximate relationship for GCO reconfiguration:

$$\frac{\Delta V}{V_{circ}} \approx \frac{\Delta\rho}{a_c} \quad (192)$$

$$\Delta V \approx \frac{\Delta\rho}{a_c} V_{circ} \approx \frac{\sqrt{\mu}}{a_c^{3/2}} \Delta\rho \quad (193)$$

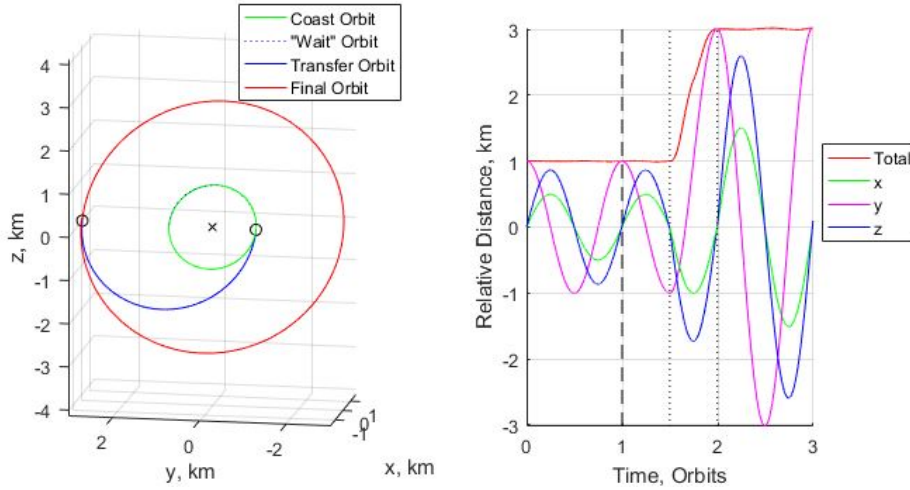


Figure 24: 1 km \rightarrow 3 km GCO Reconfiguration with $\Delta t_{max} = 3$ orbits, $N = 2$

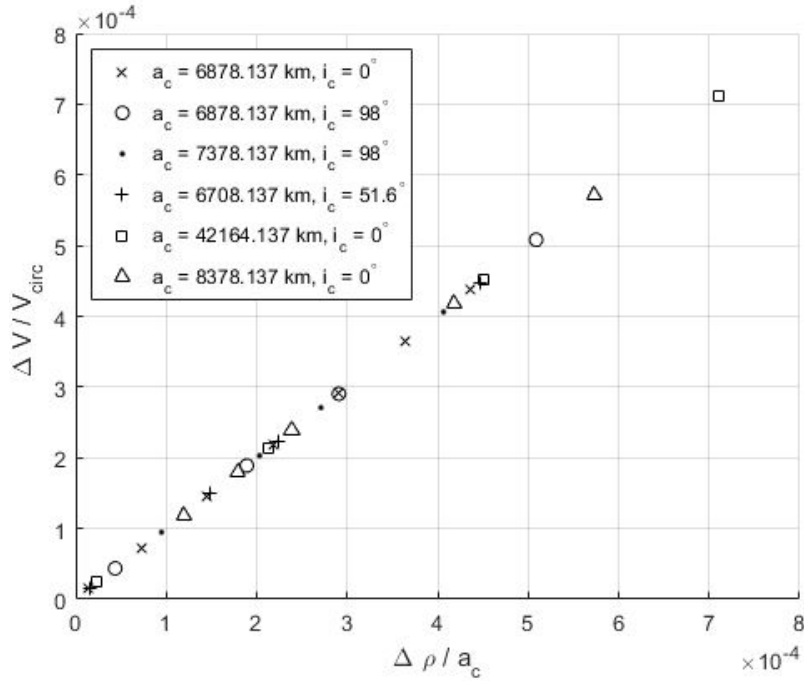


Figure 25: GCO Formation Reconfiguration Results Using Impulsive-Thrust

Now consider an ATO reconfiguration maneuver, where the spacecraft is maneuvering from a $y_d = 1$ km ATO to a $y_d = 2$ km ATO, shown in Fig. 27. The ΔV for the maneuver in Fig. 27 was 0.12 m/s. Note that for a similar change in relative distance, the ATO reconfiguration maneuver is inexpensive in comparison to the GCO (or PCO) reconfiguration maneuvers. This is likely due to the fact that

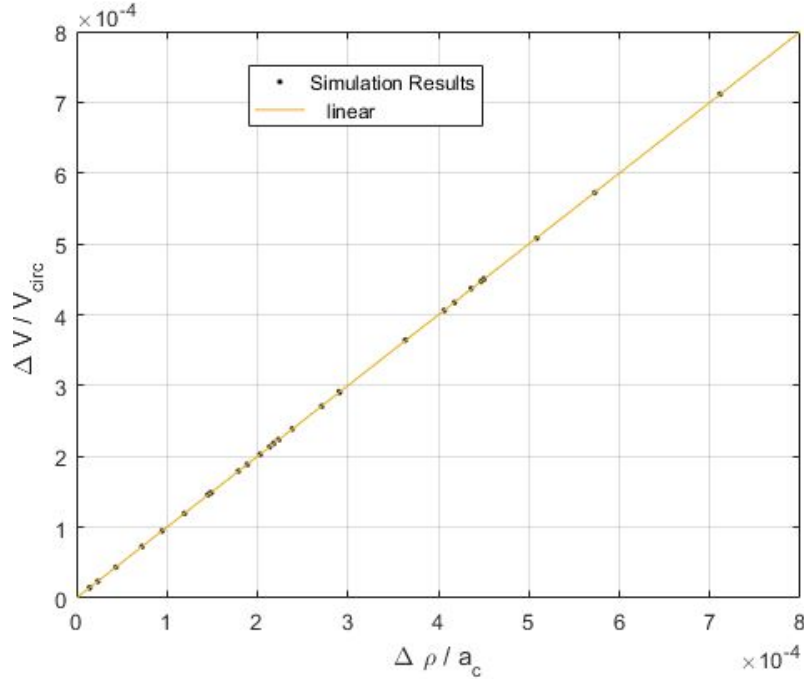


Figure 26: Approximate Linear Relationship For Impulsive GCO Reconfiguration

the ATO reconfiguration maneuver does not require any cross-track motion. Orbit plane change maneuvers, which are oriented along the same direction as the angular momentum vector (the Hill frame z -direction), are known to be costly from a ΔV standpoint. The same reconfiguration maneuver was then repeated, but with $N = 3$. The three-impulse ATO reconfiguration maneuver is shown in Fig. 28. The ΔV for the three-impulse case in Fig. 28 is 0.06 m/s. Note that unlike the case of PCO and GCO reconfiguration, there is a noticeable improvement in the ΔV when the number of impulses is increased. This could potentially be explained by the fact that in the ATO reconfiguration case, the center of relative motion is changing (an ATO can be viewed as a 2:1 relative motion ellipse centered at $\rho_y = y_d$ with $\rho_x = \rho_z = 0$). This means that unlike the case of PCO or GCO reconfiguration, the deputy satellite can use a smaller ΔV and drift to the new location. In some ways, the ATO reconfiguration maneuvers are more similar to the formation initialization results than the GCO or PCO reconfiguration maneuvers.

The 4-impulse and 5-impulse reconfiguration cases are shown in Figs. 29 and 30. The ΔV for the 4-impulse and 5-impulse maneuvers was 0.05 m/s and 0.07 m/s, respectively. However, when the Δt_{max} for the 5-impulse case was extended to 5 orbits (Fig. 31), the ΔV reduced to 0.04 m/s. This indicates that in the case of ATO reconfiguration, more impulses and a longer transfer time will generally result in a lower ΔV . However, there are certain cases where having a higher number of impulses is not necessarily more efficient.

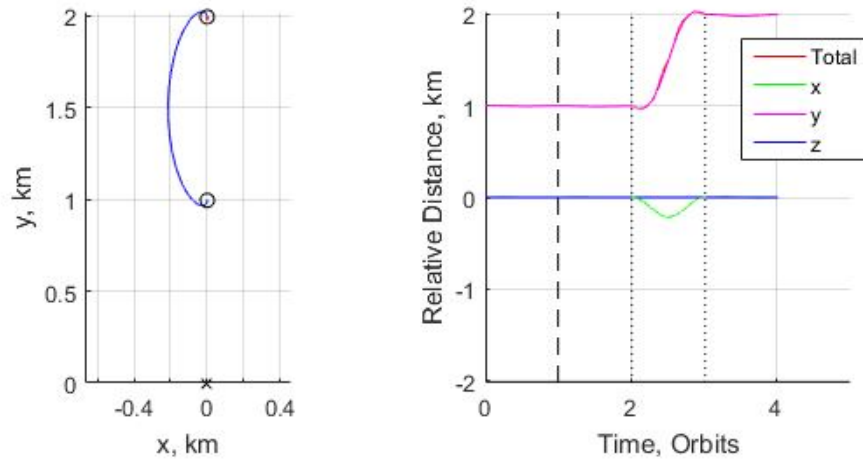


Figure 27: 1 km \rightarrow 2 km ATO Reconfiguration with $\Delta t_{max} = 3$ orbits, $N = 2$

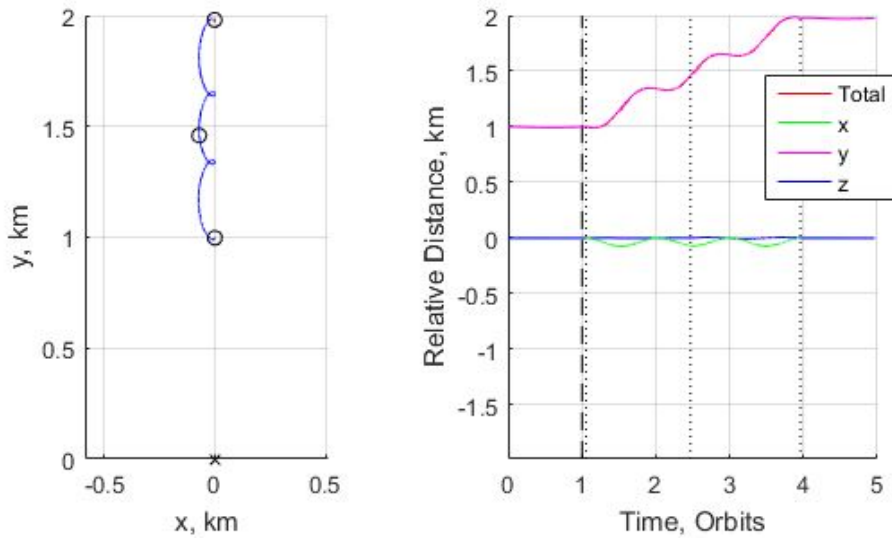


Figure 28: 1 km \rightarrow 2 km ATO Reconfiguration with $\Delta t_{max} = 3$ orbits, $N = 3$

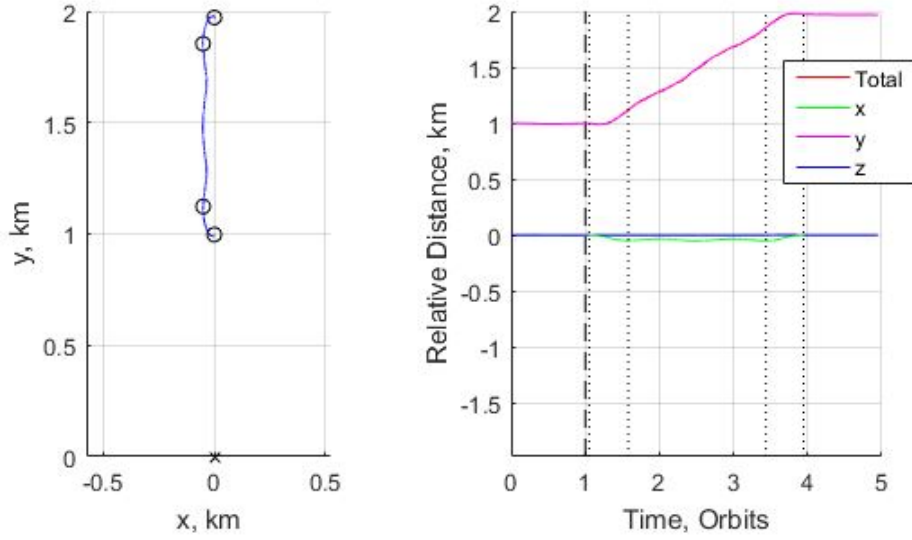


Figure 29: 1 km \rightarrow 2 km ATO Reconfiguration r with $\Delta t_{max} = 3$ orbits, $N = 4$

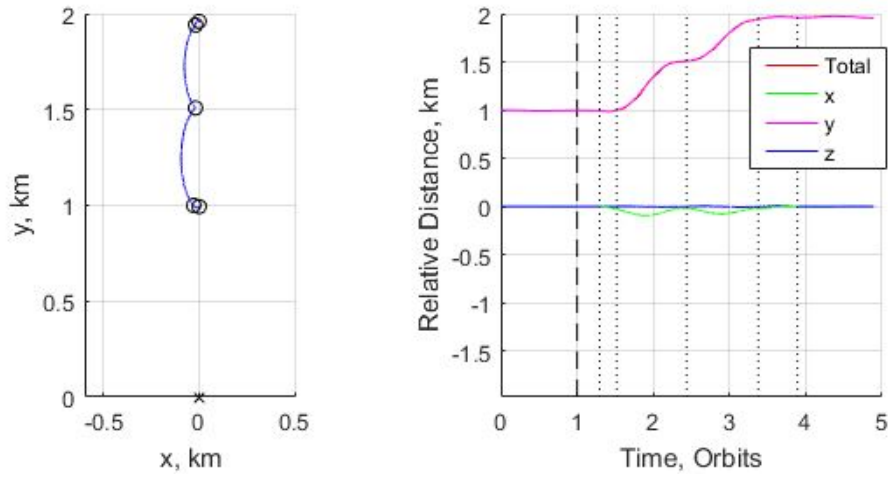


Figure 30: 1 km \rightarrow 2 km ATO Reconfiguration with $\Delta t_{max} = 3$ orbits, $N = 5$

4.2.2 Low-Thrust Reconfiguration. The 1 km \rightarrow 2 km GCO reconfiguration maneuver was executed for the spacecraft in Table 3, and is shown in Fig. 32. The maneuver was completed in four orbits and the ΔV was 1.31 m/s, corresponding to a fuel cost of 1.0×10^{-3} kg. As expected, the ΔV cost for low-thrust reconfiguration is somewhat higher than that of the impulsive-thrust case. The 1 km \rightarrow 3 km GCO reconfiguration maneuver using low-thrust is shown in Fig. 33. This maneuver was completed in 7 orbits and required 2.62 m/s of ΔV , corresponding to a fuel cost of

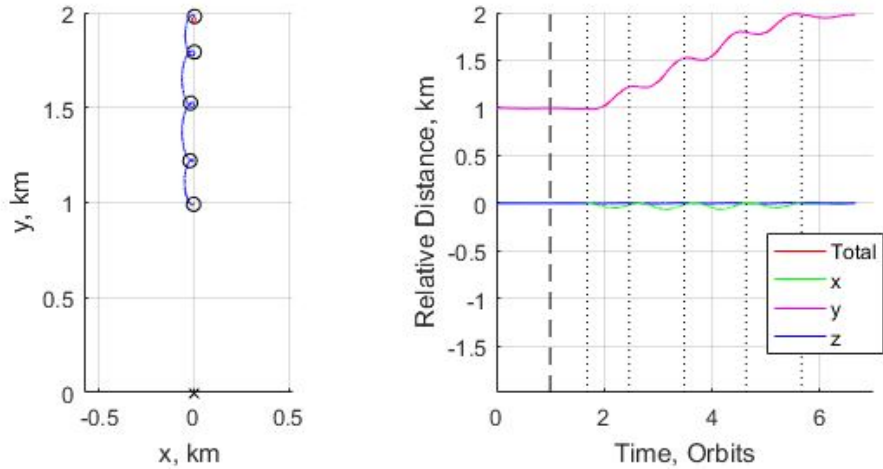


Figure 31: 1 km \rightarrow 2 km ATO Reconfiguration with $\Delta t_{max} = 5$ orbits, $N = 5$

2.1×10^{-3} kg. This indicates that as in the case of impulsive-thrust reconfiguration, there is an approximate linear relationship between the ΔV and $\Delta\rho$ of a maneuver for a given semimajor axis.

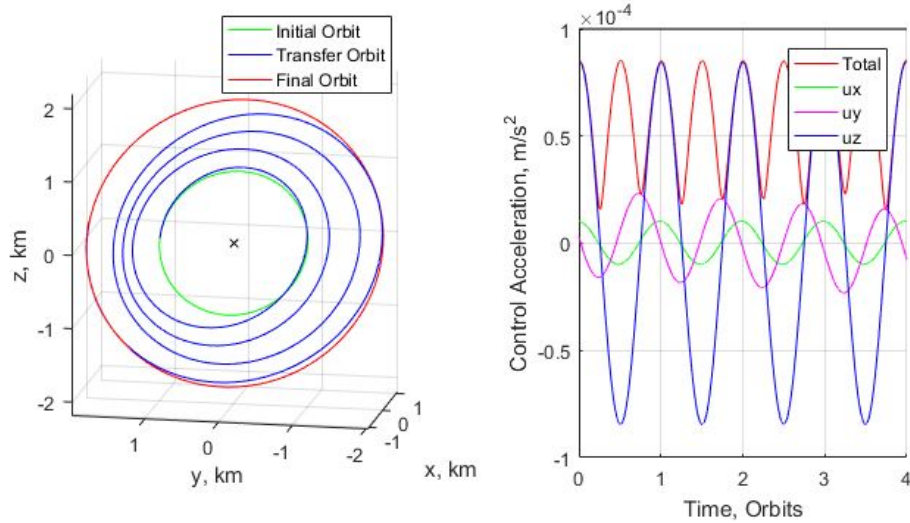


Figure 32: 1 km \rightarrow 2 km Low-thrust GCO Reconfiguration Maneuver

It is now desirable to vary the spacecraft parameters to see what effect they have on low-thrust reconfiguration scenarios. A large SmallSat (500 kg) with 23 mN of thrust and an I_{sp} of 2000 s would take 8 orbits to complete the 1 km \rightarrow 2 km GCO reconfiguration maneuver (Fig. 34), and would require 3.3×10^{-2} kg of propellant. The large SmallSat took approximately twice as long to complete the same maneuver

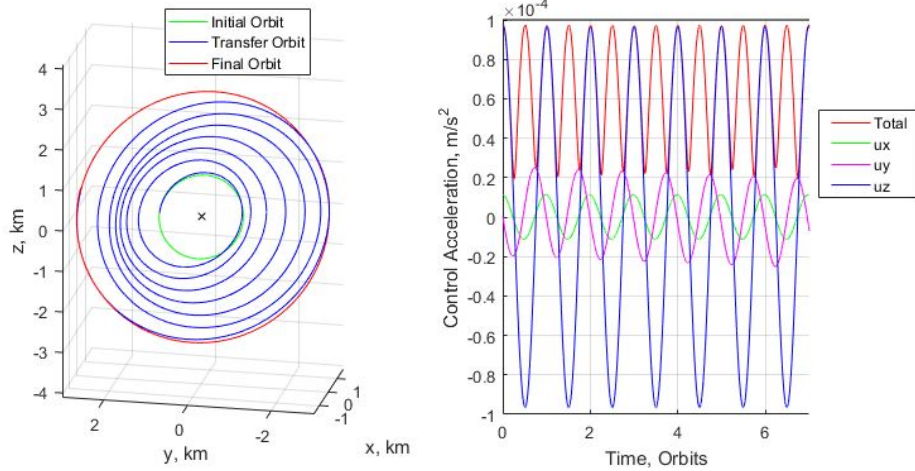


Figure 33: 1 km \rightarrow 3 km Low-Thrust GCO Reconfiguration Maneuver

as the 10 kg CubeSat. This indicates that a requirement for fast transfer times using low-power devices would drive the design to a smaller satellite, since the maximum achievable acceleration is limited by the upper bound on thrust for technologies such as ion thrusters.

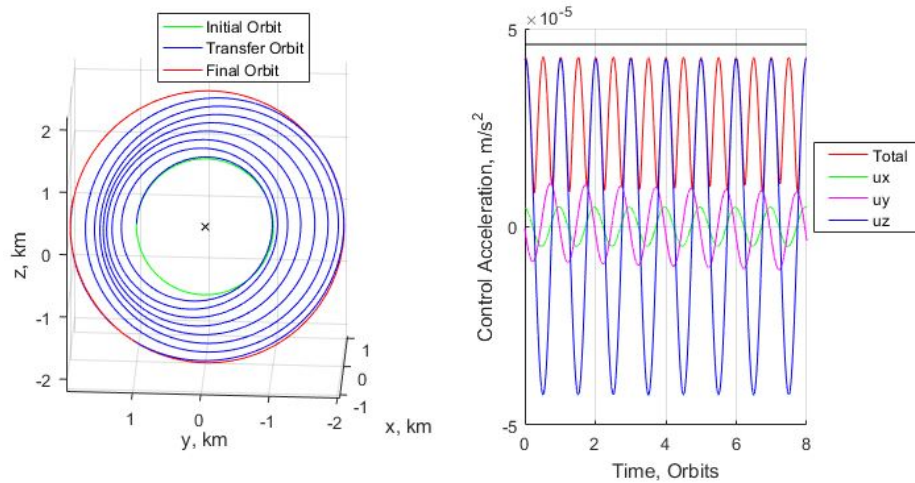


Figure 34: 1 km \rightarrow 2 km Low-Thrust GCO Reconfiguration Maneuver with 500 kg, 23 mN Thrust Satellite

On the other hand, faster reconfiguration maneuvers on the order of one or two orbits would necessitate high-power devices for all but the smallest of satellites. For example, the 10 kg CubeSat with 4 mN of thrust could complete the 1 km \rightarrow 2 km GCO reconfiguration maneuver in one orbit, and the 1 km \rightarrow 3 km GCO

reconfiguration maneuver in two orbits (Figs. 35-36). This level of performance for a CubeSat using low-thrust devices currently necessitates the use of a miniaturized Hall thruster [41]. However, it is likely that the power requirements for a Hall-effect thruster would be prohibitive for a spacecraft of this size. This indicates that a requirement for fast transfer times would require either a low-thrust spacecraft with a high power-to-mass ratio, or a design that utilizes chemical propulsion. Note that the reconfiguration maneuvers shown here are relatively large (1 to 2 km change in ρ for each maneuver). If the formations are smaller, the thrust requirements become less prohibitive. For example, the 10 kg CubeSat with 1 mN of thrust could complete a 0.5 km \rightarrow 1 km GCO reconfiguration in 2 orbits (Fig. 37).

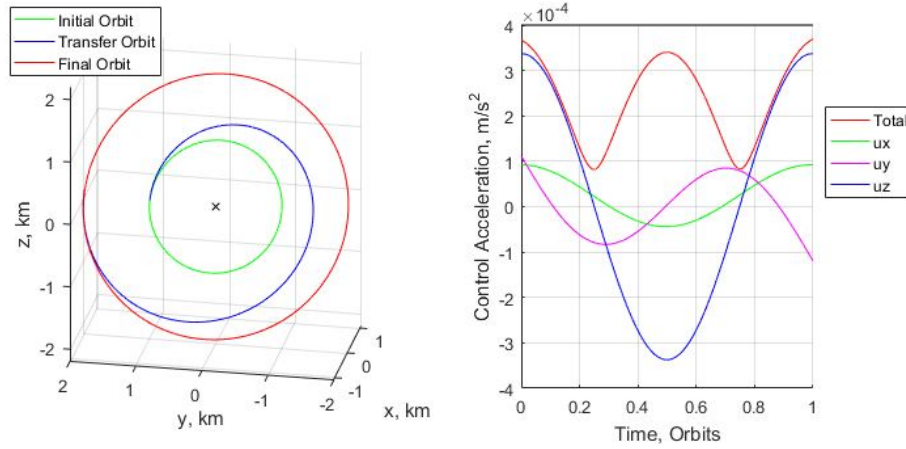


Figure 35: 1 km \rightarrow 2 km Low-Thrust GCO Reconfiguration Maneuver with 10 kg, 4 mN Thrust Satellite

While the analysis for low-thrust reconfiguration has so far been focused on general circular orbits, similar conclusions can be made for projected circular orbits as well. The results of PCO reconfiguration cases are summarized in Table 5 (plots are shown in Figs. 48-53 in Appendix B). Note how the transfer times and ΔV s are somewhat larger in the case of PCOs, due to the additional cross-track magnitude.

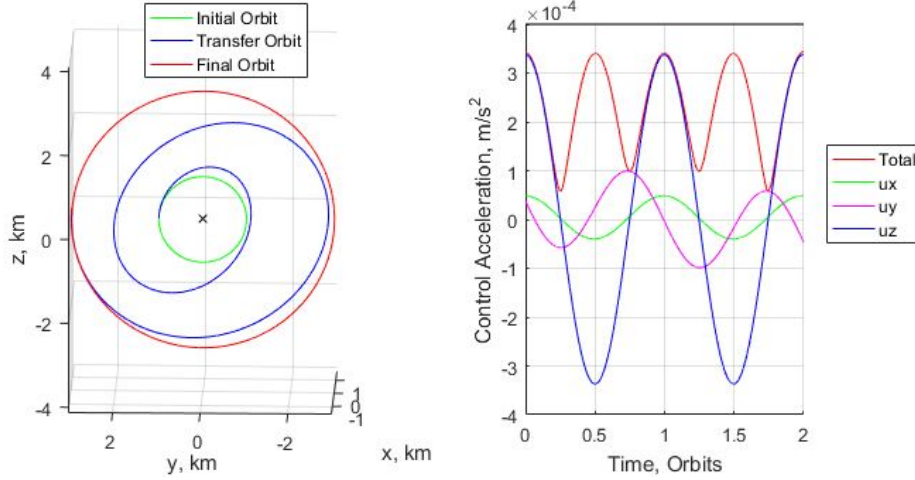


Figure 36: 1 km \rightarrow 3 km Low-Thrust GCO Reconfiguration Maneuver with 10 kg, 4 mN Thrust Satellite

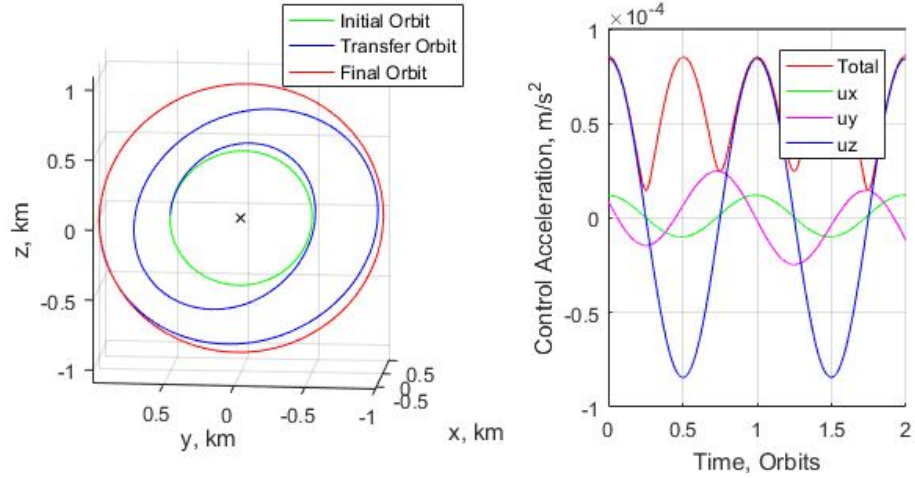


Figure 37: 0.5 km \rightarrow 1 km Low-Thrust GCO Reconfiguration Maneuver

Table 5: PCO Reconfiguration Using Low Thrust

m	F (mN)	I_{sp} (s)	$\Delta\rho$ (km)	Δt (orbits)	ΔV (m/s)	Δm (kg)
10	1	1300	1	4	1.49	1.2×10^{-3}
10	1	1300	2	8	2.98	2.3×10^{-3}
500	23	2000	1	9	1.49	3.8×10^{-2}
10	4	1300	1	1.2	1.49	1.2×10^{-3}
10	4	1300	2	2	2.99	2.3×10^{-3}
10	1	1300	0.5	2	0.75	5.8×10^{-4}

4.3 Drag Considerations

Up until the point, the presented results have assumed that the spacecraft are of identical design flying at the same attitude. This represents the optimal case where

the effects of differential drag are minimized. This section will present results for spacecraft flying at different attitudes (or of different designs) to examine the effects of differential drag on satellite formations.

Consider the case shown in Fig. 14, where a 1 km PCO initialization maneuver was executed resulting in a ΔV of 1.31 m/s. Now consider the same case, but this time the deputy spacecraft has a projected area of 600 cm² and the chief has a projected area of 200 cm². This represents a worst-case differential drag scenario for 6U CubeSats. A situation like this could arise if the chief spacecraft goes into emergency mode while the deputy is maneuvering, or if the chief has some task to perform that requires it to have a different attitude. The result using feedback control is shown in Fig. 38, with a ΔV of 1.56 m/s. This value is a 19% increase in ΔV from the ideal drag case. As can be seen from Fig. 38, the final PCO is also slightly off-center (the middle of the 2:1 ellipse is not quite on the \times). This can be corrected by increasing the number of impulses. The 6-impulse case is shown in Fig. 39, with a ΔV of 1.39 m/s. As can be seen in Fig. 39, the accuracy of the final orbit can be improved by increasing the number of impulses. Also, in this case, increasing the number of impulses reduced the ΔV .

The low-thrust formation initialization cases shown previously were repeated as worst-case differential drag scenarios, shown in Figs. 40-42. The ΔV s for the maneuvers in Figs. 40-42 were 1.62 m/s, 1.52 m/s, and 1.49 m/s, respectively. Interestingly, these ΔV values are the same as those for the ideal drag cases shown in Figs. 15-17. Clearly, differential drag does not have as significant of an effect on the low-thrust algorithm, as compared to the impulsive-thrust case. This may be due to the fact that the low-thrust initialization algorithm implements feedback on regular 1/2 orbit intervals, whereas the impulsive-thrust algorithm often has long coast periods between impulses. The long coast periods allow differential drag to build up a cumulative effect that must be compensated for with the remaining burns of the maneuver.

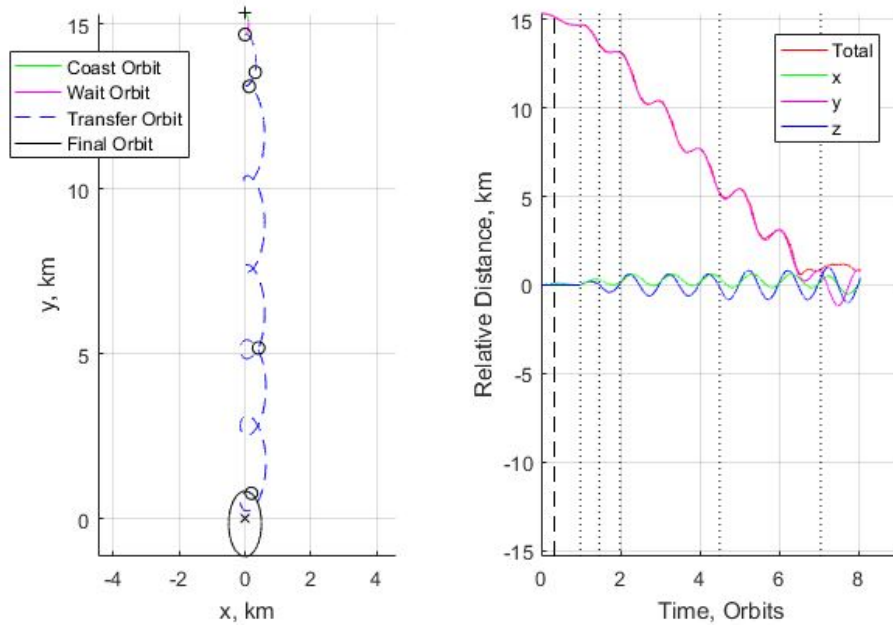


Figure 38: 1 km PCO Initialization Maneuver with Worst-Case Differential Drag

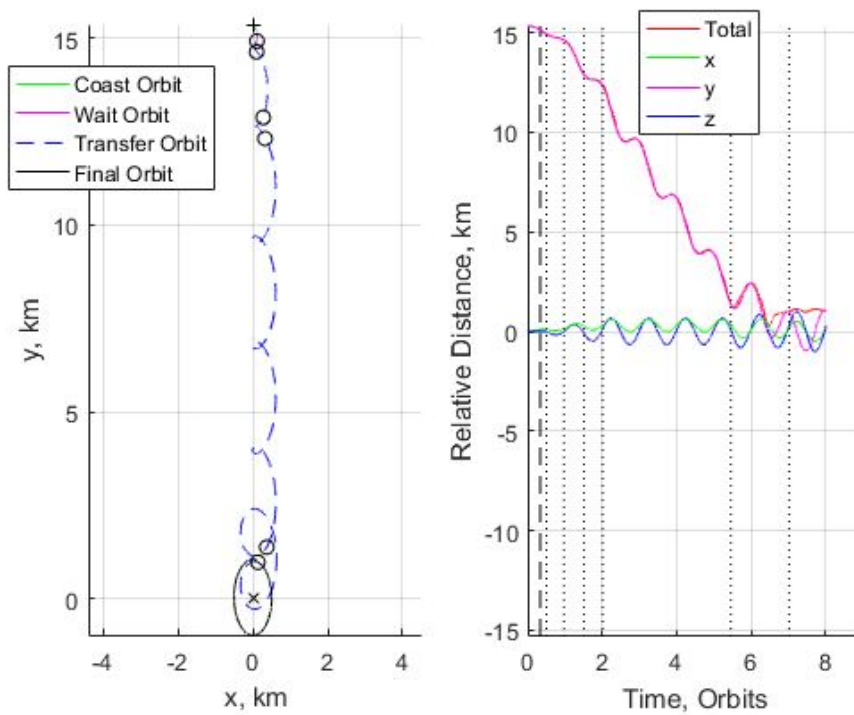


Figure 39: 1 km PCO Initialization Maneuver with Worst-Case Differential Drag, 6 Impulses

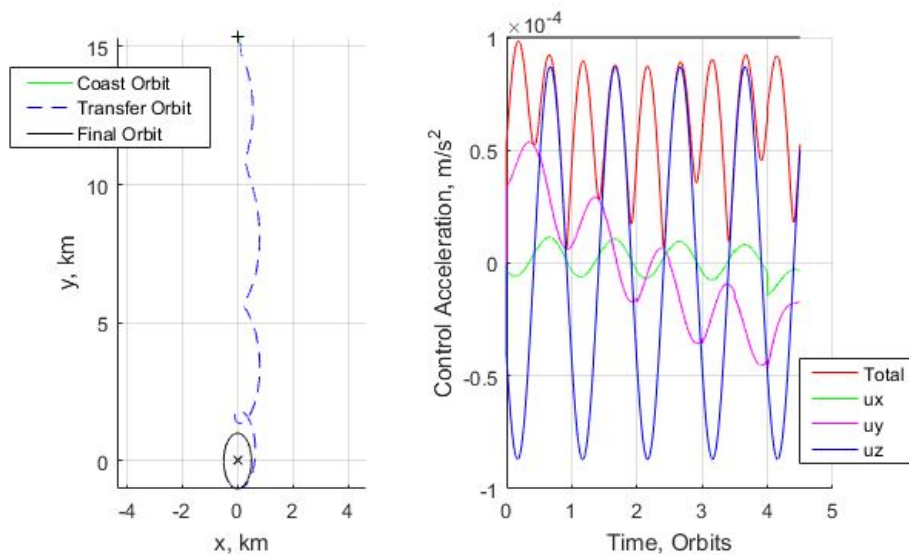


Figure 40: 1 km PCO Initialization Maneuver with Worst-Case Differential Drag using Low-Thrust, $\Delta t = 4.5$ orbits

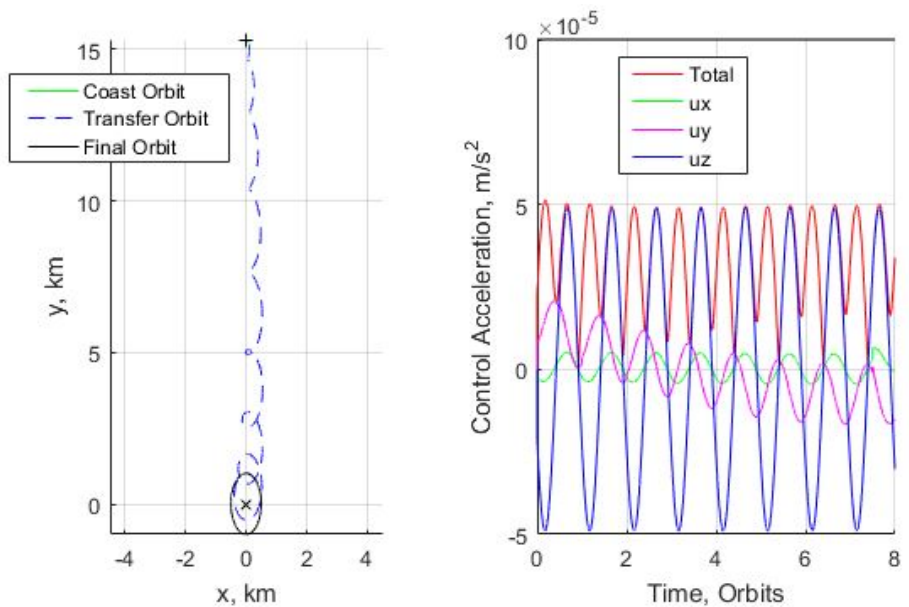


Figure 41: 1 km PCO Initialization Maneuver with Worst-Case Differential Drag using Low-Thrust, $\Delta t = 8$ orbits

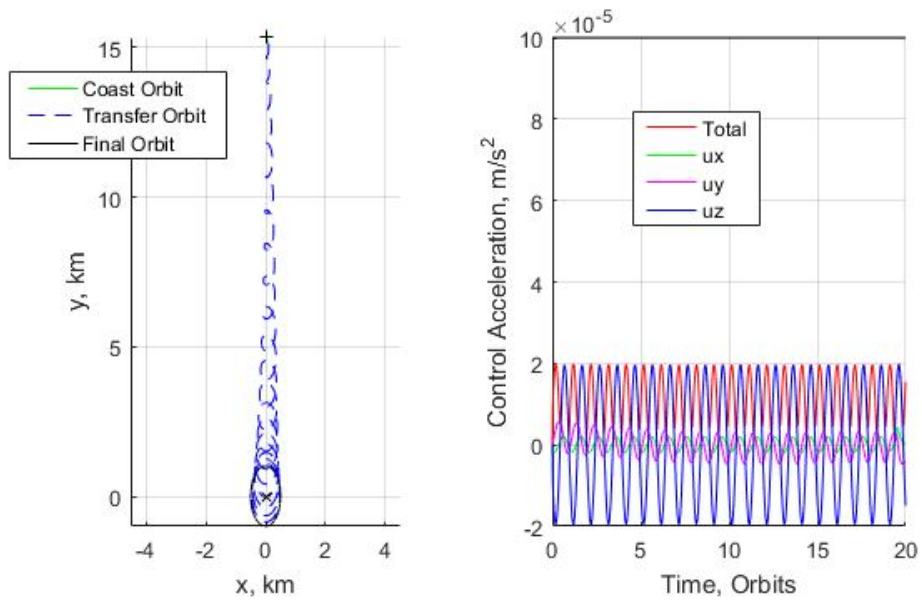


Figure 42: 1 km PCO Initialization Maneuver with Worst-Case Differential Drag using Low-Thrust, $\Delta t = 20$ orbits

V. Conclusion

This chapter will present the contributions of this thesis and the key findings of the simulation results in Chapter IV, following by a discussion of the limitations of the algorithms. Finally, recommendations will be made for future research projects.

5.1 Contributions and Key Findings

This thesis presented the derivation of the GCO initial conditions in terms of equinoctial elements, making it possible to implement GCO formations in equatorial orbits. Physical significance of the bounded relative motion parameters is presented for the case of general circular orbits. Impulsive-thrust and low-thrust algorithms were developed for formation initialization, reconfiguration, and maintenance. The algorithms¹ are valid in circular and equatorial orbit regimes where singularities are typically encountered. The trajectories are propagated with inertial equations of motion, so the full nonlinear dynamics and J_2 effects are captured, as well as aerodynamic perturbations. Maneuver costs determined by the impulsive-thrust and low-thrust algorithms were found to agree with similar analyses in the literature [4] [15], giving a high degree of confidence to their accuracy. Methods were presented to mitigate secular drift in the context of formation initialization. An approximate 1:1 relationship between $\frac{\Delta V}{V_{circ}}$ and $\frac{\Delta \rho}{a_c}$ was found for GCO reconfiguration using impulsive-thrust.

It was found that open-loop control is adequate for many scenarios involving formation reconfiguration. Results indicate that the formation reconfiguration cost for PCOs and GCOs is approximately constant with the transfer time and number of impulses. Low-thrust reconfiguration results show that requirements of fast transfer times on the order of one or two orbits would drive the design of small satellites with high power-to-mass ratios.

Formation initialization simulations demonstrate that longer transfer times and a higher number of impulses generally reduces ΔV , but not in every case. Unlike

¹Code is available upon request. Contact email is Robert.LaRue@afit.edu

the case of formation reconfiguration, it was found that feedback control is necessary for most cases involving formation initialization. An examination of worst-case drag effects found that a significant increase in the impulsive-thrust ΔV can occur when the spacecraft in a formation are flying at dissimilar attitudes for extended periods of time. Differential drag effects on the low-thrust algorithm were less pronounced, likely due to the regular interval of feedback in the low-thrust case.

5.2 *Limitations of the Algorithms*

One limitation of the developed algorithms is the use of the Schweighart-Sedwick state transition matrix for maneuver targeting. While this STM accounts for J_2 perturbations, it does not account for chief eccentricity. Therefore, the algorithms will not be able to effectively generate trajectories for elliptical chief orbits. Additionally, there are other relative motion models in the literature that are known to have higher fidelity [27]. This indicates that it is likely that more optimal maneuvers could be determined by using a higher-fidelity model. In the case of the impulsive thrust algorithm, a state transition matrix that accommodates chief eccentricity could be used, such as the Yamanaka-Ankerson [51] or Gim-Alfriend [14] models. For the low-thrust algorithms, any model used would need to accommodate the assumptions outlined in the Methodology. Cho and Park show explicitly in their article that a variety of relative motion models (including Yamanaka-Ankerson) satisfy their method [16].

Another notable limitation is the implementation of an exponential density model in the calculation of the drag perturbations. This model does not take into account factors such as solar weather and earth geomagnetic activity, both of which the atmospheric density is highly dependent on. While the implemented model provides a reasonable approximation of differential drag effects, the accuracy of the estimation could be significantly improved by implementing a higher-fidelity density model.

The algorithms account for J_2 and drag perturbations, but do not consider other perturbations such as solar radiation or third-body effects. This is sufficient for low-

Earth orbit, but these additional perturbations would need to be considered in order for the algorithms to be accurate in other orbit regimes, such as the geostationary belt. However, it is arguable that the spacecraft would have perturbations of a similar magnitude.

An additional caveat is that perfect position knowledge and perfect control was assumed for the work in this thesis. In reality a spacecraft's position cannot be known exactly, and thrusters have an associated error. These effects could be modeled by adding an appropriate amount of random noise to spacecraft position and control in the simulation.

5.3 Recommendations for Future Work

While this thesis took a step towards addressing the formation flying problem for small satellites, there are many areas that could be improved or expanded upon. As discussed in the previous section, the accuracy of the algorithms could be improved by using a higher-fidelity relative motion model for targeting, and atmospheric density estimation.

This thesis considered both impulsive and low-thrust methods, but only implemented a single approach for each. The chosen methods were based somewhat on the author's experience and are not necessarily the most effective methods for Small-Sat formation flying. There are a variety of formation control approaches that have been derived for formation flying, many of which have been cited in the Introduction. These could be adapted to similar problems as those addressed in this thesis. The transfer times for the low-thrust algorithm were iterated manually to find trajectories that satisfied the spacecraft constraints, but it would be possible to automate this process. The fidelity of the algorithms could be improved by accounting for finite burn times in the chemical propulsion case, rather than assuming impulsive burns. The algorithms in this thesis compute fuel-optimal maneuvers, but there are other cases (such as minimum time) that could be examined.

An analysis could be done to determine the “breaking point” of using relative motion models for formation initialization targeting (i.e., how far away can the deputy drift before linearization errors become so large that switching to a nonlinear targeting approach is necessary?). The ΔV results for ATO reconfiguration were very low, indicating that it is likely feasible to control and reconfigure these formations using propellantless control methods such as solar sails or drag panels. The formation initialization approach in this thesis assumed dispersal from the CSD, but there are a variety of other SmallSat dispensers that could be considered. Finally, the algorithms could be improved by accounting for attitude dynamics and position uncertainty.

Appendix A. State Transition Matrix

The Schweighart-Sedwick STM can be expressed as:

$$\Phi = \begin{bmatrix} \Phi_{11} & \Phi_{12} & \Phi_{13} & \Phi_{14} & \Phi_{15} & \Phi_{16} \\ \Phi_{21} & \Phi_{22} & \Phi_{23} & \Phi_{24} & \Phi_{25} & \Phi_{26} \\ \Phi_{31} & \Phi_{32} & \Phi_{33} & \Phi_{34} & \Phi_{35} & \Phi_{36} \\ \Phi_{41} & \Phi_{42} & \Phi_{43} & \Phi_{44} & \Phi_{45} & \Phi_{46} \\ \Phi_{51} & \Phi_{52} & \Phi_{53} & \Phi_{54} & \Phi_{55} & \Phi_{56} \\ \Phi_{61} & \Phi_{62} & \Phi_{63} & \Phi_{64} & \Phi_{65} & \Phi_{66} \end{bmatrix}$$

The nonzero entries of the matrix are:

$$\Phi_{11} = \frac{1}{1-s} (4(1+s) - (3-5s) \cos(\xi t))$$

$$\Phi_{14} = \frac{1}{n\sqrt{1-s}} \sin(\xi t)$$

$$\Phi_{15} = \frac{2\sqrt{1+s}}{n(1+s)} (1 - \cos(\xi t))$$

$$\Phi_{21} = \frac{2\sqrt{1+s}(3+5s)}{(1-s)\sqrt{1-s}} (\sin(\xi t) - \xi t)$$

$$\Phi_{22} = 1$$

$$\Phi_{24} = \frac{2\sqrt{1+s}}{n(1-s)} (\cos(\xi t) - 1)$$

$$\Phi_{25} = \frac{1}{1-s} \left(\frac{4(1+s)}{n\sqrt{1-s}} \sin(\xi t) - (3+5s)t \right)$$

$$\Phi_{33} = \cos(qt)$$

$$\Phi_{36} = \frac{1}{q} \sin(qt)$$

$$\Phi_{41} = \frac{n(3+5s)}{\sqrt{1-s}} \sin(\xi t)$$

$$\Phi_{44} = \cos(\xi t)$$

$$\begin{aligned}\Phi_{45} &= \frac{2\sqrt{1+s}}{\sqrt{1-s}} \sin(\xi t) \\ \Phi_{51} &= \frac{2n\sqrt{1+s}(3+5s)}{1-s} (\cos(\xi t) - 1) \\ \Phi_{54} &= -\frac{2\sqrt{1+s}}{\sqrt{1-s}} \sin(\xi t) \\ \Phi_{55} &= \frac{1}{1-s} (4(1+s) \cos(\xi t) - (3+5s)) \\ \Phi_{63} &= -q \sin(qt) \\ \Phi_{66} &= \cos(qt)\end{aligned}$$

The parameters are:

$$\begin{aligned}s &= \frac{3J_2 R_e^2}{8r_c^2} (1 + 3 \cos(2i_c)) \\ \xi &= n\sqrt{1-s} \\ c &= \sqrt{1+s} \\ n &= \sqrt{\frac{\mu}{r_c^3}} \\ \delta h_0 &= h_d - h_c \\ \gamma_0 &= \operatorname{acot} \left(\frac{\cot(i_c) \sin(i_d) - \cos(i_d) \cos(\delta h_0)}{\sin(\delta h_0)} \right) \\ \dot{h}_d &= -\frac{3}{2} \frac{J_2 n R_e^2}{r_c^2} \cos(i_d) \\ \dot{h}_c &= -\frac{3}{2} \frac{J_2 n R_e^2}{r_c^2} \cos(i_c)\end{aligned}$$

$$q = nc - (\cos(\gamma_0) \sin(\gamma_0) \cos(\delta h) - \sin(\gamma_0)^2 \cos(i_d))(\dot{h}_d - \dot{h}_c) - \dot{h}_d \cos i_d$$

if $i_d \approx i_c$

$$q = nc + \frac{3J_2 n R_e^2}{2r_c^2} \cos(i_c)^2$$

Appendix B. Additional Results

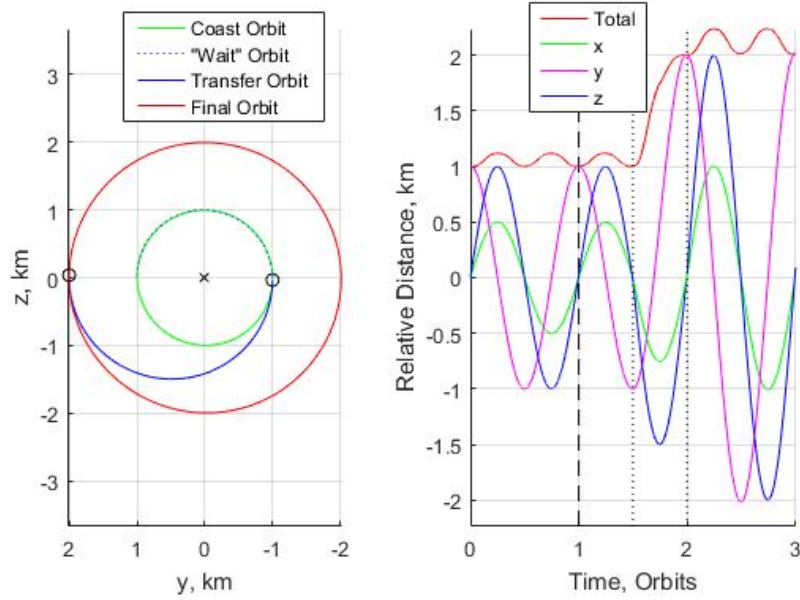


Figure 43: 1 km \rightarrow 2 km PCO Reconfiguration with $\Delta t_{max} = 3$ orbits, $N = 2$

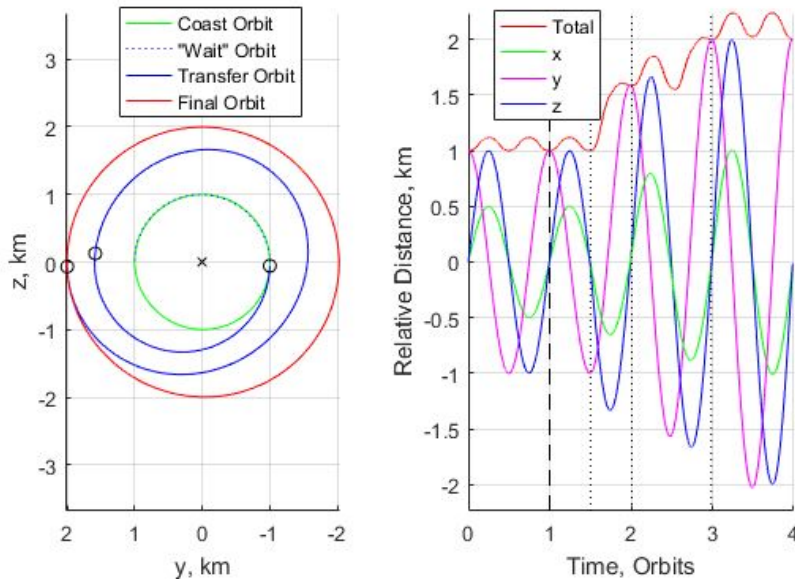


Figure 44: 1 km \rightarrow 2 km PCO Reconfiguration with $\Delta t_{max} = 3$ orbits, $N = 3$

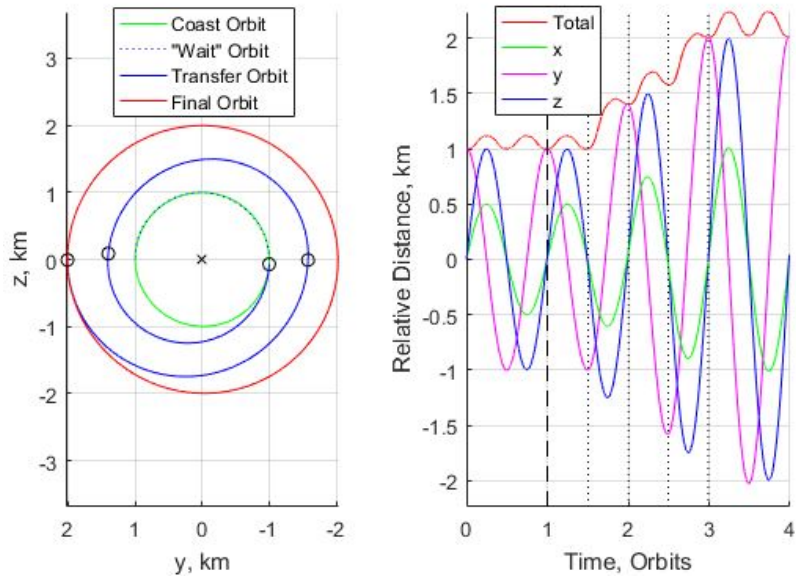


Figure 45: 1 km \rightarrow 2 km PCO Reconfiguration with $\Delta t_{max} = 3$ orbits, $N = 4$

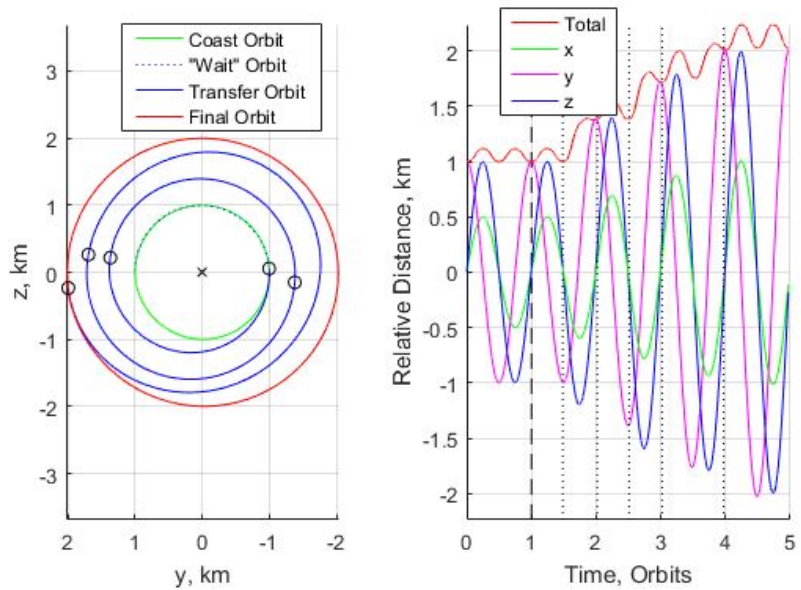


Figure 46: 1 km \rightarrow 2 km PCO Reconfiguration with $\Delta t_{max} = 3$ orbits, $N = 5$

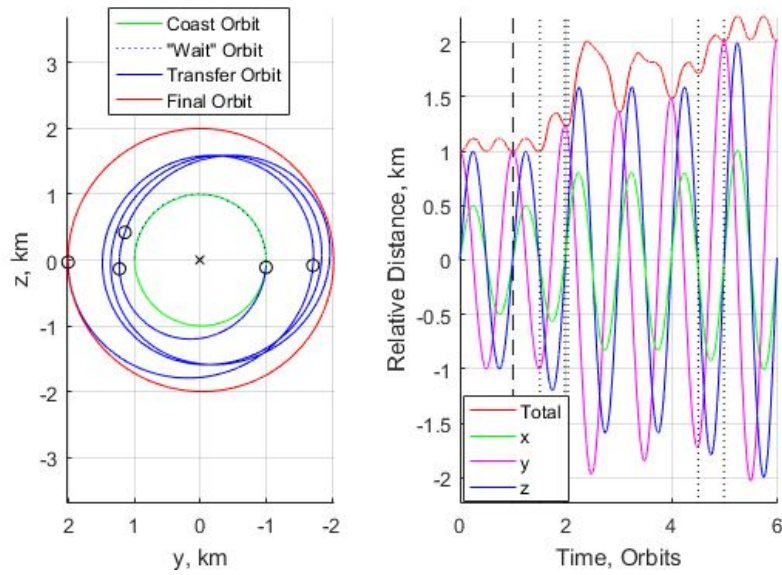


Figure 47: 1 km \rightarrow 2 km PCO Reconfiguration with $\Delta t_{max} = 5$ orbits, $N = 5$

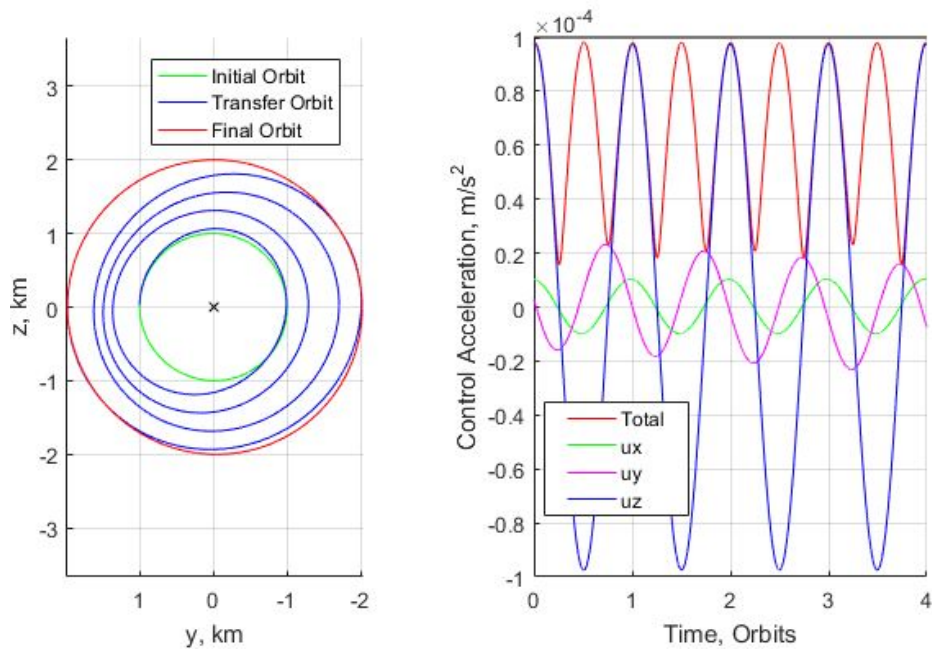


Figure 48: 1 km \rightarrow 2 km Low-Thrust PCO Reconfiguration Maneuver

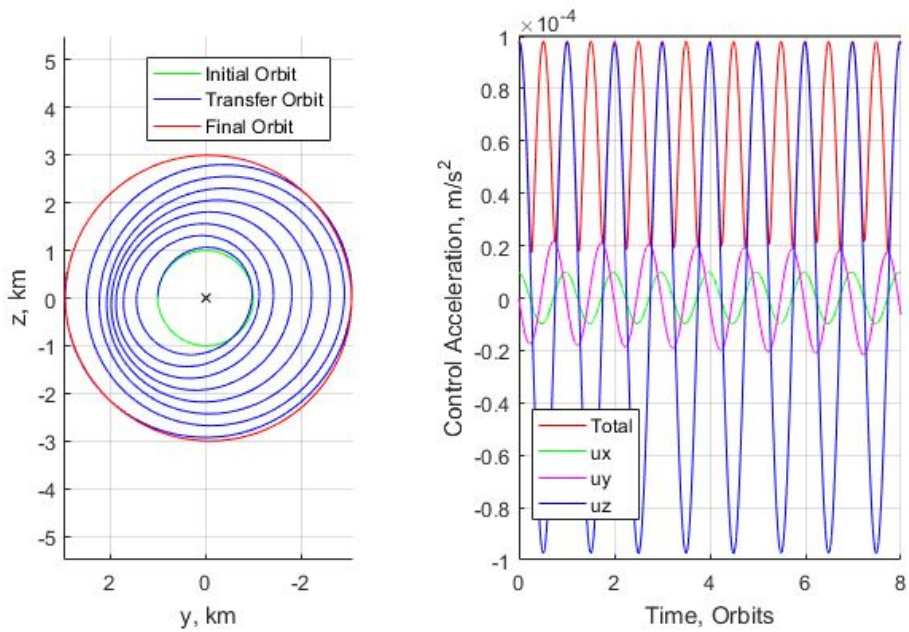


Figure 49: 1 km \rightarrow 3 km Low-Thrust PCO Reconfiguration Maneuver

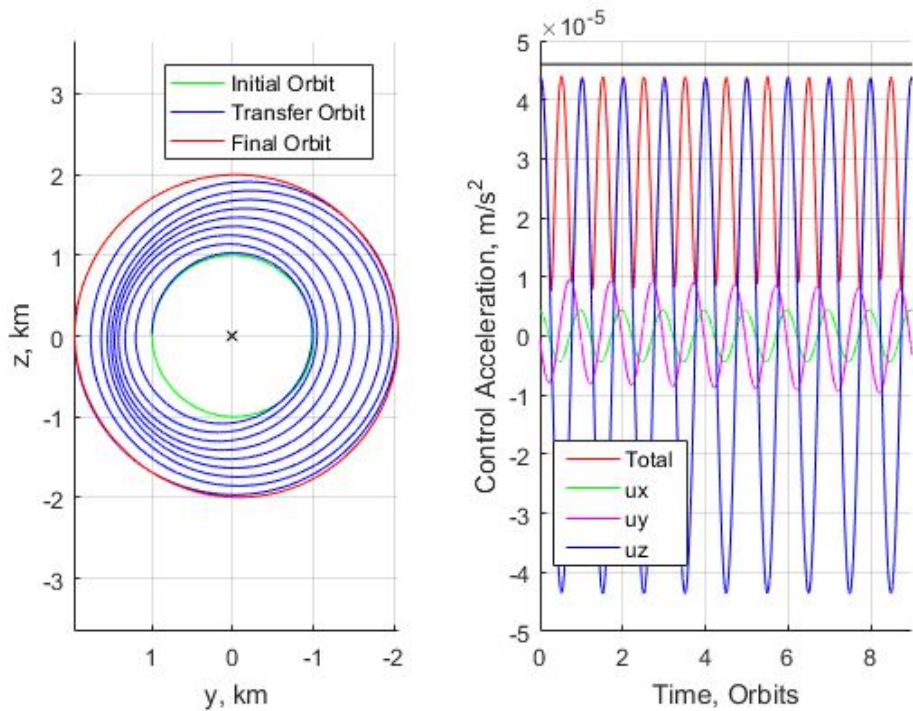


Figure 50: 1 km \rightarrow 2 km Low-Thrust PCO Reconfiguration Maneuver with 500 kg, 23 mN Thrust Satellite

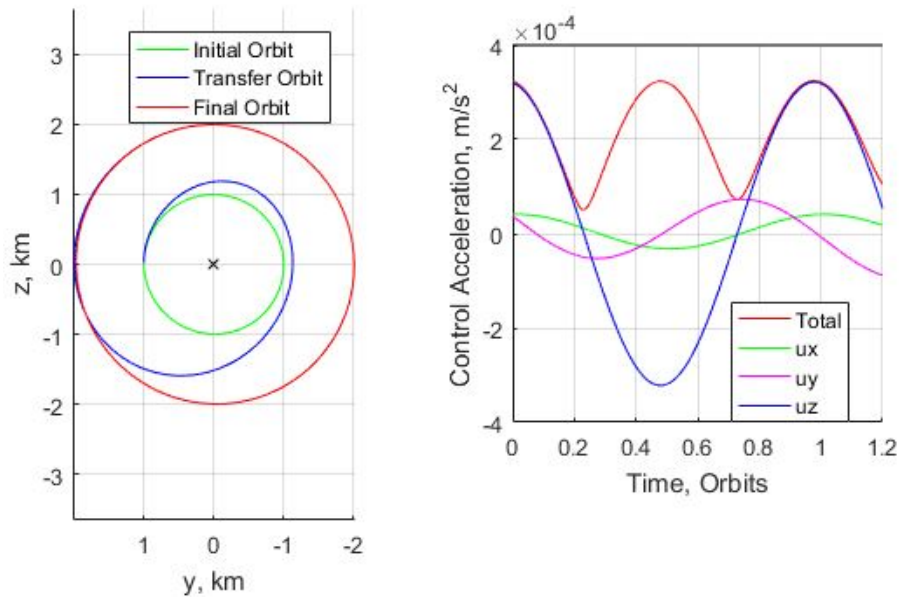


Figure 51: 1 km \rightarrow 2 km Low-Thrust PCO Reconfiguration Maneuver with 10 kg, 4 mN Thrust Satellite

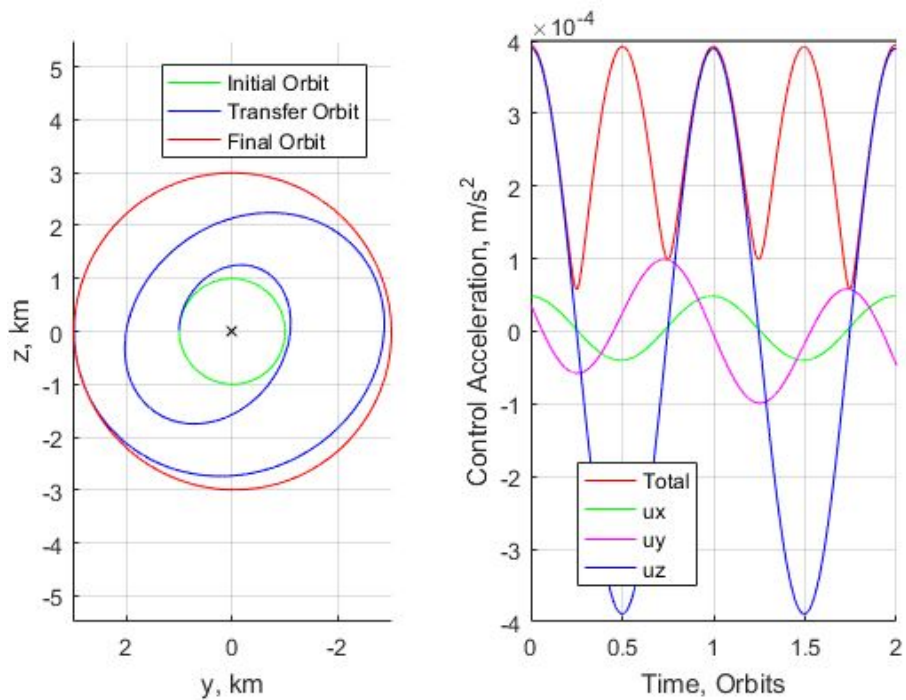


Figure 52: 1 km \rightarrow 3 km Low-Thrust PCO Reconfiguration Maneuver with 10 kg, 4 mN Thrust Satellite

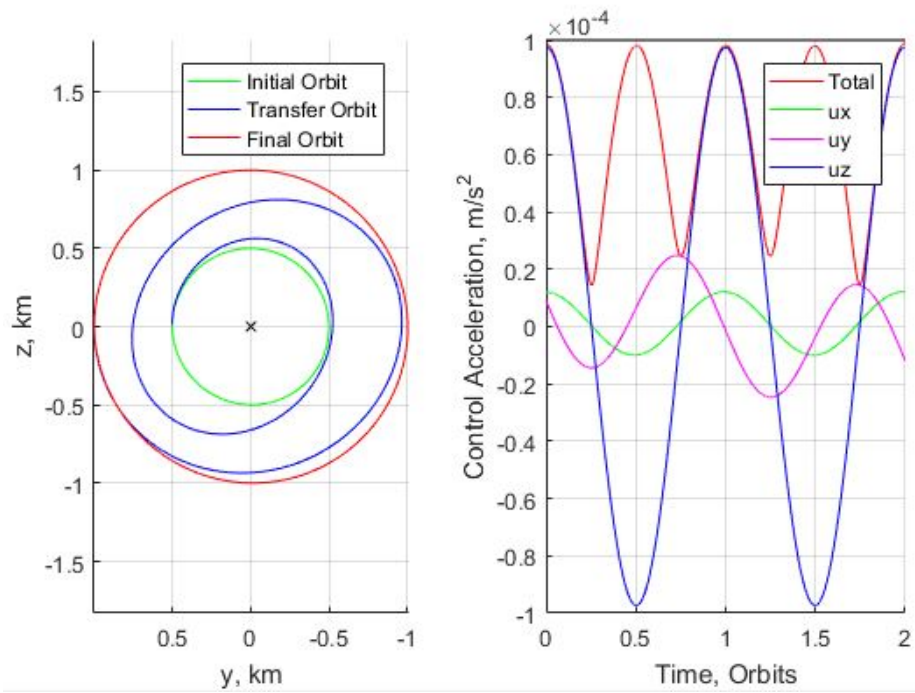


Figure 53: 0.5 km \rightarrow 1 km Low-Thrust PCO Reconfiguration Maneuver

Bibliography

1. Heidt, H., Puig-Suari, J., Moore, A. S., Nakasuka, S., and Twiggs, R., "CubeSat: A New generation of picosatellite for education and industry low-cost space experimentation," *14th Annual AIAA/USU Conference on Small Satellites*, Logan, UT, 2000.
2. Bouwmeester, J. and Guo, J., "Survey of worldwide pico- and nanosatellite missions, distributions and subsystem technology," *Acta Astronautica*, Vol. 67, 2010, pp. 854 – 862.
3. Gill, E., Sundaramoorthy, P., Bouwmeester, J., Zandbergen, B., and Reinhard, R., "Formation flying within a constellation of nano-satellites: The QB50 mission," *Acta Astronautica*, Vol. 82, 2013, pp. 110 – 117.
4. Alfriend, K. T., Vadali, S. R., Gurfil, P., How, J. P., and Breger, L. S., *Spacecraft Formation Flying*, Elsevier Astrodynamics Series, Elsevier, Oxford, UK, 2010.
5. Tooley, C. R., Black, R. K., Robertson, B. P., Stone, J. M., Pope, S. E., and Davis, G. T., "The Magnetospheric Multiscale Constellation," *Springer Science*, Vol. 199, 2016, pp. 23–76.
6. Queen, S., Shah, N., Benegalrao, S., and Blackman, K., "Generalized Momentum Control of the Spin-Stabilized Magnetospheric Multiscale Formation," *AAS/AIAA Astrodynamics Specialist Conference*, Vol. 15, Vail, CO, 2015, pp. 1–17.
7. D'Amico, S., Ardaens, J. S., and DeFlorio, S., "Autonomous Formation Flying Based on GPS - PRISMA Flight Results," *Acta Astronautica*, Vol. 82, 2013, pp. 69– 79.
8. Chung, J. S., Bandyopadhyay, S., Foust, R., and Subramanian, G. P., "Review of Formation Flying and Constellation Missions Using Nanosatellites," *Journal of Spacecraft and Rockets*, Vol. 53, No. 3, 2013.
9. Roscoe, C., Westphal, J., Lutz, S., and Bennet, T., "Guidance, Navigation, and Control Algorithms for CubeSat Formation Flying," *38th AAS Guidance and Control Conference*, Vol. 15, Breckenridge, CO, 2015.
10. Bonin, G., Roth, N., Armitage, S., Newman, J., Risi, B., and Zee, R. E., "CanX-4 and CanX-5 Precision Formation Flight: Mission Accomplished!" *29th Annual AIAA/USU Conference on Small Satellites*, Logan, UT, 2015, pp. 1–15.
11. Vaddi, S. S., Alfriend, K. T., Vadali, S. R., and Sengupta, P., "Formation Establishment and Reconfiguration Using Impulsive Control," *Journal of Guidance, Control, and Dynamics*, Vol. 28, No. 2, 2005, pp. 262–268.
12. Palmer, P., "Optimal Relocation of Satellites Flying in Near-Circular Orbit Formations," *Journal of Guidance, Control, and Dynamics*, Vol. 29, No. 3, 2006, pp. 519–526.

13. Vignal, P. and Pernicka, H., “Low-Thrust Spacecraft Formation Keeping,” *Journal of Spacecraft and Rockets*, Vol. 43, No. 2, 2006, pp. 466–475.
14. Gim, D. and Alfriend, K. T., “State Transition Matrix of Relative Motion for the Perturbed Nonsingular Reference Orbit,” *Journal of Guidance, Control, and Dynamics*, Vol. 26, No. 6, 2003, pp. 956–971.
15. Yan, H. and Alfriend, K. T., “Approximate Minimum Energy Control Laws for Low-Thrust Formation Reconfiguration,” *Journal of Guidance, Control, and Dynamics*, Vol. 30, No. 4, 2007, pp. 1182–1185.
16. Cho, H. C. and Park, S. Y., “Analytic Solution for Fuel-Optimal Reconfiguration in Relative Motion,” *Journal of Optimization Theory and Applications*, Vol. 141, No. 3, 2009, pp. 495–512.
17. Lee, S. and Park, S. Y., “Approximate Analytical Solutions to Optimal Reconfiguration Problems in Perturbed Satellite Relative Motion,” *Journal of Guidance, Control, and Dynamics*, Vol. 34, No. 4, 2011, pp. 1097–1111.
18. Massari, M. and Bernelli-Zazzera, F., “Optimization of Low-Thrust Reconfiguration Maneuvers for Spacecraft Flying in Formation,” *Journal of Guidance, Control, and Dynamics*, Vol. 32, No. 5, 2009, pp. 1629–1638.
19. Cho, H. C., Park, S. Y., Yoo, S. M., and Choi, K. H., “Analytical Solution to Optimal Relocation of Satellite Formation Flying in Arbitrary Elliptic Orbits,” *Aerospace Science and Technology*, Vol. 25, No. 5, 2012, pp. 161–176.
20. Tschauner, J. and Hempel, P., “Rendezvous zu einem in elliptischer Bahn umlaufenden Ziel,” *Astronautica Acta*, Vol. 11, No. 2, 1965, pp. 104–109.
21. “General Payload User’s Guide,” Spaceflight, Inc., 2015, SF-2100-PUG-00001 Rev. F.
22. “Canisterized Satellite Dispenser Data Sheet,” Planetary Systems Corporation, 2017, 2002337 Rev. E.
23. Hill, G. W., “Researches in the Lunar Theory,” *American Journal of Mathematics*, Vol. 1, No. 1, 1878, pp. 5–26, 129–147, 245–260.
24. Clohessy, W. H. and Wiltshire, R. S., “Terminal Guidance System for Satellite Rendezvous,” *Journal of the Aerospace Sciences*, Vol. 27, 1960, pp. 653–658, 674.
25. Vallado, D. A., *Fundamentals of Astrodynamics and Applications*, Microcosm Press, Hawthorne, CA, 4th ed., 2013.
26. Schweighart, S. A. and Sedwick, R. J., “High-Fidelity Linearized J_2 Model for Satellite Formation Flight,” *Journal of Guidance, Control, and Dynamics*, Vol. 25, No. 6, 2002, pp. 1073–1080.
27. Sullivan, J., Grimberg, S., and D’Amico, S., “Comprehensive Survey and Assessment of Spacecraft Relative Motion Dynamics Models,” *Journal of Guidance, Control, and Dynamics*, 2017, pp. 1–21.

28. Johnson, K. W., *Approaches for Modeling Satellite Relative Motion*, PhD dissertation, Texas A & M University, 2016.
29. Vadali, S. R., Sengupta, P., Yan, H., and Alfriend, K. T., “Fundamental Frequencies of Satellite Relative Motion and Control of Formations,” *Journal of Guidance, Control, and Dynamics*, Vol. 31, No. 5, 2008, pp. 1239–1248.
30. Vadali, S. R., Vaddi, S. S., and Alfriend, K. T., “An Intelligent Control Concept for Formation Flying Satellite Constellations,” *International Journal of Robust and Nonlinear Control*, Vol. 12, 2002, pp. 97–115.
31. Montenbruck, O. and Gill, E., *Satellite Orbits: Models, Methods, and Applications*, Springer, New York, NY, 3rd ed., 2005.
32. Cefola, P. J., “Equinoctial Orbit Elements - Application To Artificial Satellite Orbits,” *AIAA/AAS Astrodynamics Conference*, No. 72-937, 1972, p. 3.
33. Wiesel, W., *Modern Astrodynamics*, Aphelion Press, Beavercreek, OH, 2010.
34. Hintz, G. R., “Survey of Orbit Element Sets,” *Journal of Guidance, Control, and Dynamics*, Vol. 31, No. 3, 2008, pp. 785–789.
35. Schaub, H. and Junkins, J. L., *Analytical Mechanics of Space Systems*, American Institute of Aeronautics and Astronautics, Reston, VA, 3rd ed., 2014.
36. Markley, F. L. and Crassidis, J. L., *Fundamentals of Spacecraft Attitude Determination and Control*, Space Technology Library, Springer, New York, 2014.
37. Brouwer, D., “Solution of the Problem of Artificial Satellite Theory without Drag,” *The Astronomical Journal*, Vol. 64, No. 1274, 1959, pp. 378–397.
38. Greenwood, D. T., *Classical Dynamics*, Dover Science Books, Dover, Mineola, NY, 1997.
39. Lanczos, C., *The Variational Principles of Mechanics*, Dover Books on Physics, Dover, Mineola, NY, 1986.
40. Gim, D. and Alfriend, K. T., “Satellite Relative Motion Using Differential Equinoctial Elements,” *Celestial Mechanics and Dynamical Astronomy*, Vol. 92, 2005, pp. 295–336.
41. “Small Spacecraft Technology State of the Art,” Tech. Rep. TP2015216648, NASA Ames Research Center, 2015.
42. Conway, B. A., *Spacecraft Trajectory Optimization*, Cambridge Aerospace Series, Cambridge University Press, Cambridge, 2014.
43. Prussing, J. E. and Conway, B. A., *Orbital Mechanics*, Oxford University Press, Oxford, 2013.
44. Wiesel, W. E. and Alfano, S., “Optimal Many-Revolution Orbit Transfer,” *Journal of Guidance, Control, and Dynamics*, Vol. 8, 1985, pp. 155–157.

45. Goebel, D. M. and Katz, I., “Fundamentals of Electric Propulsion: Ion and Hall Effect Thrusters,” *Jet Propulsion Laboratory Space Science and Technology Series*, 2008.
46. Schaub, H. and Alfriend, K. T., “ J_2 Invariant Relative Orbits for Spacecraft Formations,” *Celestial Mechanics and Dynamical Astronomy*, Vol. 79, No. 2, 2001, pp. 77–95.
47. Vaddi, S. S., Vadali, S. R., and Alfriend, K. T., “Formation Flying: Accommodating Nonlinearity and Eccentricity Perturbations,” *Journal of Guidance, Control, and Dynamics*, Vol. 26, No. 2, 2003, pp. 214–223.
48. Vadali, S. R., Schaub, H., and Alfriend, K. T., “Initial Conditions and Fuel-Optimal Control for Formation Flying of Satellites,” *AIAA GNC Conference*, No. AIAA 99-4265, Portland, OR, 1999.
49. Kunz, D. L., *Intermediate Dynamics for Aeronautics and Astronautics*, Headmaster Press, Centerville, OH, 2015.
50. Sutton, G. P. and Biblarz, O., *Rocket Propulsion Elements*, John Wiley and Sons, Hoboken, NJ, 8th ed., 2010.
51. Yamanaka, K. and Ankersen, F., “New State Transition Matrix for Relative Motion on an Arbitrary Elliptical Orbit,” *Journal of Guidance, Control, and Dynamics*, Vol. 25, No. 1, 2002, pp. 60–66.

REPORT DOCUMENTATION PAGE

*Form Approved
OMB No. 0704-0188*

The public reporting burden for this collection of information is estimated to average 1 hour per response, including the time for reviewing instructions, searching existing data sources, gathering and maintaining the data needed, and completing and reviewing the collection of information. Send comments regarding this burden estimate or any other aspect of this collection of information, including suggestions for reducing the burden, to Department of Defense, Washington Headquarters Services, Directorate for Information Operations and Reports (0704-0188), 1215 Jefferson Davis Highway, Suite 1204, Arlington, VA 22202-4302. Respondents should be aware that notwithstanding any other provision of law, no person shall be subject to any penalty for failing to comply with a collection of information if it does not display a currently valid OMB control number.

PLEASE DO NOT RETURN YOUR FORM TO THE ABOVE ADDRESS.

1. REPORT DATE (DD-MM-YYYY) 22-03-2018		2. REPORT TYPE Master's Thesis		3. DATES COVERED (From - To) September 2016 - March 2018	
4. TITLE AND SUBTITLE Algorithms for Small Satellite Formation Flying				5a. CONTRACT NUMBER	
				5b. GRANT NUMBER	
				5c. PROGRAM ELEMENT NUMBER	
6. AUTHOR(S) LaRue, Robert B, 2LT				5d. PROJECT NUMBER 18YD334D	
				5e. TASK NUMBER	
				5f. WORK UNIT NUMBER	
7. PERFORMING ORGANIZATION NAME(S) AND ADDRESS(ES) Air Force Institute of Technology Graduate School of Engineering and Management (AFIT/EN) 2950 Hobson Way Wright-Patterson AFB OH 45433-7765				8. PERFORMING ORGANIZATION REPORT NUMBER AFIT-ENY-MS-18-M-273	
9. SPONSORING/MONITORING AGENCY NAME(S) AND ADDRESS(ES) Air Force Research Laboratory Charlene Jacka , Deputy Program Manager 20170 E Kirtland AFB, Kirtland AFB, NM 87117				10. SPONSOR/MONITOR'S ACRONYM(S) AFRL/RV	
				11. SPONSOR/MONITOR'S REPORT NUMBER(S)	
12. DISTRIBUTION/AVAILABILITY STATEMENT DISTRIBUTION A. APPROVED FOR PUBLIC RELEASE; DISTRIBUTION UNLIMITED					
13. SUPPLEMENTARY NOTES This material is declared a work of the U.S. Government and is not subject to copyright protection in the United States.					
14. ABSTRACT This thesis presents algorithms for spacecraft formation flying using impulsive-thrust and low-thrust methods. The general circular orbit formation initial conditions are derived in terms of equinoctial elements. Physical significance of the bounded relative motion parameters is presented for the case of general circular orbits. The developed algorithms are posed in terms of equinoctial elements for a singularity-free approach. The algorithms are assessed by numerical propagation of the inertial equations of motion with J2 and drag perturbations. Methods are presented for minimizing the ΔV required for formation initialization. An examination of the performance of open-loop and closed-loop control is provided for formation initialization and reconfiguration. The effects of differential drag on small satellite formations is analyzed. The developed algorithms are used to examine the trade space and quantify how spacecraft design parameters affect formation flying scenarios.					
15. SUBJECT TERMS Astrodynamics, Relative Motion, Formation Flying, Formation Design, Guidance and Control					
16. SECURITY CLASSIFICATION OF:			17. LIMITATION OF ABSTRACT UU	18. NUMBER OF PAGES 112	19a. NAME OF RESPONSIBLE PERSON Lt Col Kirk W. Johnson, AFIT/ENY
a. REPORT U	b. ABSTRACT U	c. THIS PAGE U			19b. TELEPHONE NUMBER (Include area code) 937-255-3636 x4285 kirk.johnson@afit.edu